Deliverable D2.14: Results of modelling and recommendations for future experimental and numerical work (HLW disposal system)

Work Package 2

This project has received funding from the European Union's Horizon 2020 research and innovation programme under grant agreement N°847593.

Document information

Project Acronym	**EURAD**
Project Title	**European Joint Programme on Radioactive Waste Management**
Project Type	**European Joint Programme (EJP)**
EC grant agreement No.	**847593**
Project starting / end date	**1st June 2019 – 30 May 2024**
Work Package No.	**2**
Work Package Title	**Assessment of Chemical Evolution of ILW and HLW Disposal cells**
Work Package Acronym	**ACED**
Deliverable No.	**D2.14**
Deliverable Title	**Results of modelling and recommendations for future experimental and numerical work (HLW disposal system)**
Lead Beneficiary	**SCK CEN**
Contractual Delivery Date	**June 2023**
Actual Delivery Date	**18 March 2024**
Type	**Report**
Dissemination level	**PU**
Authors	**Karel Lemmens (SCK CEN), Mathieu Debure (BRGM), Karine Ferrand (SCK CEN), Jules Goethals (Subatech), Sanheng Liu (SCK CEN), Nicolas Marty (BRGM)**

To be cited as:

Lemmens, K., Debure, M., Ferrand, K., Goethals, J., Liu, S., Marty, N. (2023): Results of modelling and recommendations for future experimental and numerical work (HLW disposal system). Final version as of 18.03.2024 of deliverable D2.14 of the HORIZON 2020 project EURAD. EC Grant agreement no: 847593.)

Disclaimer

Acknowledgement

This document is a deliverable of the European Joint Programme on Radioactive Waste Management (EURAD). EURAD has received funding from the European Union's Horizon 2020 research and innovation programme under grant agreement No 847593.

Status of deliverable		
	By	Date
Delivered (Lead Beneficiary)	SCK CEN	01/09/2023
Verified (WP Leader)	Diederik Jacques (SCK CEN)	06/12/2023
Reviewed (Reviewers)	Xavier Bourbon (ANDRA)	15/01/2024
Revised (Lead Beneficiary)	SCK CEN	14/02/2024
Verified (WP Leader)	Diederik Jacques (SCK CEN)	20/02/2024
Approved (PMO)		
Submitted to EC (Coordinator)	Andra (Coordinator)	19/03/2024

Executive Summary

EURAD WP2 ACED aims at modelling the chemical evolution at the disposal cell scale of geological disposal facilities for intermediate level (ILW) and high level (HLW) waste packages. The disposal cell scale is defined as the system consisting of waste packages, the engineered barrier system and the near-field host rock. The disposal cells differ between the various European countries. To ensure the evaluation of the modelling methodologies for a wide but representative range of properties and conditions relevant for different national programs, two representative disposal cells were proposed.

For HLW, these two cells consist of the following components:

- Disposal cell in granite : HLW glass / steel / bentonite clay / granite host rock
- Disposal cell in clay : HLW glass / steel / concrete / Callovo-Oxfordian (COx) claystone host rock

Task 3 of EURAD WP2 ACED concerns the mechanistic modelling of these systems at the experimental scale, using a selection of relevant experiments, and a first upscaling to the waste package level. This report describes the results of these modelling exercises. Focusing on the HLW studies, Task 3 thus consists of a *subtask 3.1* (Experimental analysis) and *a subtask 3.2* (Modelling of chemical evolution of HLW package).

Subtask 3.1 concerns experimental investigations that have generated data (characterization of interfaces) that were analyzed and allowed for model verification. Four experiments were selected for the HLW part. Details of the experimental setups are given in EURAD-ACED deliverable D2.10 (Gin 2019). These experiments have allowed to gather information about the chemical evolution at glass/steel/buffer interfaces, mainly the nature of newly formed phases, the glass alteration rate and the steel corrosion rate, according to the temperature and the nature of the buffer (clay or cement). The results were presented in EURAD-ACED deliverable D2.12 (Gin 2022). The numbering of the experiments was different in D2.10 and D2.12. The four experiments were the following (with the numbering of D2.12):

- A first experiment (Experiment 1 in D2.12, performed by CEA) concerns the system «Glass/steel/clay» in a setup with SON68 glass, (corroded and pristine) steel and COx claystone at 50 °C.
- A second experiment (Experiment 2 in D2.12) with a simple borosilicate glass in contact with iron and Boda claystone at 80°C, performed by MTA EK.
- A third experiment (Experiment 3 in D2.12, performed by EDF and ANDRA) concerns the system «Glass/steel/cement buffer/clay» in a setup with glasses SON68 and AVM V4, cement-bentonite grout, (corroded and pristine) steel and COx claystone at 70°C. A similar setup was tested without the cement-bentonite grout; this was a variant of the «Glass/steel/clay» system.
- A fourth experiment (Experiment 4 in D2.12, performed by SCK CEN) concerns the system «Glass/steel/cement» in a setup with glasses SON68 and SM539, steel and Ordinary Portland Cement (OPC) paste at 25°C.

An important limitation is that the experiments with clay were done with glass/steel/COx clay, whereas the reference system for granite host rock is glass/steel/bentonite clay. While experiments 1, 3 and 4 were already running (or even finished) before the start of EURAD, experiment 2 was started at MTA EK in the course of the EURAD-ACED project. This experiment was not included in D2.10, but the description and results of experiment 2 are presented in report D2.12.

Subtask 3.2 concentrates on the modelling of experiments studied in subtask 3.1 and the evolution of a HLW package for vitrified waste in the conditions imposed by the representative disposal cells mentioned higher. The modelling of experiments was performed only on experiment 3 and 4.

The conclusions can be summarized as follows:

Modelling of Experiment 3 (glass/steel/COx clay)

- To include the experimentally glass alteration gels in the model, some mineral phases had to be discarded. The selection of secondary phases allows to describe the main mechanisms (pH increase due to steel corrosion, and Si consumption due to the formation of Fe-bearing silicates) that drive the glass alteration.

- In addition, the modelled gel thickness agrees within the uncertainties with the mean measurements of the alteration layer in the experiments. Numerical results showed that glass alteration increased with the increase of the steel corrosion rate. The formation of a passivating gel was in competition with the precipitation of Cronstedtite-Th, identified at the iron – glass interface in task 3.1.

- The use of the GRAAL model in the context of iron/glass interaction required some caution in the resolution of kinetic reactions.

- The GRAAL model indicated that the glass alteration is promoted at the iron/glass interface: dissolution of the passivating gel promotes the glass alteration. This confirms the experimental observations, showing a large difference in the glass alteration layer thickness depending on the distance from the steel.

- Si is consumed due to the precipitation of secondary iron phases (greenalite, cronstedtite). The glass alteration is therefore function of the corrosion model (i.e. release of Fe^{+2} to the glass powder).

- The steel corrosion was simulated by a layer-by-layer approach.
    - This approach closely reproduced the mineral paragenesis observed in experiments and could be used with complex kinetics taking into account the effect of pH, temperature, O_2 partial pressure and/or the presence of a passivating layer on the steel/iron. The adopted simulation strategy showed that the Fe^{2+}, OH^- and H_2 concentration gradients affected the quantity but also the nature of the corrosion products.
    - The corrosion model had limitations that may affect glass alteration. An important limitation originates from the corrosion rate assumed constant. Moreover, the selection of secondary phases and corrosion products observed experimentally and reproduced by the model may not be the one that will formed in the repository over a longer time.

- Experiment 3 was carried out in fully saturated conditions (short time scale). H_2(g) generation should be considered for the modelling at waste package or disposal scale, but the coupled geochemical transport code MARTHE-PHREEQC has limitations on this aspect.

- MARTHE-PHREEQC uses a sequential non iterative approach (SNIA) to solve mass transport and chemistry. This, combined with a high mesh refinement of interfaces and the use of kinetic reactions, leads to high computation times. Hence simplification was required for modelling at the waste or disposal scales, with an increase of the grid size to 5 mm.

Overall, the numerical and experimental results are in good agreement, supporting the use of the simulation assumptions for extrapolation to generic cases.

Modelling of Experiment 4 (glass/steel cement)

- After 900 days only a very thin layer of cement has been altered. Transport of all the elements from the glass investigated here seems to be retarded in the cement due to either sorption or precipitation as secondary phases. The diffusion length for B in the cement is about 2 mm, and the diffusion length for Si is less than 0.5 mm.
- 1 D reactive transport model plus diffusion-controlled glass dissolution model can well reproduce the B solution concentration in the glass compartment, and the LA-ICP-MS and mineralogical profiles in the cement, including sorption of alkali cations on newly formed C-S-H with low Ca/Si ratio.
- The fitted boron diffusion coefficient in the cement is in the order of 10^{-14} $m^2 \cdot s^{-1}$, this is 100 to 1000 times smaller than the values usually assumed for cement (effective diffusion coefficient for HTO). The model assumes the same D_e for diffusion of silicon species, but because this element is solubility controlled, the diffusion profiles is more shallow than for boron. The concentration profiles of Si do, however, not reliably indicate the diffusion profile because the concentration of Si in the hardened cement paste is already very high (contrary to boron). The only indication concerning the penetration depth of Si is the reaction of the anhydrous phase. In the altered area, the amount of silicic acid was sufficiently high to dissolve portlandite and favor hydration.
- It is not clear if the low diffusivity is due to the speciation of the diffusing species or to a change in the properties of the altered cement versus the unaltered cement.
- The model is applicable at high pH (≈13.5) and does not consider an affinity effect; the only fitting parameters are the diffusion coefficients in glass and cement; effects of glass composition and cement properties are expressed via the diffusion coefficients.
- The penetration depths in the cement for different elements from the glass are different, indicative of complex interaction between elements from the glass and cement.
- The formation of a porous layer depleted in portlandite is well reproduced, but the exact porosity is not clear (gel porosity vs. open porosity; porosity is intrinsic parameter in D_{cement}).
- The faster dissolution of the glass particles at the interface with the cement was not modelled separately.
- The effect of the interaction with steel and a possible dense corrosion product layer was not studied, as there is no measurable corrosion of the stainless steel filters at pH 13.5.
- Even though the pozzolanic reaction is expected to speed up the release of calcium from the cement, the results show that only calcium in the cement close to the glass has reacted after 900 days; this can be explained by the low calcium solubility in the cement at high pH.

Modelling at waste package level (BRGM model, systems glass/steel/clay and glass/steel/cement)

- The modelling strategy has attempted to link the modelling of Experiment 3 with the modelling at the waste package scale. Parameters used in the modelling of the experiments were gradually modified to get a generic case (i.e. temperature, glass composition etc.). At the same time, modelling assumptions, such as the selection of secondary phases or the implementation of the GRAAL model, remained identical. Overall, the upscaling (i.e. space discretization of 5 mm rather than 1 µm at the interfaces and the consideration of the steel as a permeable medium) did not indicate significant modifications of numerical results.

- The modelling of generic cases indicated that the steel corrosion products were quantitatively and qualitatively dependent on the corrosion rate and the chemistry of the surrounding environment.
- The consideration of old concrete resulted in faster corrosion rates than with a young concrete.
- Overall, magnetite and iron silicate were predicted at the glass – steel interface.
- COx – steel interactions led to the precipitation of magnetite and iron carbonates with the possible formation of cronstedtite (depending on the modelled time) due to the Si diffusion from the glass.
- Magnetite was the main corrosion product expected at the concrete – steel interface.
- The glass dissolution rate appeared to be function of both the steel corrosion rate and the chemistry of the surrounding environment.

Modelling at waste package level (SCK CEN model, system glass/steel/cement)

- Modelling of Experiment 4 simulating a period of 450 years showed that a relatively small amount of glass would have to dissolve to decrease the pH at the glass surface from 13.6 (young cement) to pH 10.5.

The information for the upscaled modeling can be synthesized as follows:

- The model used for the simulation of Experiment 3 could be used to model the steel/CO_X and the glass/steel interaction for periods up to 10 000 years. The upscaling required a space discretization of 5 mm rather than 1 µm at the interfaces and the consideration of the steel as a porous media, but this did not lead to significant modifications of the numerical results.

- The selection of iron corrosion products and secondary phases used in the model in task 3.2 was different from the selection for the disposal cell modelling in task 4.1 presented in deliverable D2.17 (De Windt 2022). The modelling shows that the nature of the iron silicate affects the glass dissolution kinetics in the modelling as long as the iron is corroding. The modelled cases do not allow to evaluate how important the selection of iron corrosion products (magnetite, siderite, chukanovite…) and iron silicates greenalite, berthierine, cronstedite…) is for the long-term glass dissolution kinetics.

- Because task 3.1 did not include any tests with bentonite (e.g. Febex), there was no modelling of such experiment. Instead, Experiment 3 with interaction with COx clay was modelled. The physicochemical characteristics of Febex bentonite and COx clay are different for some parameters that should have an effect on the glass dissolution and the secondary phase formation, but a systematic study of this effect goes beyond the scope of task 3.

- An important upscaling problem is associated to the consideration of the fractures in a glass block. In contrast to the models used in task 4.1, the models used in task 3.2 do not consider these fractures. In task 4.1, the effect of fractures was simulated using a high diffusion coefficient for glass alteration layer. This diffusion coefficient is much larger than the ones used in task 3.2 for transport of species in the unfractured glass alteration layer. The diffusion coefficient used in the performance assessment driven model of task 4.1 thus has a meaning that is different from the diffusion coefficient used in the mechanistic modelling of task 3.

- The modelling of Experiment 4 suggests diffusion coefficients for boron in the altered young cement paste that are 100 to 1000 times smaller than the values usually assumed for cement and that were used also for the disposal cell calculations in D2.17. There are indications that these low D_e values are applicable also for silica released by the glass. It is not clear if the low D_e values are due to the boron and silicon speciation, or to a lower diffusivity of the altered cement paste. Such low diffusivity would slow down the interaction between the glass and the cement.

- For the very high pH conditions in young cement, three very different glass dissolution models have been used.
    - To model Experiment 4 with young cement and pH about 13.5, a diffusion driven glass dissolution model was used. In this model, all kinetics is represented in one lumped parameter, i.e. the diffusion coefficient.
    - To model the young cement system at waste package scale, the affinity driven GRAAL model was used. Glass alteration was assumed to start already when the pH was high. The results of this modelling exercise must be considered with reservation, because the pH conditions were out of the validity domain of GRAAL.
    - In D2.17 also an affinity driven glass dissolution model is used for the disposal cell calculations with young CEM I (see *Table 11*). However, in this more complete system simulation, the pH of the concrete decreases to <10 by the time of the perforation of the overpack. Hence the affinity driven glass dissolution model can be applied.
    - The diffusion driven high pH model was not used at waste package scale, but a calculation was performed in which the model simulating experiment 4 was allowed to run for several days to see how much glass must dissolve for the glass compartment to decrease the pH at the glass surface from 13.6 to pH 10 - 10.5, where the conventional affinity driven dissolution models are applicable. The conclusion was that a relatively small amount of glass is required for this. Experimental validation of the model (or another model) in this pH range is necessary to increase the confidence in this conclusion.

- The modelling of the Experiment 3 with glass/steel/COx suggests that the pH increase due to steel corrosion is significant at the clay side and at the glass side. The negative feedback effect of the higher pH on the steel corrosion rate (lower corrosion rate at higher pH) was not considered, although it would be two orders of magnitude lower at pH 12 than at pH 8. In cementitious media with high initial pH, the steel corrosion rate is much lower than in clay media. Hence the resulting pH increase due to the steel corrosion is also less important.

- Experiment 1 with SON68 in contact with a corroding piece of iron and COx clay at 50°C, showed higher corrosion rates than those observed in experiment 3, but there is a relatively large uncertainty on the corrosion rate, both on the extent and on the evolution with time (constant or decreasing). Because the steel corrosion provides iron for the formation of iron phyllosilicates that prevent the formation of a passivating amorphous silica gel, the assumptions made for the steel corrosion rate have a direct impact on the glass dissolution rate. Assumptions like a constant corrosion rate triggering the glass dissolution at a constant dissolution rate may be overconservative.

- Experiment 2 (simplified glass composition in contact with compact Boda clay with iron particles at 80°C showed lower dissolution rates than experiment 1, but in this setup there was no direct contact between glass and iron. Experiment 3 and 4 confirmed the importance of distance between the glass surface and the reacting EBS material (iron or cement paste). The glass alteration increasing effect is restricted to the outer layer.

- Pore clogging is a process with potentially large impact on the glass alteration rate and the evolution of the contacting engineered barriers. In report D2.17, the so called 'porosity feedback effect' would lead to a much slower glass dissolution with the bentonite buffer and with the cement buffer. The experiments and their modelling in task 3 did not provide direct evidence for a pore clogging effect in the clay medium. The boron profiles in the hardened Ordinary Portland Cement paste of Experiment 4 suggest a low diffusivity in the cement layer next to the glass, but no complete pore blocking.

- The experiments and modelling show that perforation of the overpack is delayed by a high pH buffer (cementitious materials) that decreases the overpack corrosion rate and by increasing the thickness of the overpack. Using a thicker cement buffer provides al longer protection, but once the overpack is perforated, the formation of iron-silicate phases is expected to trigger the glass dissolution. There is thus a trade-off between the short term advantage and long-term disadvantage of using a thicker overpack.

- A high pH will also trigger the glass dissolution. The waste package calculations suggest a rather constant and relatively high long-term dissolution rate for the ISG glass in young cement. In aged cement (pH 10.5) a lower dissolution rate is calculated, but there were no experimental data to validate the model in this range. Also the bentonite-grout mixture from Experiment 3 did not give information about this, because the bentonite-grout layer was too thin.

Based on the experience of the work done in task 3.1 and 3.2, a number of recommendations for future experimental and numerical work is given in section 6. The general conclusion is that the currently available experimental database to support the modeling of the integrated systems is not sufficient to validate a number of important mechanism and parameters of the mechanistic models. Data are missing especially at pH >10, where the classical affinity driven glass dissolution models may be not valid. Both further integrated and parametric experiments are necessary. The mechanistic modeling that was performed has given a general idea of the potential impact of the model parameters, but because of the long calculation times, only few cases could be tested. A more systematic approach with more calculation cases is necessary to come to more concrete conclusions.

Table of content

List of figures

List of Tables

Glossary

ASR: Alkali Silica Reaction

C-A-S-H: Calcium-Alumina-Silica-Hydrate

COx: Callovo-Oxfordian

C-S-H: Calcium-Silica-Hydrate

GAL: Glass Alteration Layer

HCP: Hardened Cement Paste

ISG: International Simple Glass

OPC: Ordinary Portland Cement

SAP: Secondary Alteration Products

YCWCa: Young Cement Water (with Ca)

1 Introduction

EURAD WP2 ACED aims at modelling the chemical evolution at the disposal cell scale of geological disposal facilities for intermediate level (ILW) and high level (HLW) waste packages. The disposal cell scale is defined as the system consisting of waste packages, the engineered barrier system and the directly surrounding near-field host rock.

These disposal cells differ between the various European countries. Details about this are given in EURAD-ACED deliverable D2.4 (Neeft 2019). To ensure the evaluation of the modelling methodologies for a wide but representative range of properties and conditions relevant for different national programs, two representative disposal cells for HLW were proposed.

These two cells consist of the following components:

- Disposal cell in granite: HLW glass / steel / bentonite clay / granite host rock
- Disposal cell in clay: HLW glass / steel / concrete / Callovo-Oxfordian (COx) claystone host rock

The specifications of the different reference systems are given in EURAD-ACED deliverables D2.16 (Samper 2022) and D2.17 (De Windt 2022) and are resumed in **section 2** of this report.

The reference systems are not only defined by the nature and dimensions of their constituents, but also by the expected long-term evolution of these systems. This evolution is also presented in section 2 of this report and agrees with the evolutions described in deliverable report D2.16 (Samper 2022).

Two types of modelling evaluations are foreseen:

1. *Upscaling and integration*: starting from mechanistic process knowledge and detailed modelling of individual processes and/or individual components, an integrated mechanistic model is built to simulate the chemical evolution at relevant spatial and temporal scales;
2. *Abstraction:* reducing the model complexity in a systematic way, such that (i) an acceptable description of the chemical evolution is preserved during model abstraction, and/or (ii) difference in some key variables of the chemical evolution can be described qualitatively and/or quantitatively. The full mechanistic models resulting from point 1 will be used to benchmark and evaluate different abstraction methodologies.

To realize this, WP3 ACED consists of three main experimental or modelling tasks:

- In Task 2 the steel/clay and steel/cement interfaces are studied.
- In Task 3, the waste package scale is studied. This comprises the waste package and the engineered barrier system.
- In Task 4, the entire disposal cell scale is studied.

Task 3 presents a first upscaling step from the relatively isolated processes at the interfaces studied in Task 2 to repository sub-systems, where chemical and physical processes might be closely intertwined.

This report D2.14 presents the key results from the work performed for the HLW system in Task 3. A similar report D2.15 (Blanc 2024) presents the results for the ILW system. Numerical modelling of the coupling between chemistry, transport processes and material alterations are a major effort in this task. The modelling work concentrates on describing the evolution of important chemical properties (redox pH, ionic strength) and other (geochemical) variables (e.g., mineralogy, porosity). This includes the evaluation and comparison of different conceptual and modelling approaches. The goal is to investigate to what extent abstraction in terms of process de-coupling or scale separations (spatial and temporal) are possible and appropriate: this analysis is shared with Task 4. For models that describe complex

interactions between materials and processes it is absolutely necessary to evaluate not only single process couplings with experimental data but also to compare with experiments with more complex interactions of materials and processes, preferably, if possible, at relevant space and time scales.

The main objectives of task 3 are:

- To evaluate how adequate available phenomenological concepts and models describe the chemical evolution of typical materials at an intermediate scale – i.e., parts of a repository composed of several materials in a fixed geometry (representative for ILW or HLW waste packages) well below the disposal cell scale.
- To identify critical processes and features driving and controlling the chemical evolution at the waste package scale.
- To provide information on relevance and influence of processes for implementation at disposal cell scale and for model abstraction (task 4).

Focusing on the HLW studies, Task 3 consists of a *subtask 3.1* (Experimental analysis) and *a subtask 3.2* (Modelling of chemical evolution of HLW package).

Subtask 3.1 concerns experimental investigations that have generated data (characterization of interfaces) that were analyzed and allowed for model verification. Four experiments were selected for the HLW system. Details of the experimental setups are given in EURAD-ACED deliverable D2.10 (Gin 2019). These experiments have allowed to gather information about the chemical evolution at glass/steel/buffer interfaces, mainly the nature of newly formed phases, the glass alteration rate and the steel corrosion rate, according to the temperature and the nature of the buffer (clay or cement). The results were presented in EURAD-ACED deliverable D2.12 (Gin 2022). The numbering of the experiments was different in D2.10 and D2.12. The four selected experiments were the following (with the numbering of D2.12):

- A first experiment (Experiment 1 in D2.12, performed by CEA) concerns the system «Glass/steel/clay» in a setup with SON68 glass, (corroded and pristine) steel and COx claystone at 50 °C.
- A second experiment (Experiment 2 in D2.12) with a simple borosilicate glass in contact with iron and Boda claystone at 80°C, performed by MTA EK.
- A third experiment (Experiment 3 in D2.12, performed by EDF and ANDRA) concerns the system «Glass/steel/cement buffer/clay» in a setup with glasses SON68 and AVM V4, cement-bentonite grout, (corroded and pristine) steel and COx claystone at 70°C. A similar setup was tested without the cement-bentonite grout; this was a variant of the «Glass/steel/clay» system.
- A fourth experiment (Experiment 4 in D2.12, performed by SCK CEN) concerns the system «Glass/steel/cement» in a setup with glasses SON68 and SM539, steel and ordinary Portland cement (OPC) paste at 25°C.

An important limitation is that the experiments with clay were done with glass/steel/COx clay, whereas the reference system for granite host rock is glass/steel/bentonite clay. While experiments 1, 3 and 4 were already running (or even finished) before the start of EURAD, experiment 2 was started at MTA EK in the course of the EURAD-ACED project. This experiment was not included in D2.10, but the description and results of experiment 2 are presented in report D2.12.

Subtask 3.2 concentrates on the modelling of the selected experiments studied in subtask 3.1 and the evolution of a HLW package for vitrified waste in the conditions imposed by the representative disposal cells mentioned higher. The results of the modelling of the experiments are presented in **section 3** of this report.

- The modelling by BRGM of the «Glass/steel/clay» variant of the third experiment (Experiment 3 in D2.12) is presented in section 3.1.

- The results of the modelling by BRGM of the «Glass/steel/cement-bentonite grout/clay» variant of the third experiment (similar to Experiment 3 in D2.12) were not yet available when this report was finalized. Hence the results are not included in the foreseen section 3.2. A publication was in preparation though (Grangeon, to be published).
- The modelling by SCK CEN of the «Glass/steel/cement» experiment (Experiment 4 in D2.12) is presented in section 3.3.
- Experiment 2 in D2.12 (glass/steel/Boda clay), started in the course of EURAD-ACED, was not included in the modelling scheme.

The modelling of the evolution of the HLW package requires an upscaling of the models used for the modelling of the experiments. The results of this study are presented in **section 4** of this report. Some deviations from the originally planned approach were necessary, though.

- Because of staff unavailability the HLW package calculations for the Glass / steel / clay / granite host rock could not be performed.
- Because the model applied by SCK CEN was tested only at the high pH of young OPC, it was not validated for use in the reference long-term conditions with a much lower pH. For this reason, alternative scoping calculations were performed to estimate the period of time required for the pH to decrease from the initial high pH to the lower pH where classical affinity driven models have been validated.

The reference long-term conditions are described in EURAD-ACED deliverable D2.17 (De Windt 2022).

Section 5 of this report presents the synthesis for the upscaled modelling
Section 6 presents recommendations for future experimental and numerical work.
The report ends with the list of references, an overview table with the processes modelled in task 3, and a table with the chemical formulae of most minerals mentioned in the report.

2 Integration of knowledge into models (concepts and processes)

2.1 Narrative

The narrative describes the system, evolution and high-level processes expected in the representative disposal cell systems and is complementary to the descriptions given in EURAD-ACED deliverables D2.16 (Samper 2022) and D2.17 (De Windt 2022). This description serves as a background that allows us to situate the conditions studied in the experiments described in D2.10 (Gin 2019) and modelled in task 3.2. It also mentions important processes that we do not consider in the experiments and models. There is a narrative for the clay buffer concept (section 2.1.1) and one for the cement buffer concept (section 2.1.2). It makes abstraction of differences between the specific national disposal systems, as given in D2.4 (Neeft 2022).

2.1.1 HLW glass/steel/bentonite/granite system

The HLW glass/steel/bentonite/granite reference system was described in EURAD-ACED deliverable D2.17 (De Windt 2022), and is shown in *Figure 1.* This HLW disposal cell concept in granite is based on the Spanish spent fuel reference concept in granite, known as ENRESA 2000 (ENRESA 2001). The

main difference with the reference system for vitrified waste lies in the dimensions of the carbon-steel overpack.

The generic configuration of the HLW disposal cell concept in granitic host rock includes

- The vitrified glass (40 cm in diameter)
- The overpack (5 cm thick) which is made of carbon-steel and considered as Fe(0) (glass canister and gap are neglected)
- The bentonite buffer (75 cm thick) which is composed of water-saturated FEBEX bentonite
- The Spanish Reference Granitic host rock (several meters thick in the calculations)

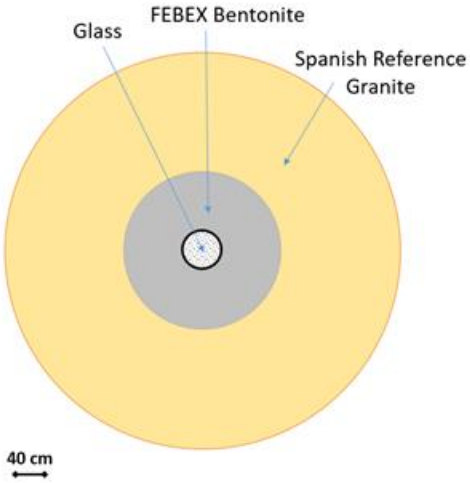

Figure 1. Layout of the representative HLW disposal cell in a granitic host rock (figure taken from D2.16 and D2.17).

An extensive description of the expected evolution of this system is given in EURAD-ACED deliverables D2.16 and D2.17, written for Task 4, and thus aiming at the evolution at the disposal cell scale. These evolutions are relevant for the modelling in Task 3 only in as far as they define the physico-chemical conditions at the time of the first contact of the HLW with the near field water. In this report D2.14, we focus on the evolutions that are relevant directly for the glass alteration.

Figure 2 taken from deliverable D2.16 presents schematically the successive periods considered in the evolution of the disposal cell. The scheme was developed for the HLW-cement buffer-clay system, but is applicable also to the HLW-bentonite buffer-granite system, with the exception that in the granite system, H_2 gas is not expected to cause desaturation of the near field.

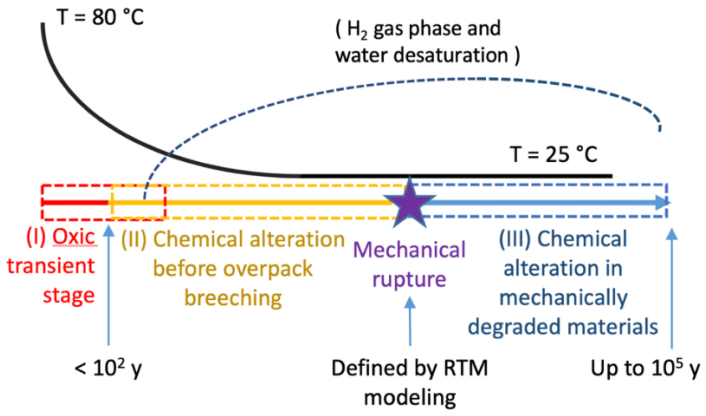

Figure 2. Graphical scheme of successive periods considered in reactive transport modelling (RTM) and evolution of temperature in the disposal cell (Figure taken from D2.16).

Figure 3 shows the same evolution in more detail, describing explicitly the relevant conditions and processes in each stage.

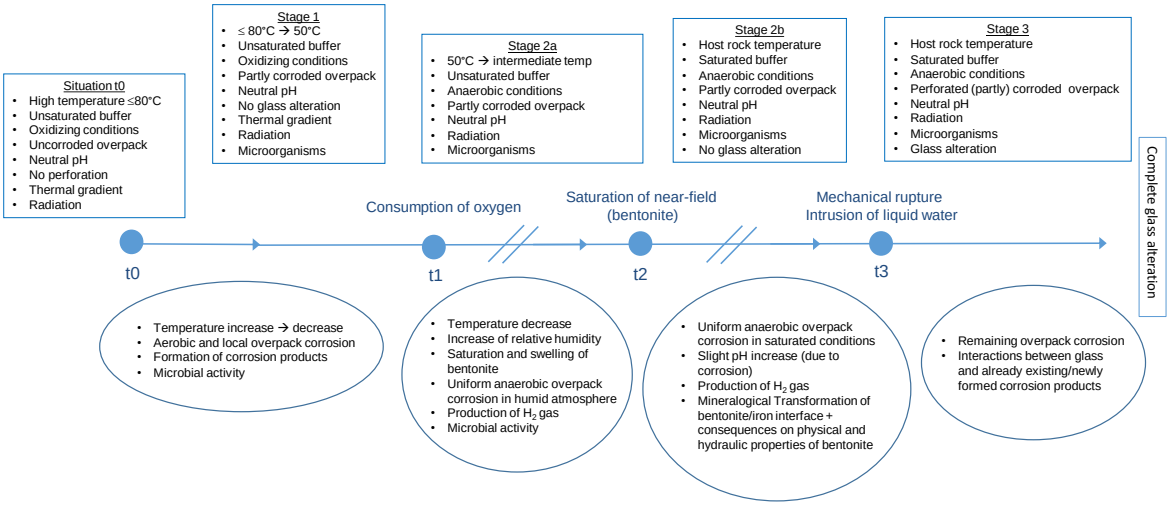

Figure 3. Descriptive scheme of successive stages in the bentonite/granite disposal cell, with the conditions governing each stage (rectangular boxes) and the main processes affecting the overpack corrosion and glass alteration (spherical boxes).

The description of the geochemical evolution of a HLW waste package with a bentonite buffer is mainly based on the Czech and Spanish national concepts in granitic host rock. The space between the overpack and the host crystalline rock will be backfilled with compacted bentonite. The following interfaces are thus involved: granite host rock/bentonite, bentonite/carbon-steel and carbon-steel overpack/vitrified waste. The excavation damaged zone is disregarded in Task 3 and is taken into account only in Task 4 as a sensitivity case.

The first stage in *Figure 2* and *Figure 3* corresponds to the transient phase from aerobic to anaerobic conditions and the consumption of residual oxygen. This period should last several decades, but less than 100 years, both in the bentonite/granite and in the cement/clay system. Aerobic corrosion and localized corrosion processes can occur, leading to the formation of first corrosion products. In the first stage, the temperature initially increases until the maximum temperature (≤ 80°C) is reached; then, the temperature decreases gradually. The temperature of 50°C in *Figure 3*. is indicative for a predisposal period of 100 years.

In the second stage in *Figure 2* and *Figure 3*, the conditions are anaerobic, and the main overpack corrosion process is anaerobic uniform corrosion that consumes water and generates H_2 gas, but the overpack is not yet perforated. In *Figure 3*, stage 2 is subdivided in stage 2a and 2b, with t2 the point in time of complete saturation of the bentonite buffer with incoming ground water.

In stage 2a the temperature further decreases; in stage 2b the temperature is assumed to have reached the host rock temperature.

The moment of the mechanical rupture is considered as the start of the third stage. With the steel corrosion rate given in D2.17, the perforation would occur after a few tens of thousands of years in the bentonite – granite system (25,000 years for an overpack of 5 cm that is perforated by mechanical stress when 3.5 cm has corroded, following D2.17). The anaerobic steel corrosion will continue after the perforation.

Other comments on the relevant processes:

- The impact of the high temperature and interaction with granite on the bentonite mineralogy is not considered in Task 3 (nor in Task 4). Indeed, the changes of the bentonite by interaction with the granite are expected to be smaller than those of the cement buffer. No illitization is expected. Major changes include smectite dissolution and precipitation of secondary clay minerals. The definition of an 'aged bentonite' (similar to 'aged concrete') is not needed.

- The alteration of the smectite near the granite interface will be less significant than at the bentonite/overpack interface. The steel corrosion will gradually lead to transformations of the bentonite/iron interface:
  - Precipitation of multi-layered corrosion products; the nature of the corrosion products depends on solution chemistry (pH, Fe and Si concentrations will evolve due to corrosion processes and associated bentonite transformations) and redox conditions;
  - Mineralogical transformations of bentonite with the destabilization of montmorillonite, replacement of bentonite minerals by Fe-rich smectites and non-swelling Fe-rich phyllosilicates.
  - Evolution of physical/hydraulic properties of bentonite induced by the mineralogical transformations: decrease of porosity and possible clogging near the bentonite/iron interface; evolution of hydraulic conductivity, diffusion coefficient and capacity to swell.

  These corrosion processes will change the physico-chemical characteristics of the near field. This is modelled in D2.17. In task 3.2 the bentonite/steel interaction was not studied, but the COx clay / steel interaction was modelled (see section 3 and 4).

- Figure 2 mentions desaturation (of the near field) by the produced H_2. This is indeed expected in the French design, with the low porosity Callovo-Oxfordian clay as host rock. In the reference granite host rock, such desaturation is not considered, because the fissures in the granite are pathways for fast transport of H_2 to the far field.

- Glass alteration is only considered in stage 3, i.e. after the breaching of the overpack, characterized by the following conditions:
  - The temperature has already decreased and is 50°C or less;
  - The transient period of resaturation is finished. The bentonite buffer is completely saturated.
  - Multi-layered corrosion products, formed during the previous periods are present, together with remaining uncorroded metallic iron. Only the outside of the overpack will have corroded before perforation occurs. This implies that at the time of first water/glass contact, only a relatively thin layer of uncorroded steel will be left. The thickness of this remaining layer of steel depends on the assumptions about the thickness required to resist to the host rock stresses. We can thus expect that (1) most of the iron will react with the bentonite before the overpack failure, (2) there will be a remaining part of uncorroded iron available to react with the glass after the overpack failure; and (3) the remaining iron corrosion products and iron-rich phyllosilicates will probably be less reactive towards the glass than the uncorroded iron or iron corrosion products that are formed in absence of a silica source (such as bentonite).

- The modelling in Task 3.2 focuses on glass alteration and the interactions of glass with corrosion products and residual uncorroded iron. The further dissolution of the glass after the complete conversion of iron into iron silicates is not modelled.

- In experiment 1 of EURAD-ACED deliverable D2.10, the clay that is used is not the reference bentonite but the Callovo-Oxfordian clay. The MTA EK experiment, described in D2.12, used Boda Clay. Even if the physico-chemical properties of these clays are different, the systems still show a qualitative similarity.

- Understanding the glass/steel interactions and their consequences on nuclear glass long-term behaviour requires knowledge of the main processes underpinning aqueous alteration of glass. According to EURAD-ACED deliverable D2.1 (Neeft 2022) and other literature (Vienna 2013, Gin 2015), glass alteration is due to the formation and dissolution of an alteration film layer, which is likely to incorporate chemical elements from the solution and to act as a diffusion barrier for reactive species. How effective this barrier is depends primarily on the concentration of silicon in solution in the vicinity of the glass. A summary of the impacting mechanisms is given in EURAD-ACED deliverable 2.16 (Samper 2022).

  The interactions of glass with corrosion products and residual uncorroded iron are important, since they can maintain high glass alteration rates over longer periods than in the same leaching solution without iron or iron corrosion products (Neeft 2022). However, this impact is only visible at local scale, and seems to be conditioned by the transport of elements in solution (Debure 2019), mainly iron and silicon. It seems to be significantly weaker when the glass is far from the iron source (corrosion products or iron). The experiments of task 3.1, described in D2.10 (Gin 2019) and D2.12 (Gin 2022) and the modelling of the experiments in this report confirm these processes.

  The corrosion products formed in stage 3 resulting from the corrosion of residual uncorroded metallic iron could be different from the corrosion products formed in stage 2a,b. Indeed, the elements released in solution by the glass alteration, in particular Si, can influence the nature of corrosion products. According to D2.1, corrosion products from a low-alloy steel disposal container are mainly composed of iron oxides such as magnetite (Fe_3O_4), or iron carbonates such as siderite ($FeCO_3$) or chukanovite ($Fe_2(OH)_2CO_3$). But in presence of clay iron silicates can also form. The experiments of task 3.1 (D2.10 and D2.12) and the modelling of the experiments in this report confirm these processes.

2.1.2 HLW glass/steel/cement buffer/clay system

The HLW glass/Cement/clay reference system was described in D2.16 and D2.17, and is shown in *Figure 4*.

The generic concept roughly corresponds to an intermediate state between the two European concepts developed for vitrified waste disposals in an argillaceous formation (the French liner concept and the Belgian/Dutch supercontainer concept). Two chemical compositions of the cement-base buffer are considered: either a bentonite/cement grout buffer (low-pH cement) more relevant for the French concept, or an ordinary Portland cement (OPC/CEM I), representative of the Supercontainer. For Task 4, the buffer thickness is varied, but for Task 3 this thickness is less relevant, because the spatial and temporal scale of the simulations is much smaller.

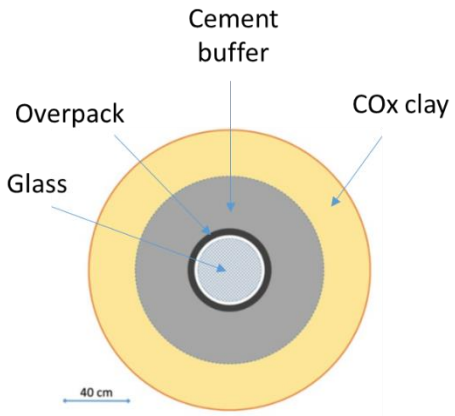

Figure 4. Layout of the representative HLW disposal cell in clay host rock.

The base case in D2.17 foresees the following characteristics:

- Thickness of the overpack = 5 cm (glass canister and gap are neglected).
- Thickness of the buffer = 30 cm, with variants of 5 and 100 cm
- Concrete = Young CEM I + calcareous aggregates
- Clay = Callovo-Oxfordian clay

Figure 2 in the previous section, taken from report D2.16 (Samper 2022) presents schematically the successive periods considered in the evolution of the HLW/Cement/clay disposal cell. *Figure 5* shows the same evolution in more detail, mentioning explicitly the potentially relevant processes in each stage.

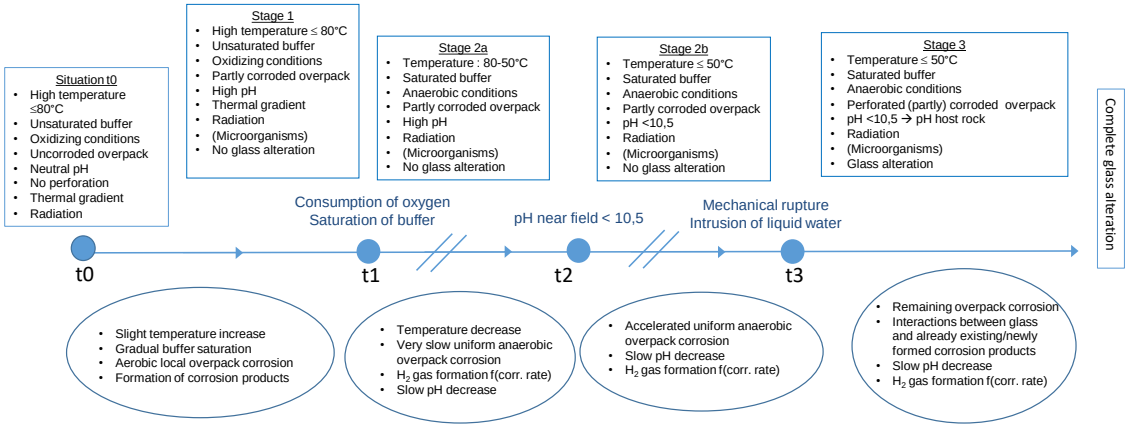

Figure 5. Descriptive scheme of successive stages in the cement/clay disposal cell, with the conditions governing each period (rectangular boxes) and the main processes affecting the overpack corrosion and glass alteration (spherical boxes).

The first stage in *Figure 2* and *Figure 5* is the oxic stage, lasting less than 100 years, like for the bentonite system. The second stage covers the evolutions before the perforation of the overpack.

Assuming fully water-saturated conditions, the chemical interactions between the clay environment and the cement (De Windt 2004) will progressively alter the buffer from a hyperalkaline fresh state (pH > 13), a depletion in portlandite (pH ≈ 12), the decalcification of C-S-H (10.5 < pH < 12), up to eventually the full carbonation (pH ≤ 10). The chemical interaction between the concrete and the clay rock will lead to the dissolution of the primary phases of cement and rock, and the subsequent precipitation of new mineral phases mainly close to the interface. Further away from the interface, the mineral alteration will be weaker but the hydrochemistry and cationic exchange properties of the rock will be impacted by the attenuated alkaline plume. This evolution has been modelled in D2.17 (De Windt 2022).

For the cementitious backfill, the corrosion rate of the overpack will be very low as long as the pH is >10.5. For this reason, the first perforation of the overpack is expected to occur only when the pH of the cement buffer has decreased to <10.5. Hence, the mechanical rupture in Figure 2 will be delayed, compared to the bentonite/clay system. The time of perforation will depend on the rate at which the pH of the cement buffer decreases. Calculations for task 4 suggest that the period of time required to reach a pH <10.5 depends very much on the thickness of the cement buffer (Table 3.13 of D2.17), but cracks in the cement can shorten this period considerably.

With the corrosion rates given in D2.17, perforation (for an uncracked cement buffer) would occur after about 25,000 years for an overpack of 5 cm thickness, assuming perforation by mechanical stress when 70% of the steel is corroded, but with a thicker cement buffer this would much later. With a buffer thickness 100 cm, the overpack would be perforated only after more than 100,000 years.

This implies that, at the time of the overpack perforation, the original cement (OPC buffer or bentonite-grout mixture) will have been transformed into a very different mineral assemblage, with a (much) lower pH than the pH of the original system. In the most likely evolution, the waste glass will thus never come in contact with high pH concrete.

At the time of perforation, most of the overpack will have corroded with formation of iron corrosion products. The most stable corrosion product in highly alkaline conditions (pH>11), maintained by the cement system, under anoxic conditions is magnetite (D2.8). The formation of the stable iron oxides/hydroxides can be inhibited, depending on kinetics, temperature and local composition, but the

cement phase can take up iron, with formation of phases like the (Al, Fe)-monosulfate and (Al, Fe)-ettringite, or Fe containing C-S-H.

The main mechanisms according to which the glass interacts with fresh OPC concrete are

i. the reaction of Si released from the glass with portlandite to form Calcium Silicate Hydrates (C-S-H), i.e. the pozzolanic reaction,
ii. the reaction of the Al released from the glass with the C-S-H phases to form Calcium Aluminium Silicate Hydrates (C-A-S-H phases),
iii. the further enrichment of the C-S-H phases with Si,
iv. the formation of an Alkali – Silica – Reaction (A-S-R) gel.

In degraded, old OPC concrete, only the 2nd, 3rd, and possibly the 4th mechanism should be important. Unfortunately, very little is known about the effective impact of these mechanisms on the glass alteration rate. The experiments performed so far to study the impact of cement phases on glass alteration have typically focused on the behaviour in young OPC concrete (pH<13) or evolved OPC concrete (pH 12.5), where the reaction with portlandite triggers the glass dissolution. No experiments have been done with old OPC concrete (C-S-H, 10.5 < pH < 12) or more representative iron containing C-S-H phases. Tests with old OPC concrete water in initial equilibrium with C-S-H, but without addition of the solid phases have been performed, though. They suggest that low glass dissolution rates can be reached at pH ≈ 11, probably thanks to the protective effect of the remaining Ca in the old cement water (Lemmens 2019). Hence, in absence of more focused studies and for the time being, one can assume that the glass dissolution mechanisms in the old OPC concrete are similar to the mechanisms in more neutral pH media, including the potential temporary triggering effect of the iron (corrosion products).

In an alternative scenario, we can consider local perforation of the overpack when the pH of the cementitious buffer is still >10.5, in spite of the low overpack corrosion rate at high pH. This would be somewhere between t1 and t2 in Figure 5. In this scenario, the glass will be exposed to high pH water. This scenario is unlikely, though. Hence it is not considered as a reference case for the modelling at the waste package or disposal cell level. Still the experiments with cementitious media in Task 3.1, reported in EURAD-ACED deliverables D2.10 (Gin 2019) and D2.12 (Gin 2022) were performed with young cement mixtures. The supporting modelling of these experiments will thus consider glass/young cement interaction.

The French design, with the Callovo-Oxfordian clay as host rock and a bentonite/grout mixture as buffer, has some typical effects on the evolution:

- With the Callovo-Oxfordian clay as host rock, H_2 generation by anaerobic steel corrosion in combination with the low porosity host rock would lead to a period of desaturation of the near field, under which the steel and glass will corrode in humid atmosphere. This is not considered in task 3.2.
- The initial pH of the bentonite/grout buffer (pH 11) will be much lower than with an OPC buffer (pH 13.5). Hence the pH will decrease faster, and exposure of the glass to high pH cement water is not expected.

On the long term, the main characteristics relevant for the glass alteration may be similar for the aged OPC cement buffer and the aged bentonite-grout buffer. Tests performed in subtask 3.1 indeed suggest that addition of the grout had little impact, but in this experiment the grout layer was much thinner than it would be in reality. Calculations for task 4.1 suggest that the pH buffering capacity of a 5 cm thick cement-grout mixture is lost in less than 1,000 years (D2.17).

- Two other processes could also have an influence during the different regimes: the radiation and also the potential influence of microorganisms, but they are not taken into account in Task 3. Bacteria can induce pitting corrosion below pH 10 or 11, but this is believed to be negligible

in the HLW reference disposal system, which leaves very little space for bacterial growth (clay buffer) or has a high pH (concrete buffer), as mentioned in D2.1 (Neeft 2022).

- In the cement-grout buffer and Callovo-Oxfordian claystone (studied in Experiment 3), the expected geochemical evolution depends on the chemical composition of the cement-grout buffer and its evolution with time. The system could be an intermediate between the clay buffer concept and cement buffer concept, with alkaline conditions and a gradual neutralization during the first stages that lead to a return close to neutral conditions in stage 3.

2.2 Processes governing the dissolution of waste glass in disposal conditions

The main high-level processes governing the dissolution of waste glass in disposal conditions were mentioned in the narrative of section 2.1. Different glass dissolution models can include different processes and mechanisms, or include them in a different way. For modelling at the disposal cell scale, detailed processes used in the waste package models can be omitted or simplified, while other processes are relevant only at the disposal cell scale.

A (non-exhaustive) table with these processes is presented at the end of this report. The table is conceived in such a way that it allows a comparison between (1) the processes modelled in the simulations of the experiments of task 3.1, (2) the waste package calculations of task 3.2, and possibly also (3) the model proposed for the upscaling in task 4. The table presents only the processes for the glass/steel/cement/clay system, because the system with bentonite was not explicitly modelled.

3 Model implementation and validation by experiments

In this section, we describe the models that are used to model the experiments described in D2.10 (setup) and D2.12 (results).

The following experiments are included in D2.12:

- Experiment 1: SON68 glass in contact with COx Clay and corroding steel at 50°C, performed by CEA.
- Experiment 2: A simple borosilicate glass in contact with iron and Boda claystone at 80°C, performed by MTA EK.
- Experiment 3: SON68 and AVM V4 glass in contact with COx clay, magnetite and corroding steel, and a second series where a thin layer of the bentonite-grout mixture separates the stainless steel from the COx, at 70°C, performed by EDF and ANDRA.
- Experiment 4: SON68 and SM539 glass in contact with a stainless steel filter and a young CEM I paste, at 25°C, performed by SCK CEN.

Modelling in the framework of EURAD-ACED was performed only for experiment 3 and 4.

3.1 Modelling of Experiment 3 (glass/steel/COx clay) by BRGM

This section presents the modelling by BRGM of the experiments carried out by EDF/ANDRA dealing with glass/steel/COx clay interactions (Experiment 3).

3.1.1 Numerical tools

MARTHE-PHREEQC is an extension of hydrological code MARTHE (http://marthe.brgm.fr/, Thiéry2015), which has been upgraded by coupling with the chemical module of PHREEQC (Parkhurst and Appelo 2013). The coupling algorithm uses a sequential non-iterative approach (SNIA): at each time step, MARTHE computes the hydraulic heads and the velocities in the whole domain. It then transports energy in order to determine the temperature field, and transport of all the considered dissolved chemical elements. Then, geochemical behaviour is computed using the PHREEQC module in each discretized cell.

Version 10a of the THERMOCHIMIE thermodynamic database (Giffaut 2014) (https://www.thermochimie-tdb.com/) was used. Considering the work of (Truche 2009) and the experimental conditions (time scale, temperature and pH), the database was modified in order to inhibit sulfate reduction by hydrogen.

A list with the minerals that are used further in this report and their chemical formula is given in Appendix B.

3.1.2 Modelled system

The EDF experimental apparatus consisted of a closed cylinder where Callovian-Oxfordian claystone (COx), iron and glass interacting together. Similar experiments performed with cement–bentonite grout are reported in section 3.2. The experiment was carried out in fully saturated conditions at a constant temperature of 70 °C. Three systems were studied in a single reactor with the assumption that the systems cannot influence each other. The systems simultaneously studied in the same apparatus were:

- COx/stainless steel/glass (powder). This is area 1 in *Figure 6*.
- COx/stainless steel/magnetite/glass (powder) interface. This is area 2 in *Figure 6*.
- COx/ (stainless and carbon) steel (plate) / glass (2 contacting monoliths). This is area 3 in *Figure 6*.

In the setup of area 1 and area 2, the glass powder is contained in perforated stainless steel 'micro-containers'. A 1 µm layer of magnetite has been deposited on the outside of a micro-container to represent the corrosion products. The micro-containers (with and without magnetite deposition) were perforated by multiple holes to ensure the water saturation of the enclosed glass powder. Mineralogical transformations were characterized after 6 months, 1 year and 3 years.

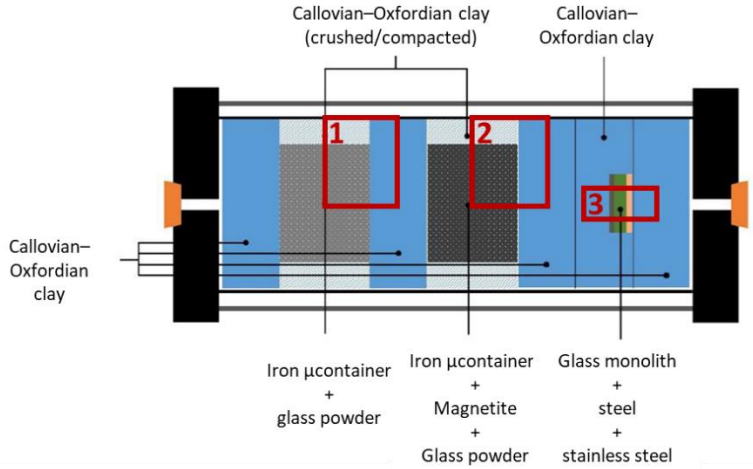

Figure 6. Schematic representation of Experiment 3.

The interactions dealing with a micro-container (areas 1 & 2 in *Figure 6*) were simulated using a 2D radial geometry (*Figure 7*) with a spatial discretization of 1 µm at the interfaces. A time step of 10^{-2} day has been used to process calculations.

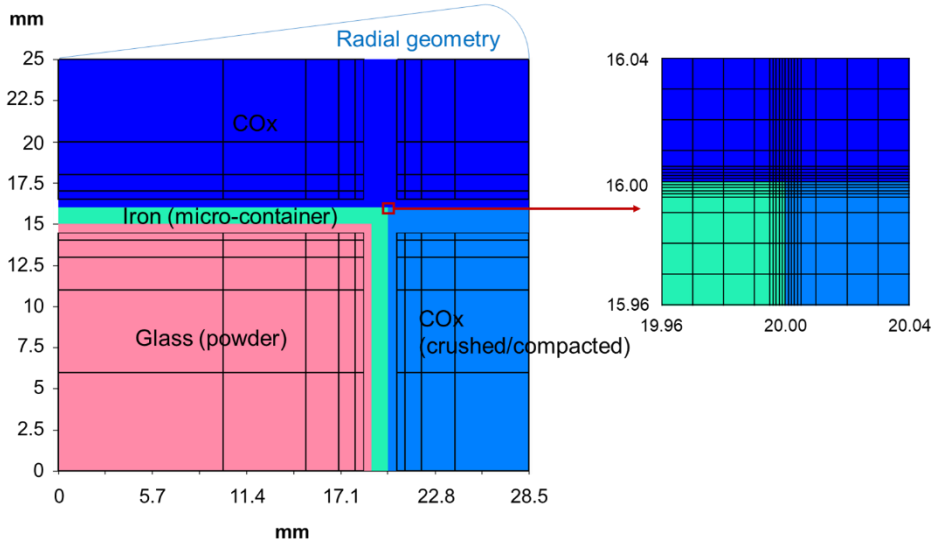

Figure 7. Considered radial geometries for the modelling of areas 1 & 2 in Figure 6 (BRGM model).

The interactions dealing with metallic plates and glass monoliths (area 3 in *Figure 6*) were simulated using a 1D Cartesian geometry (*Figure 8*) with the same spatial discretization of 1 µm at the interfaces.

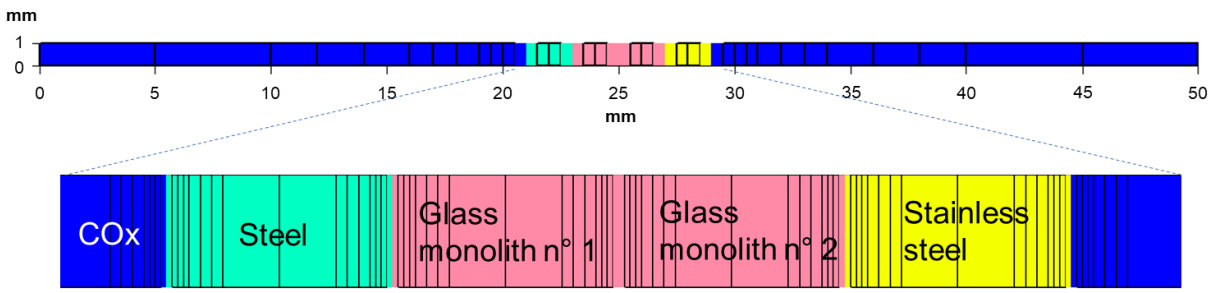

Figure 8. Considered geometries for the modelling of area 3 reported in Figure 6 (BRGM model).

3.1.3 Material representation in the modelling

3.1.3.1 Steel and stainless steel

Steel was considered as pure iron (i.e. 100 wt% of Fe^0) whereas 65 wt% of Fe^0 was assumed for the 309 stainless steel. The other elements (35 wt% of C, Cr and Ni) were discarded. Moreover, distinct corrosion rates were selected for each material. EDF observations as well as literature data dealing with similar interactions (e.g. Carriere 2020) indicates a carbon steel-corrosion rate of about 2 µm·year^{-1} at 70 °C. This value was, therefore, implemented in the model for micro-containers (areas 1 & 2 in *Figure 6*) and steel plate (area 3 in *Figure 6*). A constant corrosion rate of 0.5 µm·year^{-1} at 70 °C was selected for the stainless steel plate in agreement with the characterizations of EDF experiments (area 3 in *Figure 6*).

A layer-by-layer corrosion was simulated with the help of PHREEQC capabilities. This implies that corrosion of a deeper layer cannot start if iron remains in the more superficial layer (*Figure 9*). The reaction rate was function of the number of sides exposed to the alteration process. Hence, the corrosion rate of the corner shown in *Figure 9* is twice the one of the planes. Such a representation with an iron flux, and the related transformations, directly localized at the interface with the COx or the glass is more realistic than corrosion occurring simultaneously over the entire iron depth, which is usually the case the iron when it is modelled as a porous medium.

The perforated micro-containers were defined as porous (10%) and permeable media (D_e = 5.3 10^{-9} $m^2 \cdot s^{-1}$ at 70 °C). For the steel and stainless steel plates in area 3, distinction was made between the deeper and the superficial layers. The deeper layers were assumed to be impermeable (to simulate this D_e is set at 10^{-45} $m^2 \cdot s^{-1}$, this is the lowest value that can be used in the code) and not porous as long as the more superficial layers are not completely corroded, while the corroding superficial layer was considered porous (5 %) and permeable (D_e = 5.6 10^{-11} $m^2 \cdot s^{-1}$ at 70 °C). The assumed porosity has no physical meaning, but is required by the code, which needs a water volume in which the aqueous reactions take place.

Note that it is necessary to define each matrix as a porous medium anyway since MARTHE-PHREEQC, as all geochemical codes, cannot solve geochemical reactions in the absence of water.

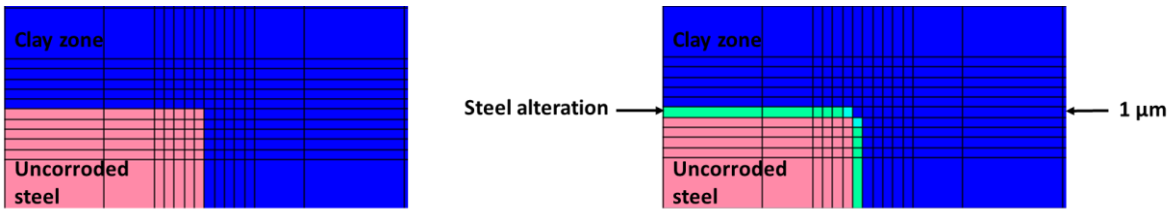

Figure 9. Illustration of layer-by-layer corrosion in the BRGM model.

Magnetite is expected to be the main corrosion product in reducing environment (Chivot 2004). The iron conversion into magnetite cannot be processed at the thermodynamic equilibrium because such a reaction would lead to sole production of magnetite and H_2 (in the following equation, we neglect aqueous Fe that would be in equilibrium with magnetite):

$$3Fe^0 + 4H_2O \rightarrow Fe_3O_4 + 4H_2 \qquad \text{(Equation 3.1)}$$

Such an overall reaction disagrees with experimental data showing the precipitation of other corrosion products (e.g. Carriere 2020, Necib 2016) and a pH increase (e.g. Kaufhold 2021, Bourdelle 2017).

In order to avoid that all the corroded iron turns into magnetite a kinetic control was applied, limiting the reaction as follows:

$$6Fe^{0} + 10H_2O \rightarrow 3Fe^{+2} + 6OH^{-} + Fe_3O_4 + 7H_2 \qquad \text{(Equation 3.2)}$$

Considering the lack of kinetic data for magnetite precipitation, it was assumed that 1 mol of iron can give 1/6 mol of magnetite. Hence, 1 volume of iron can give ~1 volume of magnetite leading then to a precipitation of additional corrosion products, a pH increase and a migration of other reaction products (OH^-, Fe^{+2} and H_2) toward other materials (COx or glass). Indeed, in saturated clay media, only half of the oxidized Fe is retained and the other part is potentially transported elsewhere (Carriere 2020, Schlegel 2010).

3.1.3.2 Glass

The most extensive studies have been undertaken on the SON68 glass (inactive version of the R7T7 French nuclear glass), a borosilicate glass without any Mg. A simplified alteration reaction was established from literature data (Fleury 2013):

$$SiB_{0.53239}Na_{0.42073}Al_{0.12708}Ca_{0.09500}Zr_{0.02838}Fe_{0.04812}Ni_{0.01295}Zn_{0.04072}Li_{0.1752}Cs_{0.01357}Sr_{0.00432}P_{0.00494}Mo_{0.01542}O_{3.632089} \rightarrow 0.12708Al^{+3} + 0.53239B(OH)_4^{-} + 0.09500Ca^{+2} + 0.004812Fe^{+2} + 0.043308Fe^{+3} + 0.01295Ni^{+2} + 0.02838Zr^{+4} + 0.04072Zn^{+2} + 0.1752Li^{+} + 0.42073Na^{+} + 0.01357Cs^{+} + 0.00432Sr^{+2} + 0.00494H_2(PO_4)^{-} + 1.0H_4(SiO_4) + 0.01542MoO_4^{-2} - 0.981618H^{+} - 2.578911H_2O$$

A small amount of Fe^{+3} was considered based on an Andra analysis (personal communication).

A layer-by-layer alteration was considered for modelling the alteration of the glass monoliths (region 3, see section 3.1.5.1.3 and 3.1.5.1.4). Like for the steel, the reacting layer is assumed to be porous (5%) and permeable (effective diffusion coefficient D_e in the glass of 1.8 10^{-22} $m^2 \cdot s^{-1}$), while the deeper layer is not porous and impermeable.

The layer-by-layer alteration was not applied to the glass powder (region 1, see section 3.1.5.2.3). The glass powder was defined as a porous (40%) and permeable medium following the experimental conditions (known mass of glass introduced in a given volume, leaving 40% of the volume for water). The diffusion coefficient for water was used here (D_e = 5.6 10^{-11} $m^2 \cdot s^{-1}$ at 70 °C).

The SON68 alteration was kinetically controlled using the GRAAL model (e.g. Frugier 2018) converted to the PHREEQC formalism (Debure 2019).

3.1.3.3 Callovian-Oxfordian claystone (COx)

The considered phases and the exchange capacity (0.174 meq g^{-1} of rock) of the COx claystone were taken from (Gaucher 2009). The mass percentages (*Table 1*) were slightly modified from (Marty 2015a): K-feldspar was neglected and siderite was switched with goethite according the COx reactivity with the temperature increase (Gailhanou 2017). Silicates and aluminosilicates were processed under kinetic control, based on the work of Marty (Marty 2015b, Marty 2018). Montmorillonite (Montmorillonite-HCCa in the thermodynamic database) and chlorite (Ripidolite_Cca-2) were only allowed to dissolve. A diffusion coefficient (D_e) of 5.6 10^{-11} $m^2 \cdot s^{-1}$ at 70 °C was assumed for the claystone.

Mineral name in THERMOCHIMIE	Mass fraction	mol·L^{-1} of rock
Calcite	0.22	5.04
Celestite	0.01	0.12
Ripidolite_Cca-2	0.02	0.07
Dolomite	0.04	0.50
Illite-Imt-2	0.34	1.94
Montmorillonite-HCCa	0.08	0.49
Pyrite	0.01	0.19
Quartz	0.24	9.16
Goethite	0.01	0.26
Siderite	0	0

Table 1. Mineralogical assemblage of the COx argillites. Mineral concentration (mol·L^{-1} of rock) calculated assuming a porosity of 18% used in the BRGM model.

A synthetic claystone pore fluid was used for the liquid saturation of the EDF experimental apparatus. The fluid chemistry was equilibrated with the mineralogical assemblage at 70 °C.

3.1.4 Selection of secondary phases

The selection of phases allowed to precipitate is an essential step for the realization of the calculations: ideally, it must be based as much as possible on the experimental observations and be as broad as possible not to force a preferential pathway. Moreover, if not observed in claystone, secondary minerals must be undersaturated with respect to the COx pore water at 25 °C (mineralogical consistency). The selection was made following discussion and feedback with Andra. The French agency has initiated and supported numerous studies on glass/iron/clay/cement interactions. However, following this first screening, some phases were discarded (e.g. heulandite, okenite, mordenite, clinoptilolite, greenalite, minnesotaite and analcime that are thermodynamically predicted as alteration product of the glass) because of their strong competition with the formation of gels (i.e. passivating and non-passivating gels), thus leading to a too high glass-dissolution rate. This could be solved using kinetics limiting the formation of these secondary phases. Unfortunately, no precipitation rates could be extracted from the literature. The mineralogical selection is reported in *Table 2*. Note that the modelling assumptions made for the iron corrosion forces the precipitation of magnetite, siderite, mackinawite and chukanovite, the main phases observed as corrosion products, with a release of Fe^{+2}, OH^- and H_2 towards the other materials. A table with the chemical formulae of the most relevant minerals is given at the end of this report.

	Mineral name in THERMOCHIMIE	COx	Glass	Iron	Remark
COx primary phases	Calcite	Eq	Eq	-	
	Celestite	Eq	Eq	-	
	Dolomite	Eq	Eq	-	
	Goethite	Eq	Eq	-	
	Illite-Imt-2	Kin	Kin	-	
	Montmorillonite-HCCa	Kin	-	-	
	Pyrite	Eq	Eq	-	
	Quartz	Kin	Kin	-	
	Ripidolite_Cca-2	Kin	-	-	
GRAAL end-members	SON68	-	Kin	-	
	SiAlgel	-	Kin	-	log K at 90 °C[a]
	SiAlCagel	-	Eq	-	log K at 90 °C[a]
	SiCagel	-	Eq	-	log K at 90 °C[a]
	SiAlNagel	-	Eq	-	log K at 90 °C[a]
	SiZrCagel	-	Eq	-	log K at 90 °C[a]
	SiZrNagel	-	Eq	-	log K at 90 °C[a]
	$CaMoO_4$(s)	Eq	Eq	-	i.e. Powellite
	Hydroxyapatite	Eq	Eq	-	
	Lizardite	Eq	Eq	-	preferred to Silicate-Mg[b]
	Pimelite	Eq	Eq	-	log K at 90 °C[a]
	Zincsilite	Eq	Eq	-	log K at 90 °C[a]
Corrosion model	Chukanovite	Eq	Eq	Eq	from LLNL database[c]
	Iron	-	-	Kin	
	Magnetite	Eq	Eq	Kin	
	Mackinawite	Eq	Eq	Eq	
	Siderite	Eq	Eq	Eq	
Additional phases	Anhydrite	Eq	Eq	-	
	Berthierine(FeII)	Eq	Eq	-	
	Berthierine(FeIII)	Eq	Eq	-	
	Berthierine_ISGS	Eq	Eq	-	
	Brucite	Eq	Eq	-	
	Borax	Eq	Eq	-	from LLNL database[c]
	Cronstedtite-Th	Eq	Eq	-	
	CSH0.8	Eq	Eq	-	
	CSH1.2	Eq	Eq	-	
	Ferrihydrite(am)	Eq	Eq	-	
	Gibbsite(am)	Eq	Eq	-	from THERMODDEM[d]
	Gypsum	Eq	Eq	-	
	Magnesite(syn)	Eq	Eq	-	
	Natrolite	Eq	Eq	-	
	Nontronite-Na	Eq	Eq	-	

	Pyrrhotite	Eq	Eq	-	
	Saponite-FeCa	Eq	Eq	-	
	Saponite-FeNa	Eq	Eq	-	
	Sepiolite	Eq	Eq	-	from THERMODDEM[d]
	Stratlingite	Eq	Eq	-	
	Strontianite	Eq	Eq	-	
	Vermiculite-Ca	Eq	Eq	-	

[a] log K only available at 25 °C in the current version of GRAAL
[b] $Mg_4Si_6O_{15}(OH)_2{:}6H_2O$ used in GRAAL
[c] Johnson 2000
[d] Blanc 2012

Table 2. Selection of mineral phases. Eq, Kin and - stand for a processing at the thermodynamic equilibrium, under kinetic control and not considered, used in the BRGM model.

3.1.5 Results of the modelling of Experiment 3 (glass/steel/COx clay)

3.1.5.1 Interactions between metallic plates and glass monoliths (area 3 in *Figure 6*)

After one year of simulated time, the alteration fronts are a few micrometer thick at the different interfaces; it is necessary to zoom in the profile to observe these mineralogical transformations. The presentation of numerical results focused on mineralogical transformations because the EDF experimental apparatus was not designed to sample the fluid and therefore its chemical composition is not available.

3.1.5.1.1 COx – carbon steel interface (area 3 in *Figure 6*)

Corrosion products predicted after 1 year at the COx – steel interface are reported in *Figure 10*. A corrosion rate of ~2 µm·year^{-1} led to the precipitation of magnetite, chukanovite, mackinawite, siderite, saponite-FeCa and berthierine(FeII). The pH increased up to 10.2 in steel layers subjected to corrosion at 70 °C. Chukanovite precipitated directly in contact with the steel whereas siderite precipitated in a more distant zone. Such a mineral sequence agrees with Azoulay (Azoulay 2012) who reports that, in the case of high-pH conditions (10.3-10.9 at 25 °C), chukanovite can be formed without siderite. We note also the absence of magnetite in the COx, even if the mineral was processed at the thermodynamic equilibrium in this area. Such a result appeared consistent with the work of Bourdelle (Bourdelle 2017). Saponite and berthierine are expected during clay-iron interactions (e.g. Mosser-Ruck 2010).

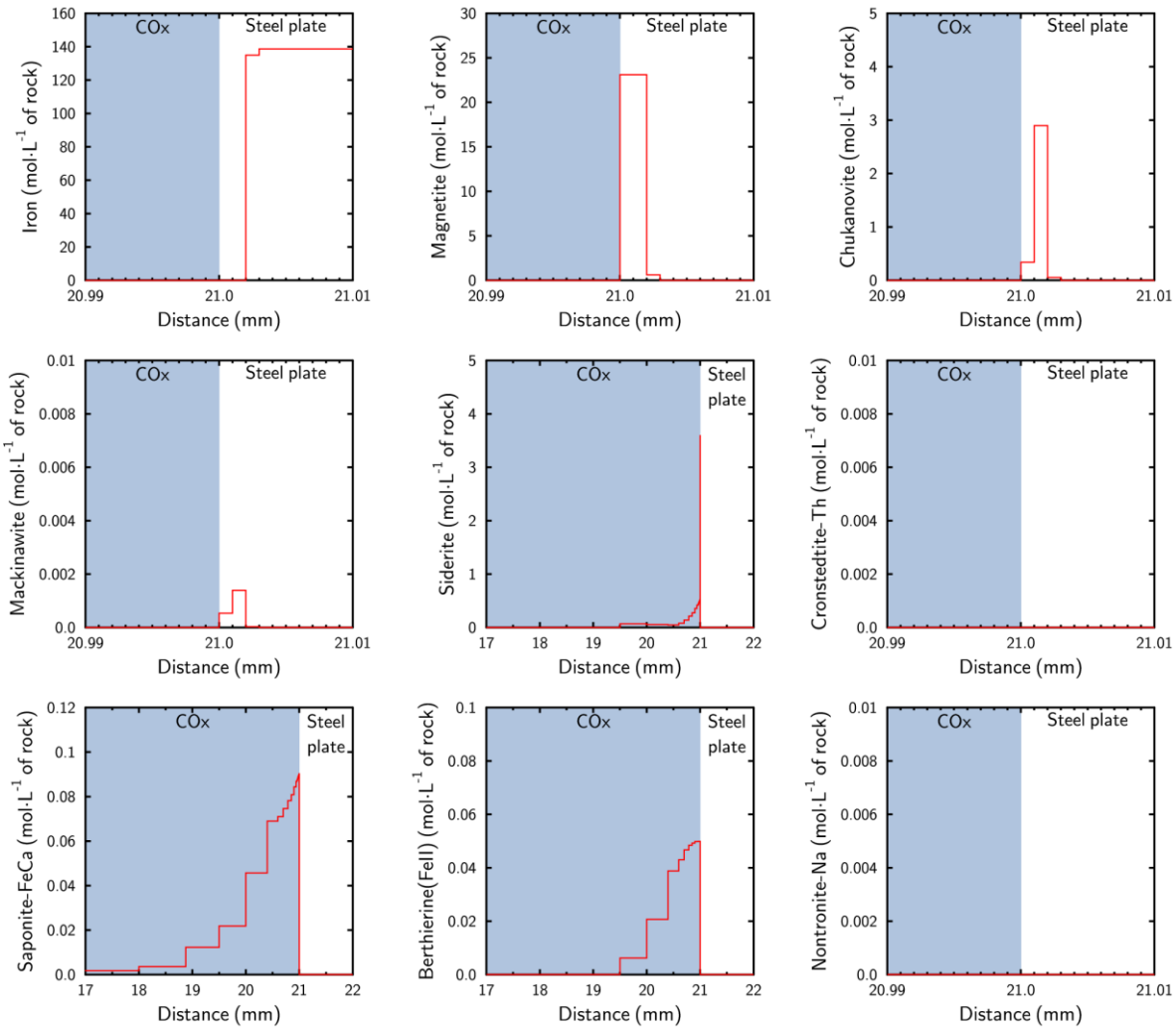

Figure 10. Corrosion products calculated with the BRGM model at the COx – carbon steel interface after 1 year in Experiment 3 at 70°C (area 3 in Figure 6).

The main transformation of the COx mineralogical assemblage (*Table 1*) concerned the conversion of pyrite (FeS_2) in pyrrhotite (FeS) promoted by the H_2 production from the iron corrosion (*Figure 11*). Such a transformation was experimentally observed (e.g. Mosser-Ruck 2020).

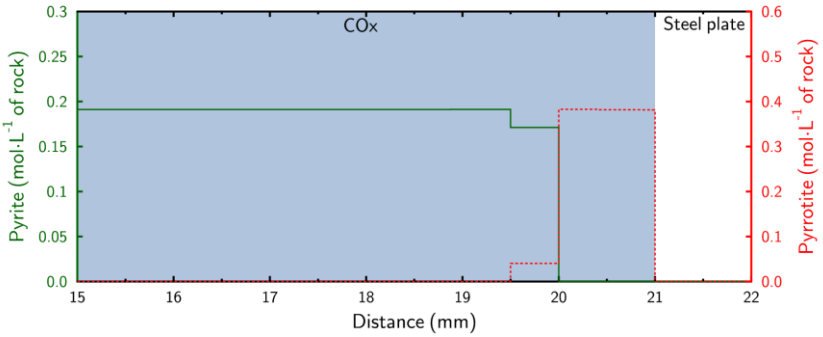

Figure 11. Pyrite – Pyrrhotite conversion in the COx clay calculated with the BRGM model at the interface with the carbon steel after 1 year in Experiment 3 at 70°C (area 3 in Figure 6).

The H_2 diffusion through the COx occurred concomitantly with the dissolution of goethite (*Figure 12*). A low dissolution of montmorillonite-HCCa promoted the precipitation of saponite-FeCa and berthierine (FeII). No significant transformation was simulated for the other primary COx minerals.

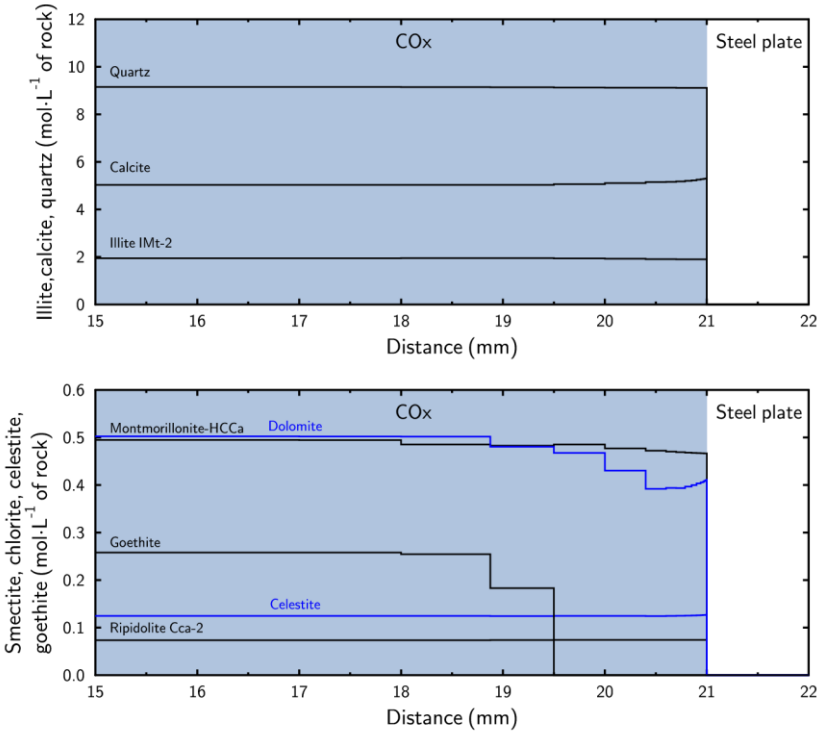

Figure 12. COx mineral alteration calculated with the BRGM model at the interface with the carbon steel after 1 year in Experiment 3 at 70°C (area 3 in Figure 6).

3.1.5.1.2 COx – stainless steel interface (area 3 in *Figure 6*)

Corrosion products predicted at the COx – stainless steel interface are reported in *Figure 13*. A corrosion rate of ~0.5 µm·year^{-1} was imposed leading to a precipitation of magnetite, chukanovite, mackinawite, siderite, saponite-FeCa and berthierine (FeII). This corrosion rate involved an increase of pH up to 10.1 in the first stainless steel layer.

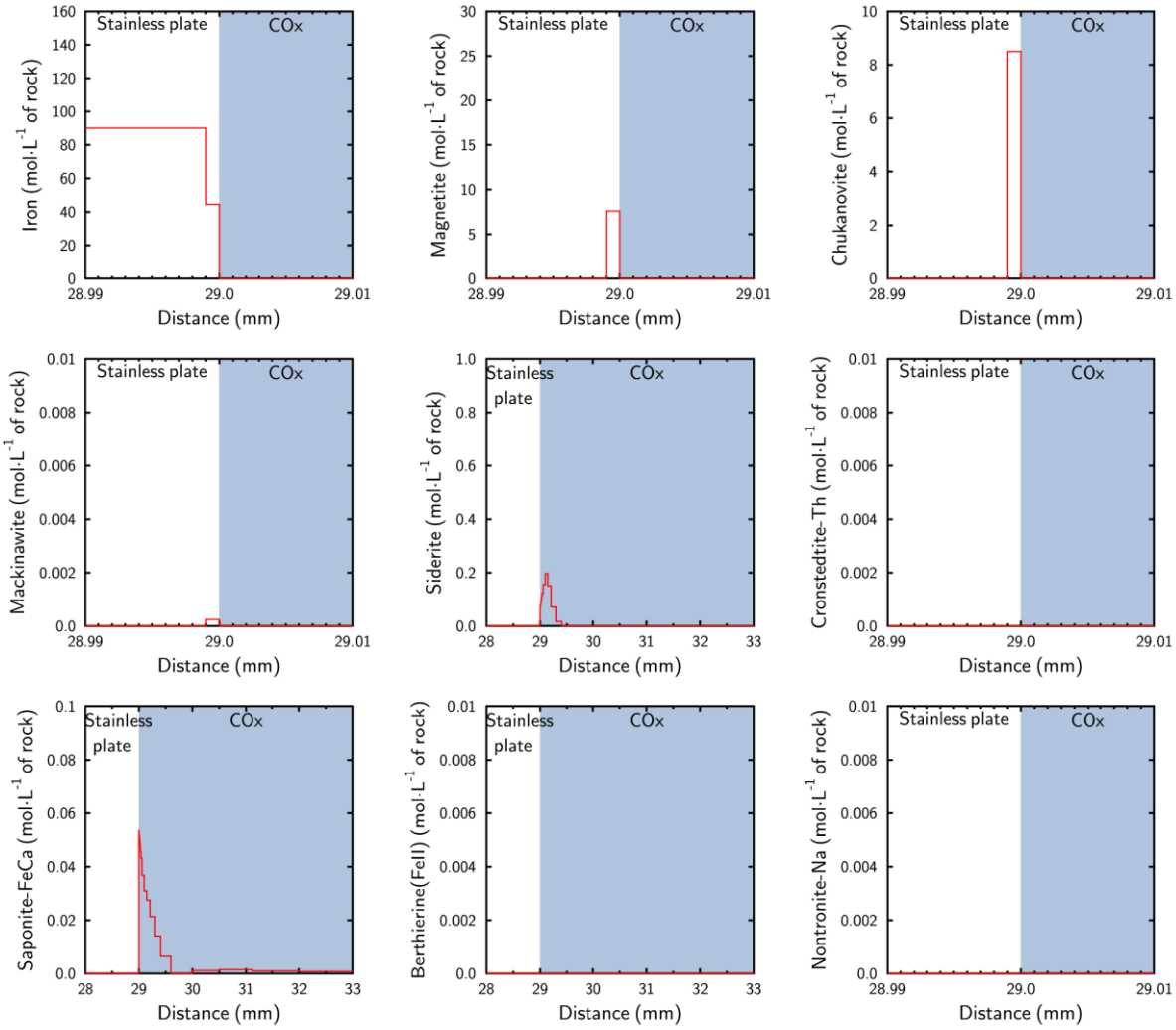

Figure 13. Corrosion products calculated with the BRGM model at the COx – stainless steel interface after 1 year in Experiment 3 at 70°C (area 3 in Figure 6).

A conversion of Pyrite in Pyrrhotite was also predicted (*Figure 14*).

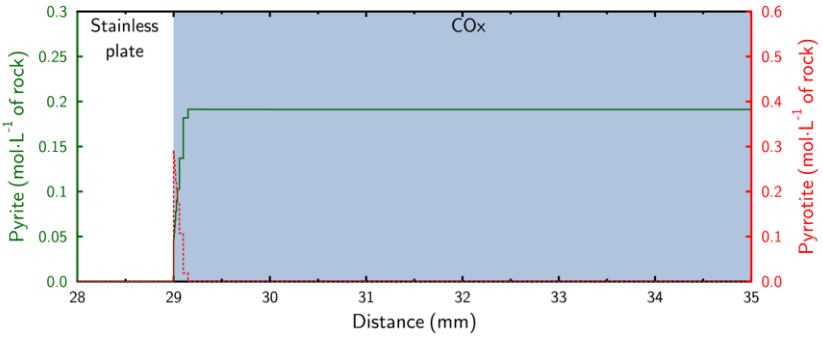

Figure 14. Pyrite – Pyrrhotite conversion calculated with the BRGM model in the COx clay at the interface with the stainless steel after 1 year in Experiment 3 at 70°C (area 3 in Figure 6).

The model predicted alteration of goethite while alteration of other primary COx minerals was negligible (*Figure 15*). The transformations involved are thus the same as those observed when COx is contacting the carbon steel but less advanced due to the slower corrosion rate of the stainless steel. Note that stainless steel was fully composed of Fe in the model (section 3.1.3.1). However, stainless steel also contains Cr, Ni and other minor elements that can reach 35 wt% and thus leave only 65 wt% of Fe. The Si consumption can be balanced by the potential secondary phases formed with those Cr and Ni elements, but the characterization did not give evidence for phases that might be considered in the model. For this reason and for the sake of simplicity (the model is already complex and including the chemistry of Ni and Cr would require model development that was not foreseen for EURAD-ACED), those stainless steel components were not considered in the model.

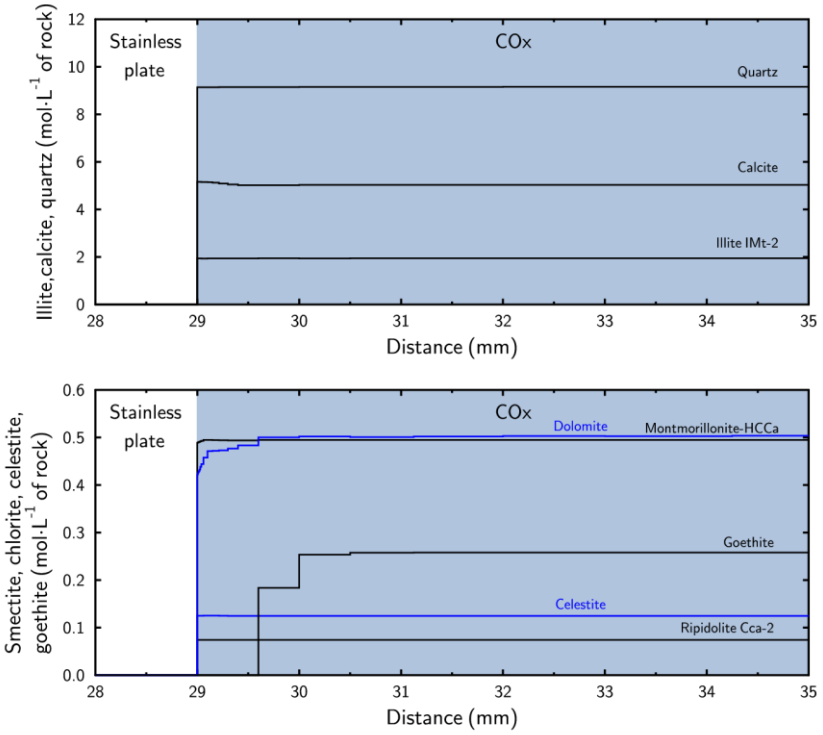

Figure 15. COx mineral alteration calculated with the BRGM model at the interface with the stainless steel after 1 year in Experiment 3 at 70°C (area 3 in Figure 6).

3.1.5.1.3 SON68 glass – carbon steel interface (area 3 in *Figure 6*)

Applying a carbon steel corrosion rate of 2 µm·year^{-1}, the corrosion products at the glass – steel interface were magnetite, chukanovite, saponite-FeCa and cronstedtite-Th (*Figure 16*). A pH of 10.8 at 70 °C was predicted at the interface. We note little precipitation of chukanovite due to the absence of CO_2 input related to the consideration of impermeable materials (i.e. iron plates and monoliths) with a 1D Cartesian geometry (*Figure 8*). Moreover, such geometry favours the pH increase because it neglects the surrounding environment. The presence of chukanovite in the corrosion-product layer rather than siderite, and precipitated Mg-rich and Fe-rich silicates at the gel surface seem to be due to the high-pH conditions (Carriere 2020).

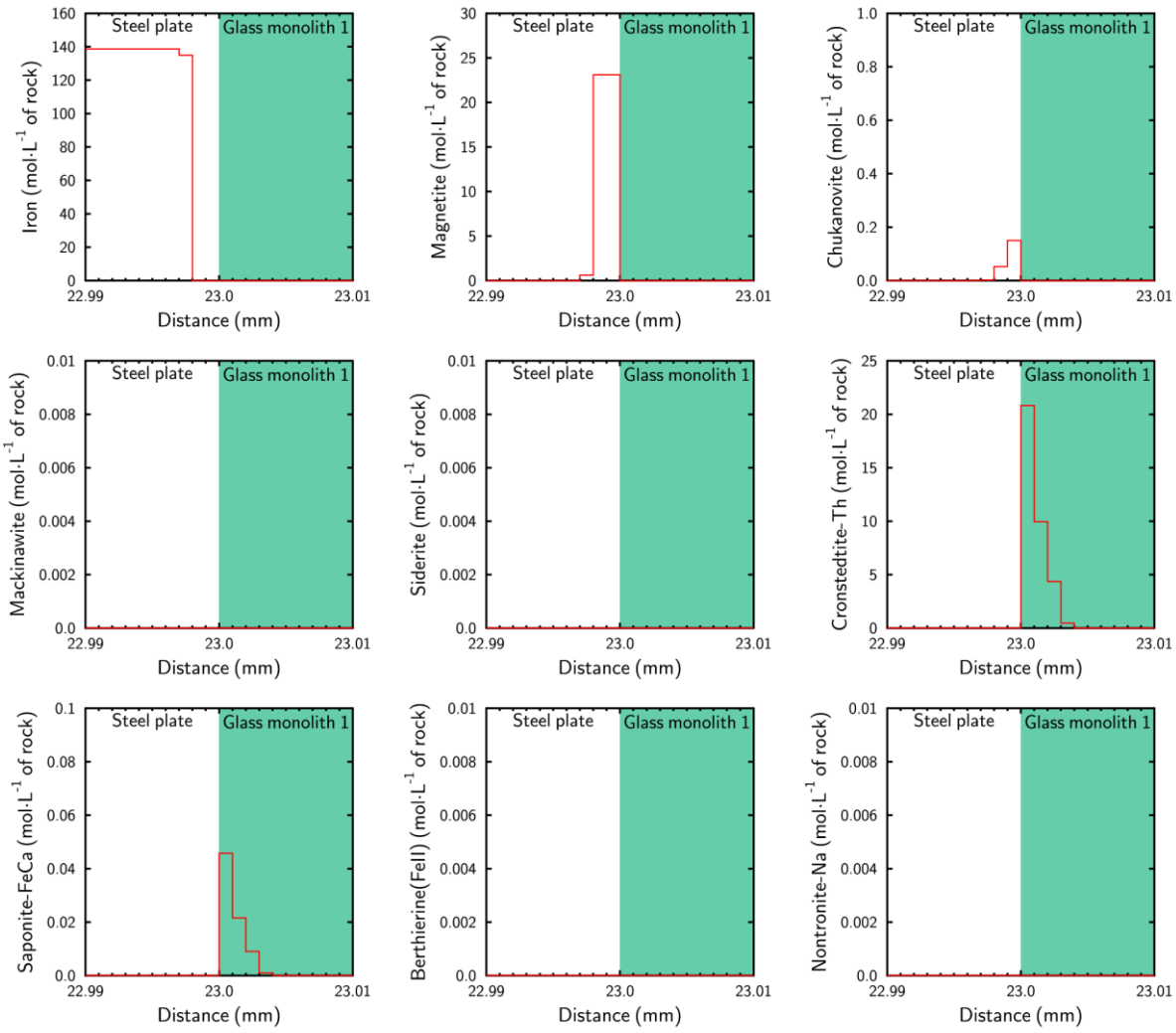

Figure 16. Corrosion products calculated with the BRGM model at the SON68 glass – carbon steel interface after 1 year in Experiment 3 at 70°C (area 3 in Figure 6).

Numerical results indicate the systematic presence of non-passivating gels and secondary phases zincsilite, natrolite, pimelite, hydroxyapatite and celestite that drive the glass alteration (*Figure 17*). The passivating gel (SiAl end-member) is only present at the glass corrosion front. The glass alteration of 3.2 µm after 1 year was in agreement with EDF observations. Indeed, the glass alteration measured by EDF varied between 2.4 µm at the edge of the monolith and 0.5 µm in the middle of the monolith. In the absence of information on corrosion products, we can only say that the thicknesses are in the same range.

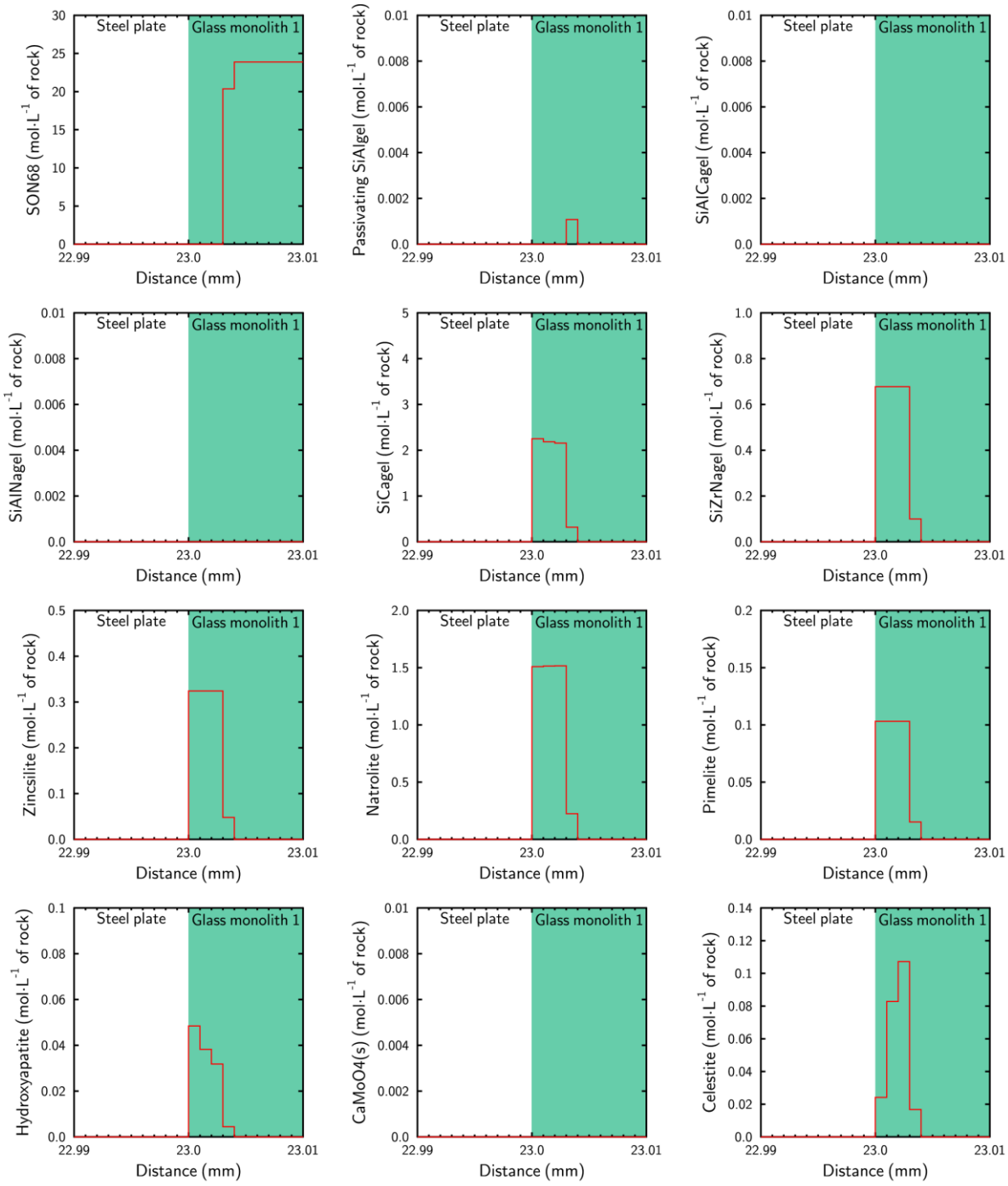

Figure 17. Glass alteration products calculated with the BRGM model at the SON68 glass – carbon steel interface after 1 year in Experiment 3 at 70°C (area 3 in Figure 6).

3.1.5.1.4 SON68 glass – stainless steel interface (area 3 in *Figure 6*)

The corrosion of the stainless steel in contact with the glass leads to the precipitation of magnetite, chukanovite, saponite-FeCa and cronstedtite-Th (*Figure 18*). A pH of 10 at 70 °C was predicted at the glass – stainless steel interface.

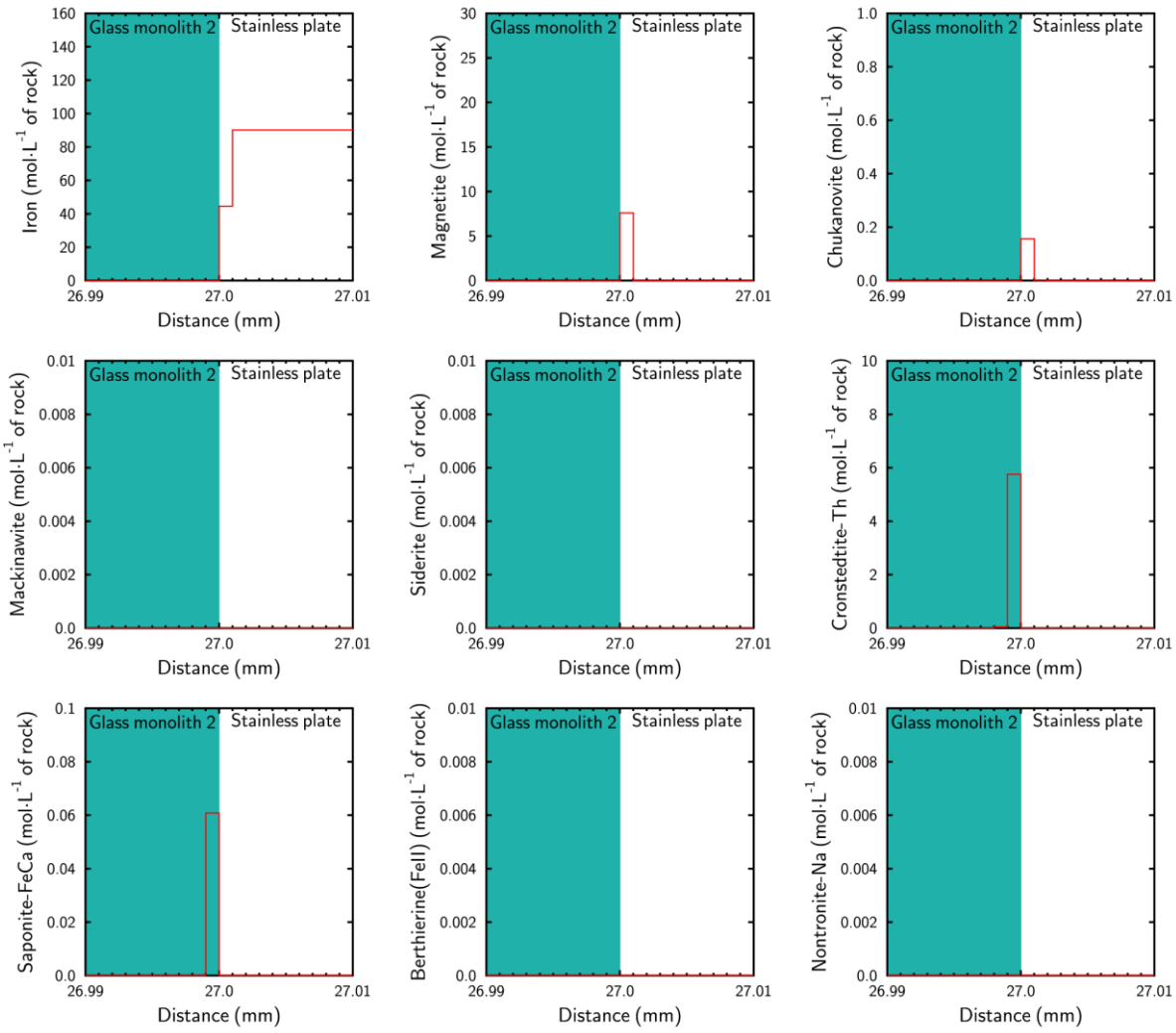

Figure 18. Corrosion products calculated with the BRGM model at the SON68 glass – stainless steel interface after 1 year in Experiment 3 at 70°C (area 3 in Figure 6.)

There was less glass alteration in contact with stainless steel (0.5 µm, *Figure 19*) than in contact with steel (3.2 µm, *Figure 17*). Consequently, the resolution (mesh size) does not enable to distinguish graphically the passivating layer from the gel layer anymore. The precipitation of iron silicate (i.e. cronstedtite-Th) was in competition with the formation of the passivating gel (i.e. SiAlgel), leading to an increase of glass alteration with the increase of the corrosion rate. As mentioned in section 3.1.5.1.2, the presence of Cr, Ni and other minor elements in the stainless steel was not considered.

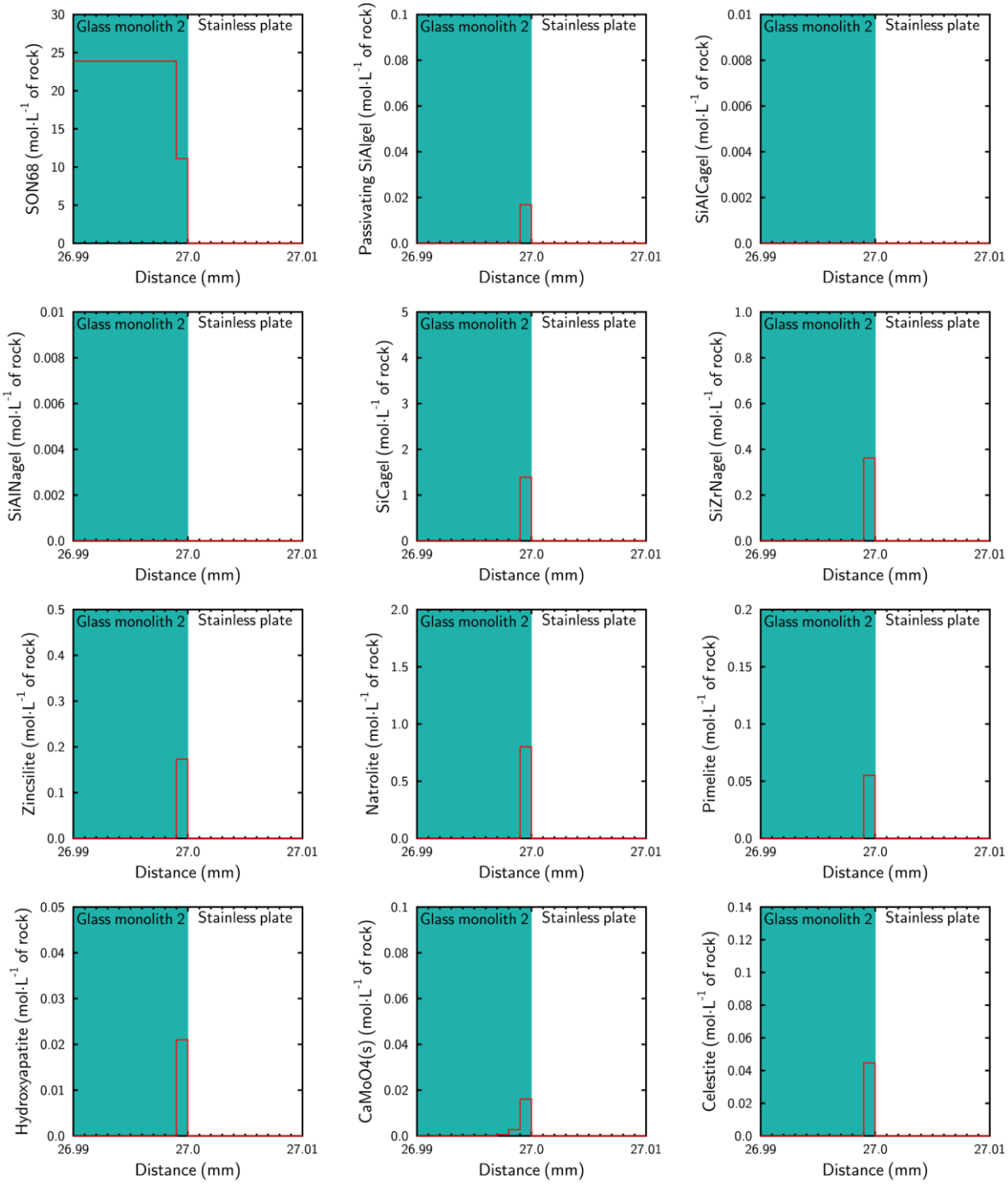

Figure 19. Glass alteration products calculated with the BRGM model at the SON68 glass – stainless steel interface after 1 year in Experiment 3 at 70°C (area 3 in Figure 6).

3.1.5.1.5 SON68 glass – glass interface (area 3 in *Figure 6*)

The alteration layer of glass at the interface between the two monoliths was only a few tens of nanometer thick (50 nm, *Figure 20*). Modelling indicated a massive precipitation of passivating gel leading to low alteration rate. The passivating gel was stable in absence of elements such as iron that can promote the glass corrosion through Si consumption.

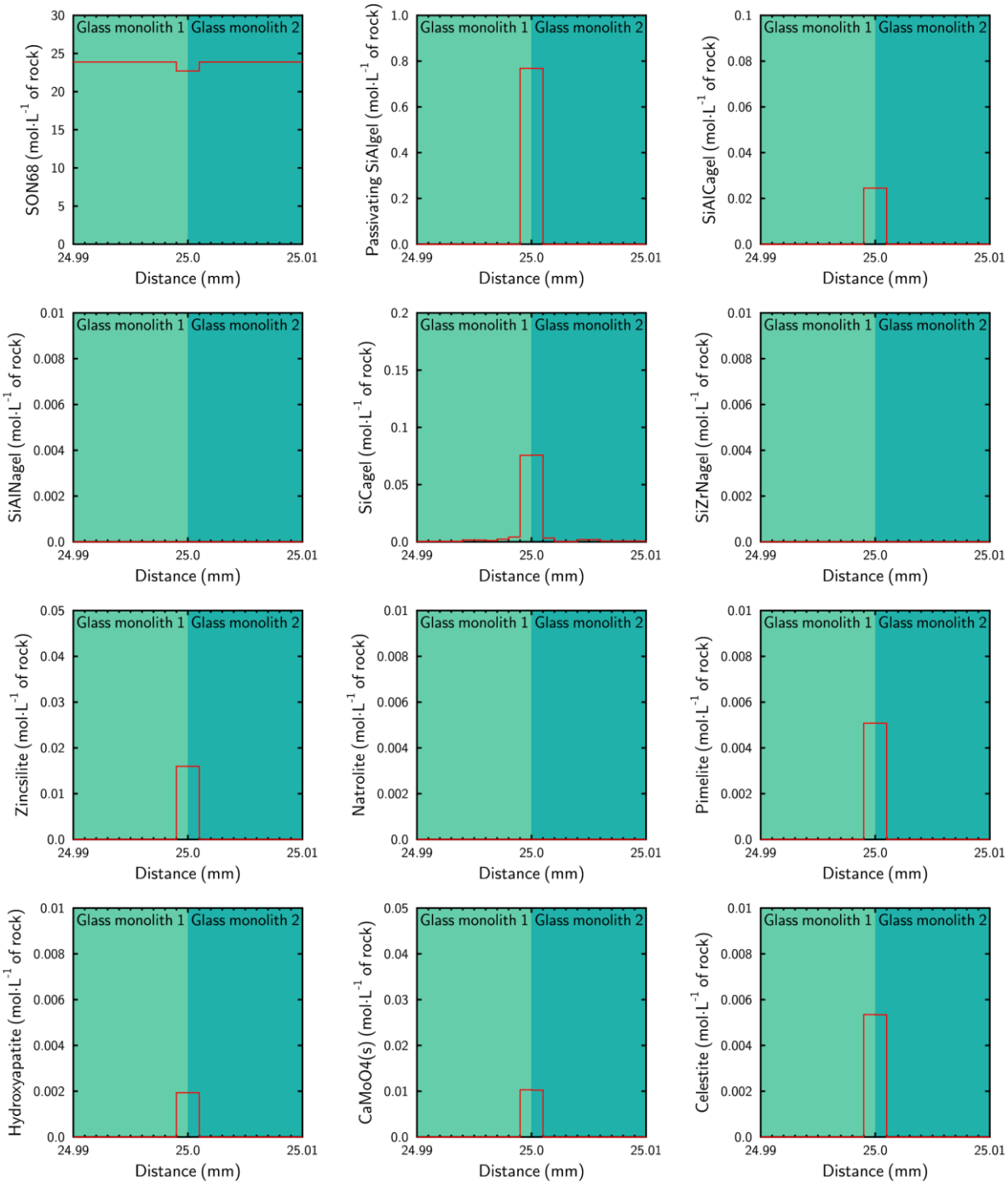

Figure 20. Glass alteration products calculated with the BRGM model at the SON68 glass – glass interface after 1 year in Experiment 3 at 70°C (area 3 in Figure 6).

3.1.5.2 Interactions in the micro-container without magnetite deposition (area 1 in *Figure 6*)

A 2D radial geometry was considered for the modelling of the interaction in the micro-container (*Figure 7*). This section is focused only on area 1 described in *Figure 6*. Indeed, the presence of a magnetite layer on the micro-container (area 2 in *Figure 6*) had negligible effects on the calculated mineralogical transformations, which were therefore not plotted. Such a behaviour was certainly related to our modelling strategy that assumed a constant corrosion rate regardless of the thickness of the corrosion product layer.

Unfortunately, experimental results are not available due to technical problems with the resin impregnation of the micro-container. The glass should be corroded more in front of the holes made in the container, however, characterization failed to confirm that because the glass powder did not remain in place. The numerical results are therefore mainly predictive.

3.1.5.2.1 COx alteration (area 1 in *Figure 6*)

The alteration of the clayey fraction of the COx (i.e. Ripidolite_Cca-2, Illite-Imt-2 and Montmorillonite-HCCa) and Quartz were kinetically controlled (*Table 2*). This led to negligible alterations of these minerals after 1 year of simulated time (*Figure 21*). Such a behaviour is in agreement with the experimental results available in the literature (Gaucher 2009).

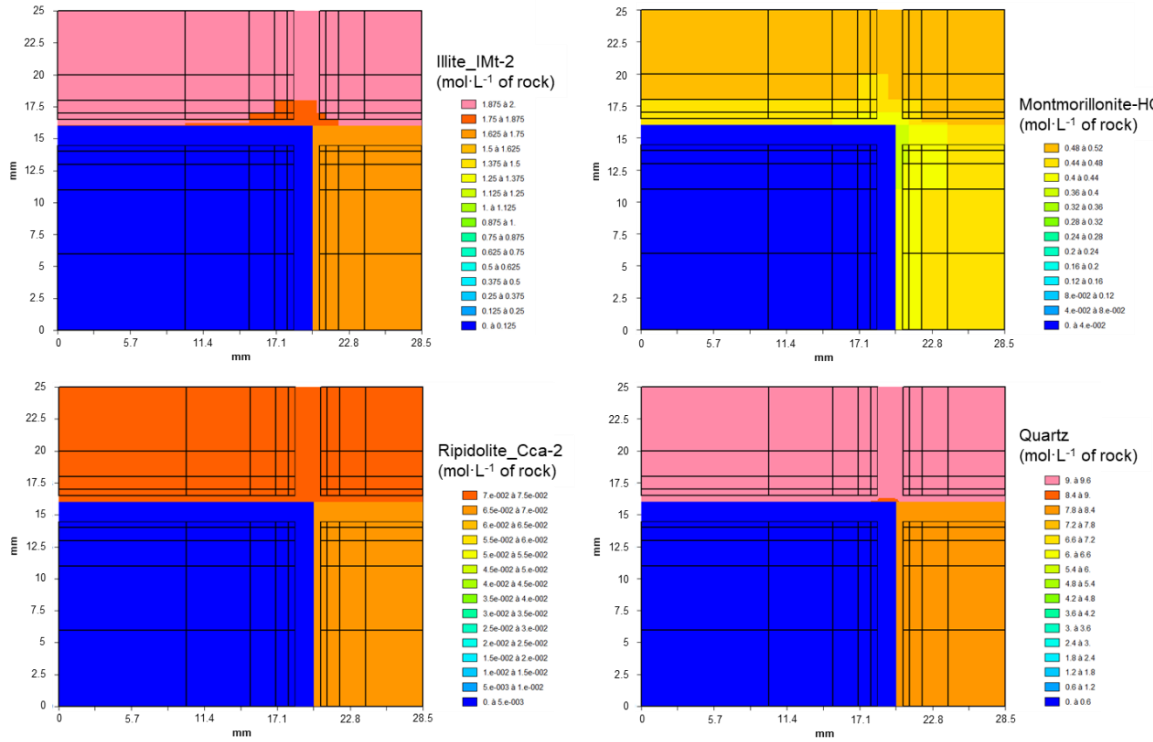

Figure 21. Alteration of clayey fraction of the COx (i.e. Ripidolite_Cca-2, Illite-Imt-2 and Montmorillonite-HCCa) and Quartz surrounding the micro-container after 1 year in Experiment 3 at 70°C (area 1 in Figure 6), calculated with the BRGM model.

The main transformations expected were the reduction of pyrite into pyrrhotite as well as the goethite dissolution (*Figure 22*). Reaction pathways were related to the diffusion of H_2 released by the iron corrosion. Note that the micro-container was assumed as a homogeneously permeable medium allowing thus the transport of H_2 produced by the corrosion of the external and internal parts of the micro-container. The alteration fronts were therefore larger than the ones expected from the modelling dealing with impermeable metallic plates (section 3.1.5.1).

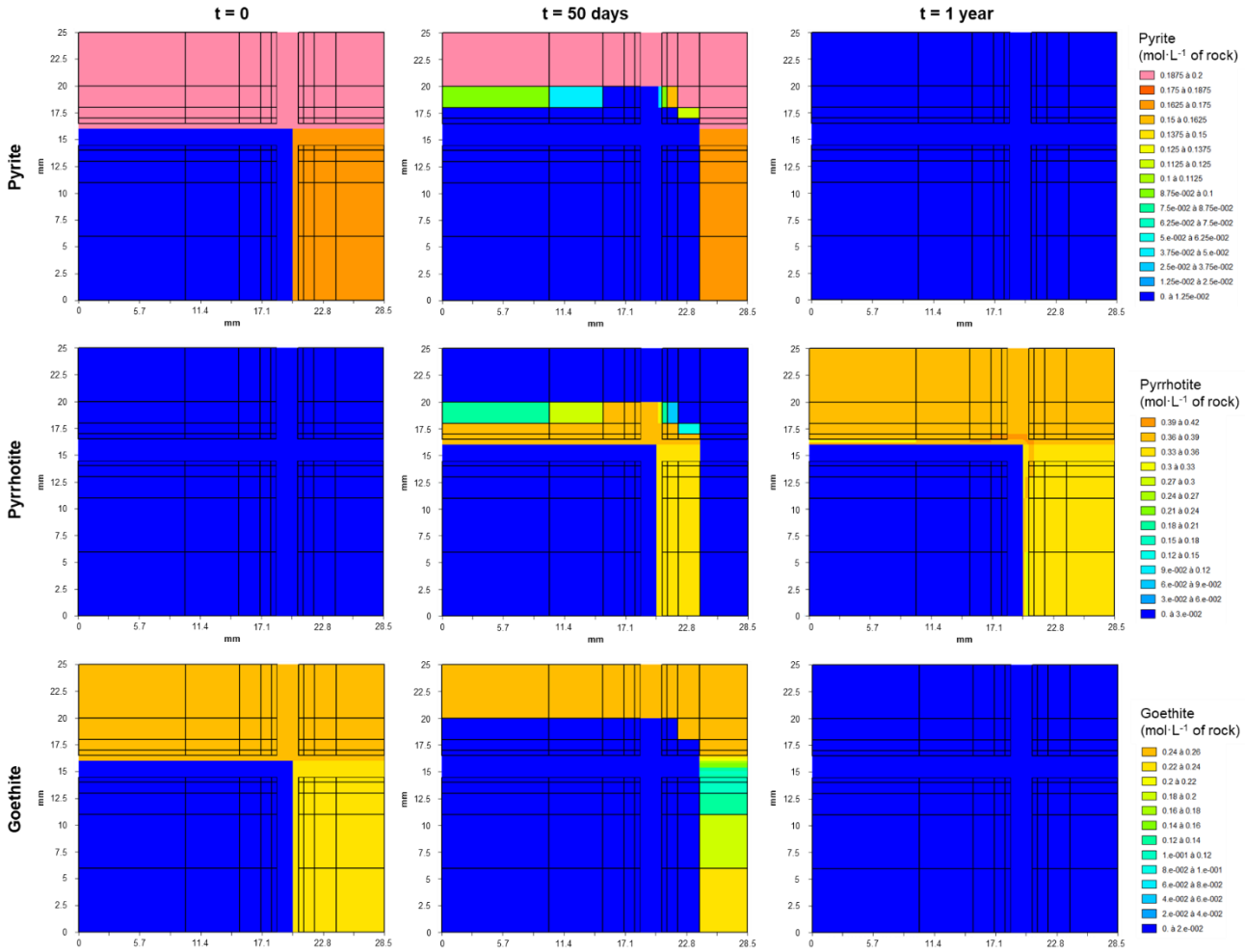

Figure 22. Pyrite – pyrrhotite conversion and goethite alteration surrounding the microcontainer up to 1 year in Experiment 3 at 70°C (area 1 in Figure 6), calculated with the BRGM model.

3.1.5.2.2 Corrosion of the micro-container (area 1 in *Figure 6*)

The modelling strategy (section 3.1.3.1) led to a preferential corrosion of the corner of the micro-container (*Figure 23*). The mineralogical transformations that can be expected in this zone are therefore more important. The pH increased up to 9.8 at 70 °C in this area.

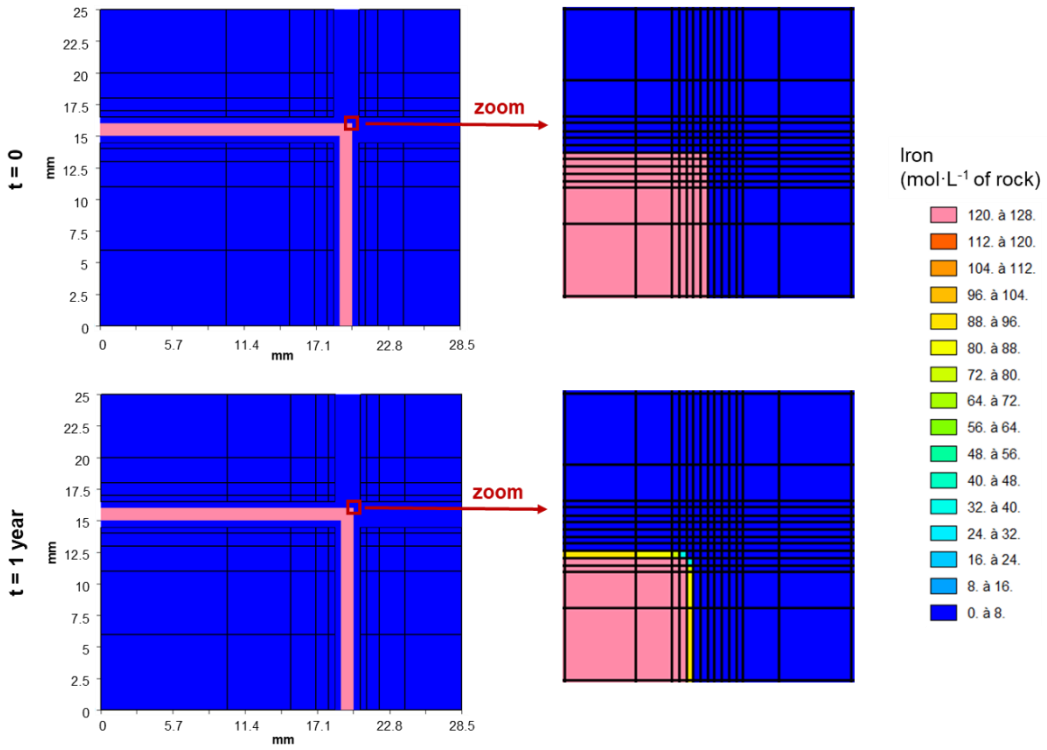

Figure 23. Corrosion of the micro-container in contact with COx clay after 1 year in Experiment 3 at 70°C (area 1 in Figure 6) calculated with the BRGM model

Magnetite is generally considered to be the main iron corrosion product in reduced environment (e.g. Chivot 2004, Marty 2010). This phase was predicted to precipitate on the whole steel surface exposed to the corrosion process and was particularly significant at the corner of the micro-container (*Figure 24*).

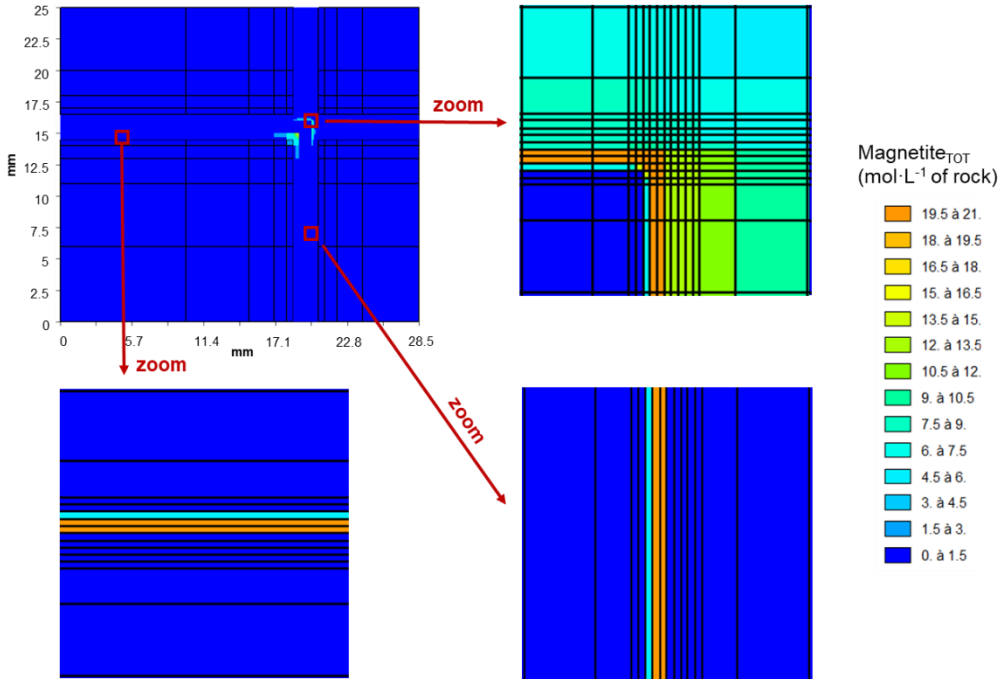

Figure 24. Magnetite precipitation on the micro-container in contact with COx clay *after 1 year in Experiment 3 at 70°C (area 1 in Figure 6) calculated with the BRGM model.*

The amount of precipitated chukanovite makes this mineral an important corrosion product (*Figure 25*). As for magnetite, the mineral was expected on the entire surface of steel exposed to the corrosion process. We note its formation directly inside the steel area located at the corner of the micro-container. Such a precipitation was possible because the perforated micro-container was considered as a porous and permeable medium. The modelled “iron/magnetite/chukanovite” sequence should be confirmed by observations.

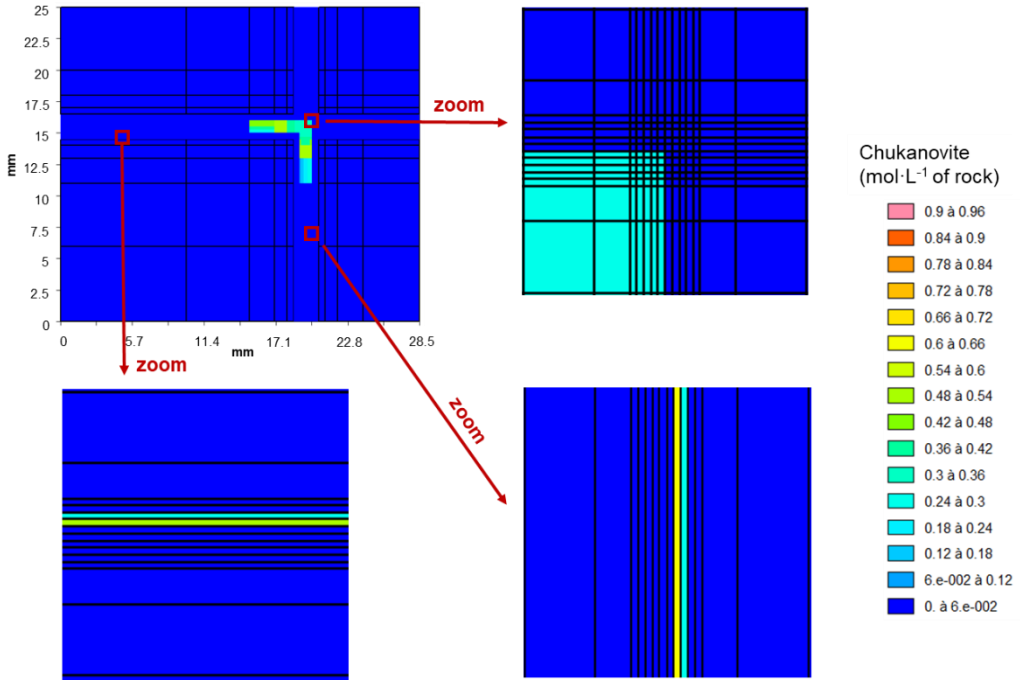

Figure 25. Chukanovite precipitation on the microcontainer in contact with COx clay *after 1 year in Experiment 3 at 70°C (area 1 in Figure 6) calculated with the BRGM model.*

Numerical results also indicated a precipitation of siderite (*Figure 26*) that was in competition with chukanovite for the incorporation of iron and carbonate. The high corrosion rate at the inside corner of the container led to a pH increase promoting the precipitation of chukanovite (inside the micro-container) rather than siderite (Azoulay 2012), while siderite is formed on the outside of the micro-container.

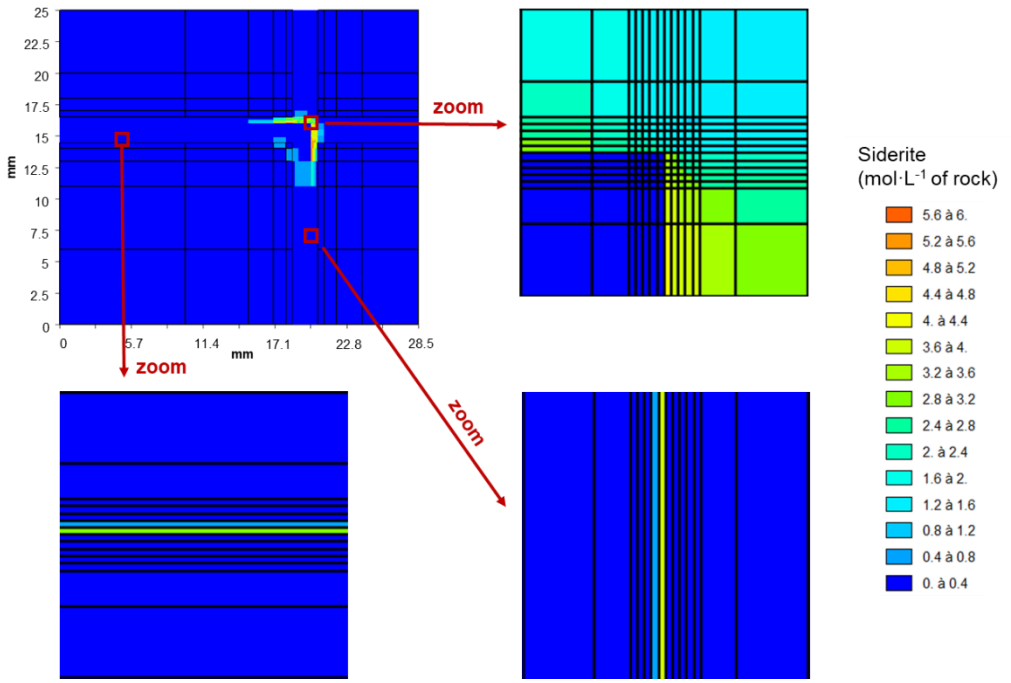

Figure 26. Siderite precipitation on the microcontainer in contact with COx clay *after 1 year year in Experiment 3 at 70°C (area 1 in Figure 6) calculated with the BRGM model.*

Mackinawite was also expected as a corrosion product *Figure 27*). The formation of the iron sulfur inside the steel area was possible due to the adopted modelling strategy (sections 3.1.3 and 3.1.4).

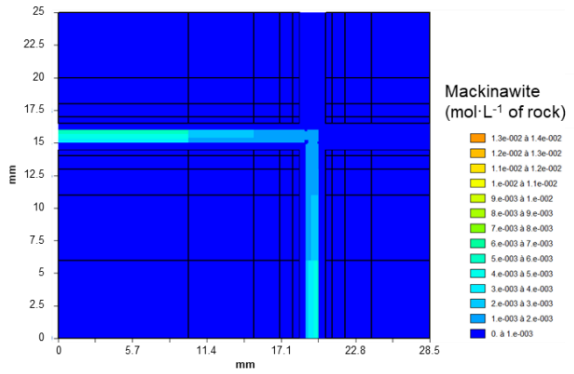

Figure 27. Mackinawite precipitation on the micro-container in contact with COx clay *after 1 year year in Experiment 3 at 70°C (area 1 in Figure 6) calculated with the BRGM model.*

The low clay alteration (e.g. Montmorillonite-HCCa, *Figure 21*) and the Fe release by the corrosion process promoted the precipitations of cronstedtite and saponite in the COx (*Figure 28*). Similar precipitations were also expected in the glass powder due to the significant Si release by the SON68 alteration. Cronstedtite was the main Fe-Si bearing mineral, regardless of the side considered (i.e. COx or glass powder), but the highest amounts were predicted in the glass powder. This secondary phase was mainly observed close to the corner of the micro-container, i.e. the area characterized by a high corrosion rate (*Figure 28*). The iron flux affected the nature of the corrosion products.

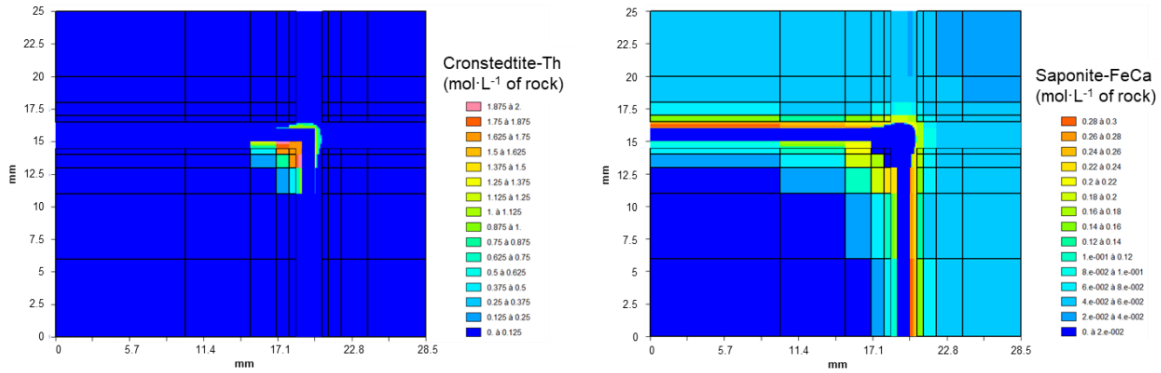

Figure 28. Precipitations of Cronstedtite-Th and Saponite-FeCa on the micro-container in contact with COx clay *after 1 year year in Experiment 3 at 70°C (area 1 in Figure 6) calculated with the BRGM model.*

In contrast, the formation of berthierine was only predicted in the COx side (*Figure 29*). To our knowledge, its formation has been only observed in the case of iron – clay interactions (e.g. Rivard 2013).

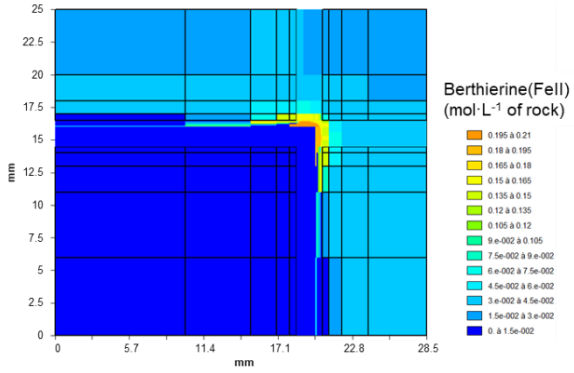

Figure 29. Precipitation of Berthierine(FeII) on the micro-container in contact with COx clay *after 1 year in Experiment 3 at 70°C (area 1 in Figure 6) calculated with the BRGM model.*

3.1.5.2.3 Alteration of the SON68 glass powder and gel formation (area 1 in *Figure 6*)

The use of the GRAAL model implies an alteration of the glass powder that is inversely related to the predicted amount of passivating gel. Therefore, the absence of passivating gel in the corner of the micro-container led to the highest glass alteration (*Figure 30*). The gel formation was limited in this area due to a competition with ferrous silicate minerals (i.e. cronstedtite, *Figure 28*) that consume silica and sustain the glass alteration rate (glass corrosion is function of silica concentration in solution).

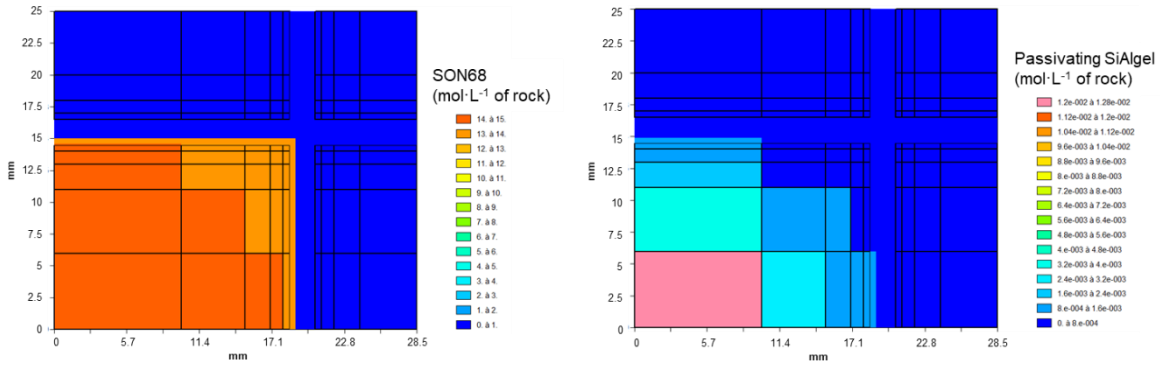

Figure 30. SON68 glass alteration and passivating-gel formation after 1 year year in Experiment 3 at 70°C (area 1 in Figure 6) calculated with the BRGM model.

In contrast to the modelling of the system with metallic plates and glass monoliths, only two non-passivating gels were predicted as glass alteration products (*Figure 31*). This is probably due to the higher glass surface area to solution volume for the glass powder.

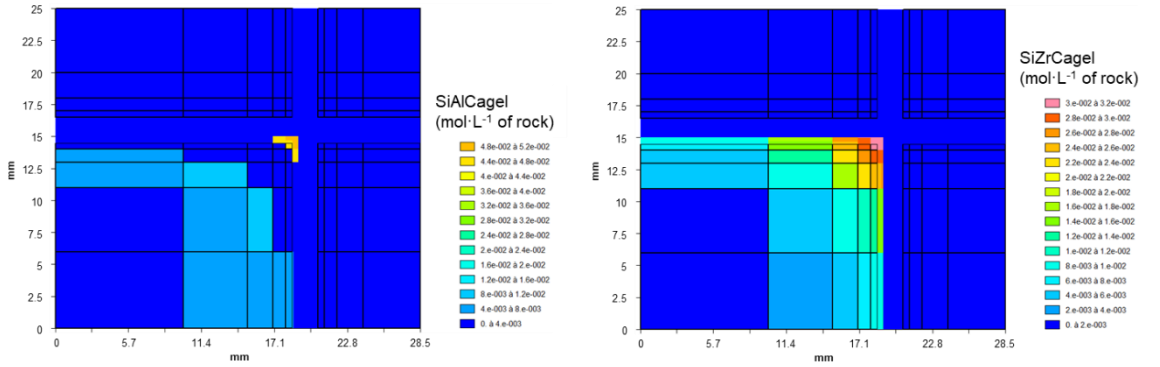

Figure 31. Precipitation of non-passivating gels with SON68 glass after 1 year in Experiment 3 at 70°C (area 1 in Figure 6) calculated with the BRGM model.

Glass alteration products (zincsilite, natrolite, pimelite, hydroxyapaptite and celestite) that control in the model the concentrations of minor elements (e.g. Zn, P, Ni) present in the glass are also predicted (*Figure 32*).

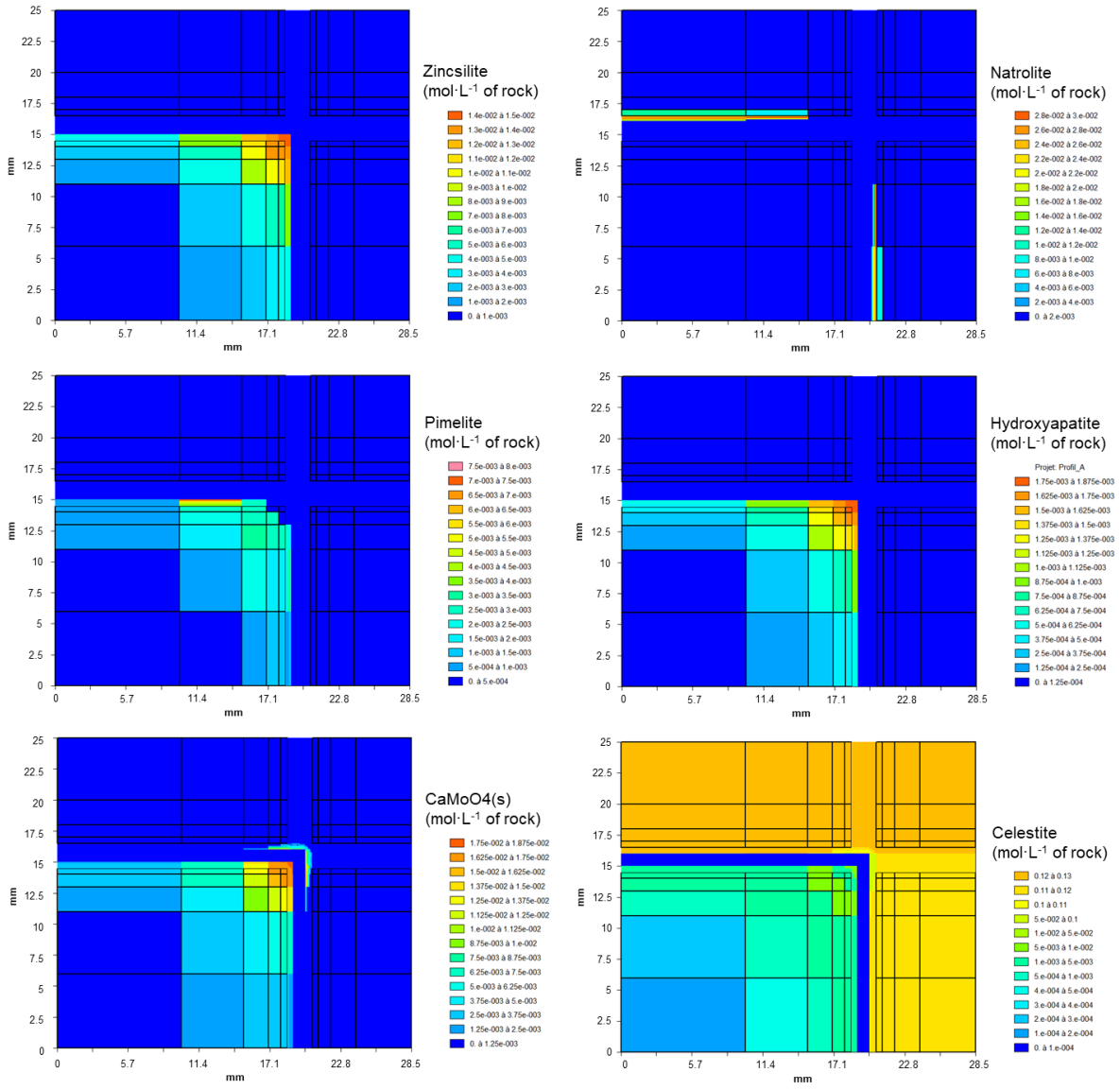

Figure 32. Precipitation of Zincsilite, Natrolite, Pimelite, Hydroxyapatite, $CaMoO_4$(s) and Celestite after 1 year of simulated time with SON68 glass in Experiment 3 at 70°C (area 1 in Figure 6), calculated with the BRGM model.

3.1.6 Conclusions for the modelling of Experiment 3 (glass/steel/COx clay)

- The glass alteration gels were experimentally observed. It was therefore necessary to ensure that they were present in the numerical simulations. This led us to discard some mineral phases for which the precipitation by lack of kinetic control led to a too strong competition with the formation of passivating and non-passivating gels. The choices made in the selection of secondary phases allow describing the main mechanisms (pH increase due to steel corrosion, and Si consumption due to the formation of Fe-bearing silicates) that drive the glass alteration.

- In addition, the modelled gel thickness agrees within the uncertainties with the range of measurements of the alteration layer in the experiments (i.e. 1.4 ±0.1 and 0.4 ±0.1 µm in contact

with steel and stainless steel, respectively). Numerical results showed that glass alteration increased with the increase of the steel corrosion rate; the formation of a passivating gel was in competition with the precipitation of Cronstedtite-Th. This phase was identified at the iron – glass interface in task 3.1.

- The use of the GRAAL model in the context of iron/glass interaction required some caution in the resolution of kinetic reactions.

- The GRAAL model indicated that the glass alteration is promoted at the iron/glass interface: dissolution of the passivating gel promotes the glass alteration. This confirms the experimental observations, showing a large difference in the glass alteration layer thickness depending on the distance from the steel. Close to the steel, the layer was several µm thick, while the glass particles situated at a distance of 0.5 mm or more from the steel remained unaltered.

- Si is consumed due to the precipitation of secondary iron phases (greenalite, cronstedtite). The glass alteration is therefore function of the corrosion model (i.e. release of Fe^{+2} to the glass powder).

- The steel corrosion was simulated by a layer-by-layer approach.
    - Apart from the modelling presented here, only few studies (Bildstein 2017) have attempted to simulate a layer-by-layer corrosion. This approach closely reproduced the mineral paragenesis observed in experiments (Bildstein 2017). Moreover, it could be used with more complex kinetics taking into account the effect of the pH, the temperature, the O_2 partial pressure and/or the presence of a passivating layer on the steel/iron corrosion rate. The adopted simulation strategy allows Fe^{2+}, OH^- and H_2 fluxes directly localized at the interfaces with other materials. The numerical results showed that these concentration gradients affected the quantity but also the nature of the corrosion products. Different corrosion products are formed on the glass side and the COx side. See for example Cronstedtite in *Figure 28*.
    - The corrosion model had some limitations that may affect glass alteration. The main one originates from the corrosion rate assumed constant. Moreover, the restricted selection of secondary phases, but also assumptions made on the conversion of iron into magnetite, constrained the model to form the corrosion products observed experimentally over short times. These may not be the ones that will formed in the repository over a significantly longer time.
    - The layer-by-layer corrosion was applied also for the modelling at waste package scale (section 4.3)

- Experiment 3 was carried out in fully saturated conditions (short time scale). $H_2(g)$ generation should be considered for modelling at the waste package or disposal scale, but MARTHE-PHREEQC have limitation on this aspect.

- MARTHE-PHREEQC uses a sequential non iterative approach (SNIA) to solve mass transport and chemistry. This, combined with a high mesh refinement of interfaces and the use of kinetic reactions, leads to high computation times: 3 weeks of calculation to simulate 1 year (case of 2D simulations). Hence simplification was required for modelling at the waste or disposal scales. As shown in section 4.3 the grid size was increased to 5 mm for this purpose.

Overall, the numerical and experimental results dealing with metallic plates and glass monoliths are in good agreement, supporting the use of the simulation assumptions for extrapolation to generic cases.

3.2 Modelling of glass/steel/cement-bentonite/clay interaction by BRGM

The experimental setup presented in section 3.1 was used also to study the interaction glass/steel/cement-bentonite grout/clay, where the clay was Callovo-Oxfordian claystone (COx.

The results of the modelling by BRGM of this experiment (similar to Experiment 3 in D2.12) were not yet available when this report was finalized. Hence the results are not included. A publication was in preparation though (Grangeon, to be published).

3.3 Modelling of Experiment 4 (glass/steel/cement) by SCK CEN

3.3.1 Introduction of the model and experiments

3.3.1.1 Summary description of the experiment

The experiment modelled here was described in EURAD-ACED deliverable D2.10 (Gin 2019) as Experiment 4. Here we only give a short summary of the experimental setup (*Figure 33*) and method.

The interaction between glass and OPC paste was studied at room temperature in stainless steel cells that had on one side a compartment that was filled with glass powder, while the rest of the cell was filled with hardened OPC paste (water/cement ratio of 0.4). These tests were thus integrated mockup tests, designed to study the coupling of glass dissolution and reactions with the cement paste via diffusion through the interfaces in a geometry that is similar to the geometry expected in disposal conditions.

Tests were done with the reference glasses SON68 and SM539. The glass compartment was separated from the hardened cement paste (HCP) compartment by a stainless steel filter. This filter represents in a simplified way the steel corrosion product layer expected to be formed in disposal conditions. The HCP compartment had sampling holes that were filled regularly with young cement water ('YCWCa', pH 13.7) before the start of the experiment. To speed up the saturation of the cement paste with water, the cells were simultaneously percolated with cement water under pressure. As soon as water started percolating, implying that the glass compartment was also filled with cement water, the cells were disconnected and the actual static leaching tests started (= formal time zero of the glass leaching). The water in the compartments was regularly sampled and analysed. After about 2.5 years (April 2012), all remaining water in the sampling holes was collected in a last sampling (= formal end of glass leaching). The cells stayed like this until February 2014 (cell with SM539) and June 2015 (cell with SON68), when the remaining pore water was removed by connecting the cells to a vacuum pump. The cells were dismantled in June 2016 for a first series of analyses of the (altered) cement paste and glass, and then used further for a more detailed solid analysis in Task 3.1 of EURAD-ACED. The results of the analyses are given in EURAD-ACED deliverable D2.12 (Gin 2022).

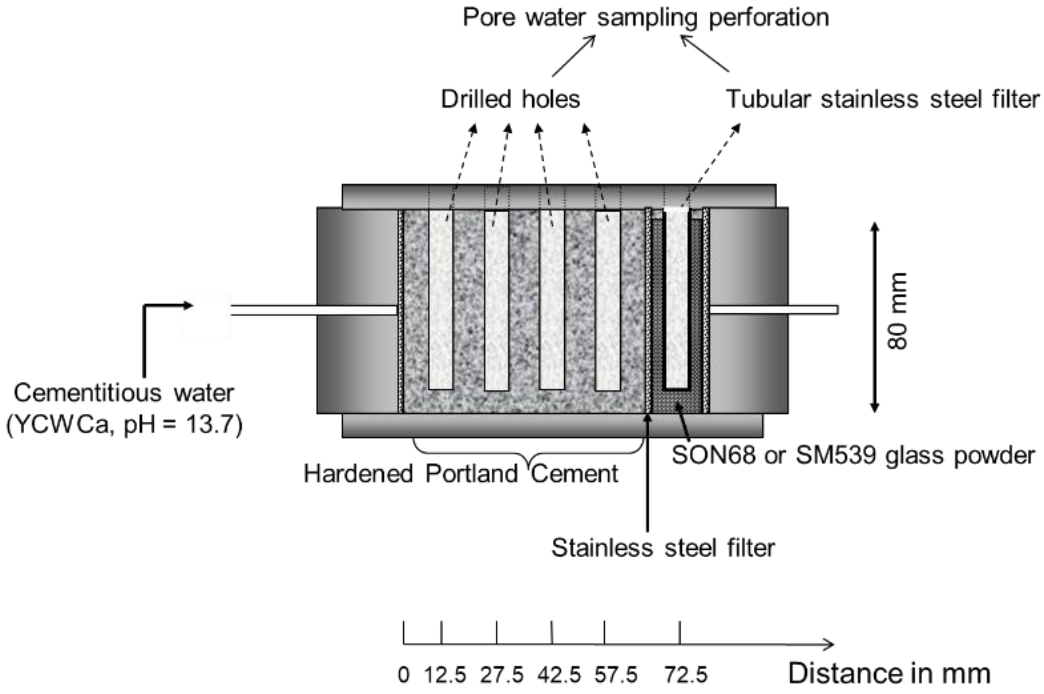

Figure 33. Experimental setup for the integrated tests of Experiment 4 (hardened ordinary Portland cement paste/stainless steel filter/glass powder at room temperature)

3.3.1.2 The reactive transport model

One dimensional reactive transport modelling was applied to model the described system. The model has been used before to model concrete/clay interaction (Liu 2014) and has also been benchmarked against other reactive transport modelling codes such as MIN3P, TOUGHREACT and HYTEC (Marty 2015). Basically, the model solves Fick's second law of diffusion in 1D or 1D radial system using a finite difference method, and couples the module-based PHREEQC for chemical reactions. The coupling was done through a sequential non-iterative approach (SNIA), i.e., chemical reactions are calculated after each transport time step and before proceeding to next transport time step and so on.

Figure 34 is the conceptual model of the experimental system. Since the pH at the glass/cement interface stayed high (about 13.7) during the whole experiment, iron reaction was expected to be slow, and thus neglected. The iron filter with a thickness of 2.5 mm and a porosity of 0.34 served only as an inert porous medium separating the glass and cement.

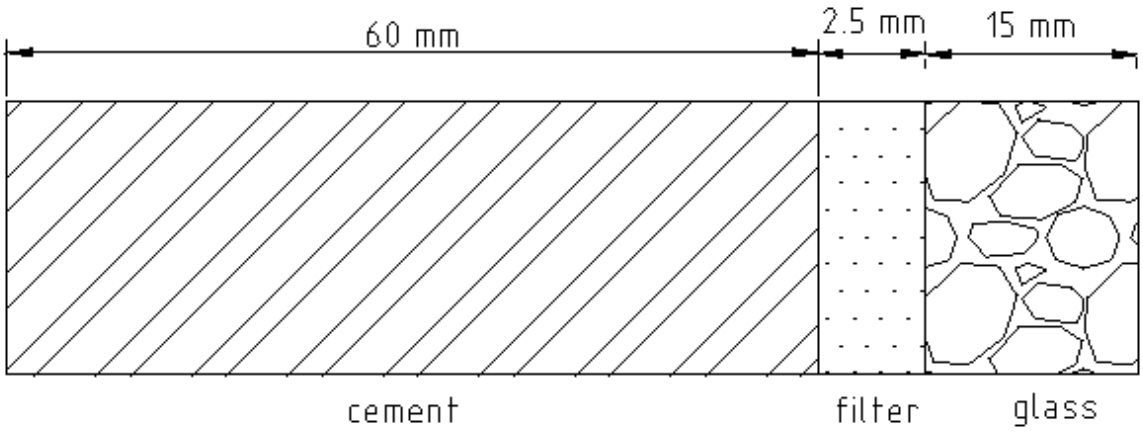

Figure 34. Conceptual model for the glass/iron filter/cement system in Experiment 4 (SCK CEN model).

In the conceptual model the glass compartment was treated as one grid cell with a fixed solution volume and glass dissolving kinetically. The rate of the glass dissolution follows 1/sqrt(time) according to previous experimental and modelling results (Liu 2015, Mann 2019, Liu 2019). The model for glass dissolution is similar to the models described by Liu in an earlier paper (Liu 2019). It is assumed that there is a sharp diffusional front advancing proportionally to square root of time, i.e., glass dissolution is treated as a moving boundary problem or Stefan problem. The diffusive flux for elements from the glass were calculated semi-analytically, and converted to concentrations in the glass compartment. Since this model requires both congruent dissolution at the dissolution front and a non-moving initial glass surface, precipitation or local reorganization reactions, mainly reaction of Si and Al and non-soluble elements such as Ca and Fe, are assumed to compensate the retreat of the initial glass surface. Easily soluble elements such as B and alkalis will be released congruently into the ambient solution.

Three diffusion coefficients are required for the modelling of such a system: (1) a diffusion coefficient in the glass (2) a diffusion coefficient in the iron filter, and (3) a diffusion coefficient in the cement. The diffusion coefficients in the glass and cement are fitting parameters in the modelling. The diffusion coefficient in the iron filter is related to the porosity of the iron filter through an Archie's law type relationship with the porosity raised to the power of 2.

$$D_e = D_{aq}.n^2 \qquad \text{(Equation 3.3)}$$

In this equation D_e is the effective diffusion coefficient, D_{aq} is the aqueous diffusion coefficient and n is the porosity of the iron filter.

3.3.1.3 The glass dissolution model

The basic assumptions for the glass dissolution model are given in the previous section. On the one hand, the glass dissolution or solvation of glass network former and modifier elements by alkaline hydrolysis is stoichiometric according to the concept of interfacial coupled dissolution and precipitation (e.g., Hellmann 2015), but on the other hand, not all solvated elements from the glass are fully released into the ambient solution. For certain solvated elements such as Si, Al, Ca and Zr, precipitation or local reorganization integrates them back into the glass alteration layer (GAL) together with alkalis (K, Na) from the solution, to form a hydrated silica gel, i.e. glass dissolution is assumed to be congruent at the dissolution front, but because of the reprecipitation the concentrations in solution do not reflect the congruency. Additionally, the GAL is assumed to directly replace the space filled by the initial glass powder without change in volume. Like the GRAAL model (Frugier 2018), the model thus assumes isovolumetric dissolution and an increase of the glass alteration layer thickness proportional to the square root of time. We have no direct evidence for this hypothesis from measurements of layer thicknesses for different test durations, but this assumption allows to fit the parabolic increase of the boron (glass dissolution indicator) solution concentration with time or the linear increase with the square root of time. Moreover, with the proposed D_{glass}, a (theoretical) thickness of 0.25 µm for SON68 and 0.30 µm for SM539 is calculated, which fits with the SEM layer thickness of <1µm for the particles in the bulk of the glass compartment.

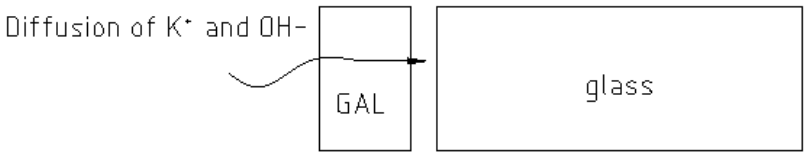

Figure 35. Schematic drawing of the 1 D glass dissolution model used for the modelling of Experiment 4 (SCK CEN model).

Elemental fluxes from the glass were calculated semi-analytically, and converted to concentrations in the glass compartment. Dissolution of glass powders is a 3-D problem. However, due to the large surface area of glass powders and because less than 5% of the total glass powder has been altered at the end of the experiments, the thickness of the glass alteration layer is very thin and thus the reactive surface area change due to the radius change of the glass powder is negligible. Hence the 3-D dissolution is simplified to 1 D, as shown in *Figure 35*, with the kinetic rate reaction as follows

$$\alpha(t)^2 = k \cdot t \qquad \text{(Equation 3.4)}$$

In Eq. 3.4 k is the reaction constant, t is the time and α(t) is the fraction of reacted glass which is calculated as

$$\alpha(t) = \frac{m(t)}{m_0} \qquad \text{(Equation 3.5)}$$

where m(t) [g] is the amount of reacted glass at time t and m_0 [g] is the initial amount of the glass. Since boron is often used as a dissolution indicator, the amount of the reacted glass is calculated based on the amount of boron released from the glass according to the following equation

$$m(t) = \frac{C_B V}{\chi_B} \qquad \text{(Equation 3.6)}$$

In this equation C_B [g/L] is boron solution concentration, V [L] is the solution volume and χ_B [dimensionless] is the weight percentage of boron in the glass.

In *Figure 35*, the growth of the GAL is assumed to be fast enough compared to the diffusion of reactants such as K, Ca and OH from the solution to the interface between GAL and pristine glass, i.e., diffusion of those reactants through the GAL becomes the limiting process. *Figure 36* shows how the dissolution rate evolves based on Equation 3.4.

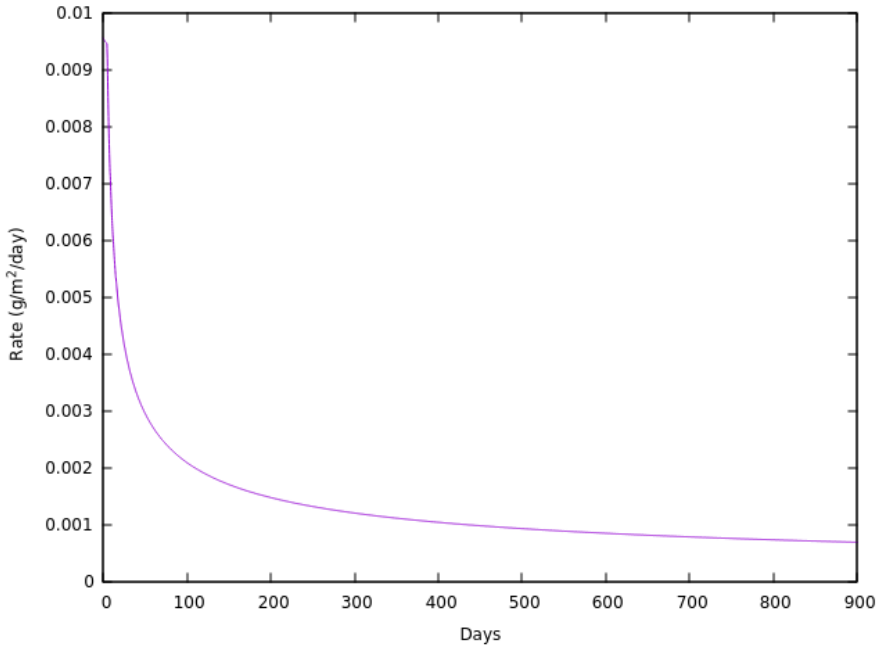

Figure 36. Evolution of SON68 glass dissolution rate according to Equation 3.4, used to model Experiment 4 (SCK CEN model).

The model does not make any distinction between glass particles close to the stainless steel filter and glass particles further away. Still, for SM539, the particles close to the stainless steel filter had thicker alteration layers. The faster dissolution of these particles would correspond to a more porous GAL, with a multilayered structure. The faster alteration close to stainless steel filter is an indication for deviating local conditions, but this is not included in the glass dissolution model.

The glass dissolution model that is used for the tests in very alkaline conditions, is very different from the models normally used for experiments in less alkaline conditions, where a protective layer is assumed to be formed after saturation of the solution with the components that stabilize this layer. At high pH, pseudo-equilibrium of solution with glass phase is unlikely though, because of the very high SiO_2 solubility. The use of a diffusion-controlled glass dissolution model has important consequences:

- In the diffusion model, the value of D_{glass} incorporates all processes related to dissolution kinetics and affinity. A high glass dissolution rate is explained by a large D_{glass}.
- In this model the dissolution rate does not depend on the silicon concentrations via an affinity term, but indirectly the silicon concentrations can have an effect on the diffusion properties of the glass alteration layer, because the Si concentrations in solution are assumed to be in equilibrium with the GAL, where Si containing phases have an effect on the density and porosity, affecting the diffusivity of the layer.
- A high dissolution rate (large D_{glass}) would correspond to a more porous glass alteration layer; the porosity will depend on the phases that constitute the glass alteration layer, and these will be influenced by the concentration of (a.o.) Si in solution. Specific studies to look at the influence of high Si concentrations on the glass dissolution rate at high pH have not been performed.
- The model must be adapted for the short term to include the initial rate (for SON68 at 30°C in young cement water, this would be 0.04-0.08 $g \cdot m^{-2} d^{-1}$, see ref. Caes 2020), because a diffusion controlled dissolution for t = 0 would be infinitely high.
- The dissolution rate becomes infinitely small on the long term; hence extrapolation to the long term leads to very low dissolution rates that cannot be demonstrated experimentally; a 'residual' rate is necessary when the model is extrapolated to avoid likely underestimation of the long-term dissolution rate (e.g. using the minimum rate measured experimentally)
- The dissolution rate of glasses is known to be larger for a smaller ratio of glass surface area to solution volume (SA/V). Hence the SA/V ratio is an implicit model parameter; a realistic value should be selected for use under in-situ conditions.
- At high SA/V, the initially high pH can decrease because of glass dissolution, and the dissolution mechanism can change.
- The model can fit data in young cement water (pH 13,5), but was not validated in evolved cement water (pH 12.5, portlandite controlled). In old cement water (pH ≈ 11), where very low dissolution rates have been measured (Lemmens 2019), an affinity model may be applicable.

3.3.1.4 The cement hydration model

Cementitious materials have been commonly treated as porous media in reactive transport modelling. The mineralogy and pore solution composition of cementitious materials are required as initial conditions in reactive transport modelling. For a given cement and water to cement ratio, those parameters can be obtained via a cement hydration model, i.e., a series rate equations to transform cement clinker phases into cement hydration products. *Table 3* shows the amounts of each clinker phase per 100 g cement used in the experiments. The rate equations and parameters for the four major clinker phases C_3S, C_2S, C_3A and C_4AF were based on a paper by Bernard et al. (Bernard 2003). For the other clinker phases in Table 1 hydration reactions were assumed to proceed via chemical equilibrium. Na, K, S and Mg oxides partially form solid solutions with the four major clinker phases and dissolve congruently with these phases (Lothenbach 2006, Taylor 1997). Additionally, Na and K sorption onto CSH1.6 were modelled as the following sorption reactions:

$$Csh\_wOH + Na^+ = Csh\_wOHNa^+ \qquad \textit{(Equation 3.7)}$$

$$Csh\_wOH + K^+ = Csh\_wOHK^+ \qquad \textit{(Equation 3.8)}$$

In the above reactions Csh_wOH is the master surface species associated with CSH1.6. The site density and specific surface area for CSH1.6 were based on the literature, e.g., 4.82 sites per nm^2 for C-S-H (Krattiger 2021, Labbez 2011) and 32 $m^2 \cdot g^{-1}$ (Beaudoin 2019), respectively, which resulted in 0.05 mol sorption sites per mol of CSH1.6. Note that there are some variations in both parameters in the literature.

The reaction constants are fitting parameters to ensure that: 1) the distribution coefficients for Na and K between CSH1.6 and the pore solution agree with the literature; 2) the modelled Na and K porewater concentrations are in agreement with the measurements. For simplicity, the reaction constants were taken the same for Na and K , assuming that there is no preferential incorporation of either cation (Hong 1999). A recent study by Miron et al. confirmed that the difference in uptake of Na and K in C-S-H is very small (Miron 2022).

PHREEQC 3 (Parkhurst and Appelo 2013) together with the Thermochimie version 11a (Blanc 2015) database were used to calculate chemical reactions. Selection of secondary minerals (hydration products) were based on commonly reported hydration products in the cement literature (e.g. Lothenbach 2006, Taylor 1997) and the reaction of those minerals were assumed to be at chemical equilibrium.

Clinkers	Mass%
C_3S ($3CaO.SiO_2$)	62
C_2S ($2CaO.SiO_2$)	14.5
C_3A ($3CaO.Al_2O_3$)	12.1
C_4AF ($4CaO.Al_2O_3.Fe_2O_3$)	2
K_2SO_4	0.65
Na_2SO_4	0.068
MgO	1.25
$CaSO_4$	4.16

Table 3. Composition of cement (per 100 g) in Experiment 4 used in the SCK CEN model.

Remark about the hydration model: The equations used in the hydration model are similar to those in the other hydration models, i.e. the Avrami and Jander equations (Avrami 1939, Jander 1927), or modified Jander equations, such as Ginstling-Brounstein (GB) equations. The widely-followed formulation of Parrot & Killoh (Parrot and Killoh 1984) also uses similar equations. Equation 3.7 and 3.8 are based on the surface complexation model of Dzombak and Morel (1990), and have already been implemented in PHREEQC. Basically this model includes ion association with a charged surface through the Boltzmann term (e.g. Dzombak and Morel, 1990). Alternatively, cation exchange reactions could be used for alkali uptake, but then the reaction should be highly pH-dependent, and there should be a decrease in the pore solution pH. If alkali exchanges for Ca^{+2} instead of H^+ in the C-S-H, then there should be an increase in the Ca solution concentration with the alkali uptake. The experimental results don't seem to support such ion exchange process. The apparent charge imbalance in Eq. 3.7 and 3.8 is due to the presence of a charged surface in the model. So even if there is no charge balance in the solution, the system 'solution + solid' is charged balanced.

3.3.2 Results of the modelling of Experiment 4 (glass/steel/cement) by SCK CEN

3.3.2.1 Modelling of the hardened cement paste

Based on the cement composition in *Table 3* and a water to cement ratio of 0.4, the pore water composition, mineral composition and porosity after 40 days of hydration can be obtained as shown in *Table 4* and *Table 5*.

As shown in *Table 4*, the model tends to overestimate the Al concentration, and to underestimate the Ca concentration. The large difference for sulphate come from the fact that the synthetic cement water that was used to saturate the system had a low sulphate concentration.

.

Species	Modelled ($mg \cdot L^{-1}$)	Measured ($mg \cdot L^{-1}$)
Al	7.4	0.82 ± 0.27
Ca	17.2	65 ± 7
K	14574	13471 ± 515
Na	3519	3403 ± 114
$SO_4^{(2-)}$	2117	1035 ±208
Si	14.1	14 ± 9
Mg	≈ 0	0.36 ± 0.21
Fe	0.27	0.18 ± 0.06
pH	13.6	13.6 ~ 13.9

Table 4. Modelled pore water composition in concrete after 20 days of hydration in Experiment 4, compared to the concentrations measured in the HCP compartment during the experiment (SCK CEN model).

Phase	Chemical formula	Volume fraction (%)	Observed
Monocarboaluminate	$(CaO)_3Al_2O_3:CaCO_3:10.68H_2O$	2.37	yes
C3FH6	$Ca_3Fe_2(OH)_{12}$	5.2	Yes *Observed as* $Ca_3(Al_xFe_{1-x})_2(SiO_4)_y(OH)_{4(3-y)}$
Calcite	$CaCO_3$	0.79	Yes
Ettringite	$Ca_6Al_2(SO_4)_3(OH)_{12}:26H_2O$	10.3	Yes
Hydrotalcite	$Mg_4Al_2(OH)_{14}:3H_2O$	4.55	No
CSH1.6	$Ca_{1.6}SiO_{3.6}:2.58H_2O$	37.2	Yes
Portlandite	$Ca(OH)_2$	17.6	Yes
C_2S(unreacted)	$(CaO)_2SiO_2$	2.14	Yes
C3S (unreacted)	$(CaO)_3SiO_2$	0.05	Yes
C4AF (unreacted)	$(CaO)_4(Al_2O_3)(Fe_2O_3)$	0.32	Yes
Water (free)	H_2O	19.8	

Table 5. Modelled volume fractions of cement hydration products after 20 days of hydration in Experiment 4; the name and chemical formula of the phases in this table are from the Thermochimie database. (SCK CEN model)

In *Table 5* the volume fraction of free water is assumed to be the porosity in the cement, i.e., we consider only fully saturated cement. Dissolution of cement hydration products and precipitation of secondary phases may alter the volume fraction of the free water in the cement and thus change the porosity. Practically the porosity change can also be related to the diffusion coefficient change through an Archie's law type relationship shown in section 3.3.2.3 (equation 3.3). However, such a handling of porosity and diffusion coefficient relationship may result in some grid-size-dependent numerical issues in the case of mineral dissolution and precipitation reactions. Therefore diffusion coefficients are assumed to be constant even though the calculated volume fraction of pore space may evolve with time.

The calculated porosity (19.8 %) reproduces reasonably well the measured porosity in the bulk of the cement paste (21.3 ± 2.4 % for SON68 and 25.9 ± 0.3 % for SM539, see Table 5-11 in D2.12).

All phases present in the model were experimentally observed, except for hydrotalcite, which is generally absent in CEM I HCP without Mg-carbonate additions.

Comparison with the solid analyses (D2.12) shows that the measured carbonation in the actual cement paste (measured volume fraction of 2 to 4.4 x 10^{-2}) was higher than calculated. This is the case also for the unreacted clinker (measured volume fraction 5 x 10^{-2} to 1 x 10^{-1}).

The experiment also showed that hydration was less advanced than predicted by the model. After 20 days of hydration there are thus still small amounts of unreacted clinker. For simplicity the remaining clinker is assumed to not react further after 20 days. All C3A is supposed to be completely hydrated.

Conclusions for cement hydration modelling (Initial conditions for modelling):

- Apart from Mg bearing phases, minerals included in the model are confirmed by the solid analyses.
- Carbonation of the cement in the mockup tests was underestimated
- The amount of unreacted clinker in the mockup tests was underestimated
- The model overestimates Al and underestimates the Ca concentration
- The porosity of the bulk HCP was reasonably well reproduced

3.3.2.2 Modelling of the glass dissolution

The fitted diffusion coefficients through the glasses are the averaged boron diffusion coefficients, assuming that all the glass particles contribute equally to the elemental solution concentrations in the glass layer. However, post-experimental analyses showed that glass particles closer to the filter (and thus to the cement) altered more than those away from the filter, especially for SM539 (See D2.10 and D2.12).

The glass alteration model does not describe the difference in alteration of the glass particles depending on their location. It is used rather as a high-level source term model that describes the total release of glass components to the cement component. The mechanism behind the diverging alteration of the glass particles is not well understood. The porosity in the glass compartment was 48 to 60%, so diffusion in the glass compartment must be fast, compared to the diffusion in the glass. Hence diffusion in the water surrounding the glass particles is not considered. There were no indications for cementation of the glass particles by precipitation of secondary phases.

The higher alteration of the glass particles close to the filter must be due to a more intense reaction with the cement, but this effect is more obvious for SM539 than for SON68. Possibly the high Si concentration in the SON68 compartment diffusing through the filter immobilizes the Ca on the cement side of the filter, preventing influx of Ca from the cement in the glass compartment, whereas for SM539 (with much lower Si concentrations in the glass compartment), Ca can still enter the glass compartment, but it reacts immediately with the first glass particles and has no time to diffuse to the bulk particles. This is however a speculative explanation. It also does not explain why the glass alteration in the bulk is so low (10 to 100 times lower than the forward rate), in spite of the high pH. In agreement with the glass alteration model used here, we can assume that a thin layer is formed that acts as a diffusion barrier. If this alteration layer has a different composition from the layer formed on glass particles close to the filter, it may also have different diffusion properties. The glass dissolution model that is used here, describes the behaviour of a hypothetical average glass particle. However, as long as the model correctly

describes the solution concentration of boron in the glass compartment, the results from the reactive transport modelling in the cement will not change.

Attempts were made to reproduce the measured concentrations in the glass compartment assuming equilibrium with secondary phases from the database. Equilibrium with these phases was assumed to calculate the release of glass components to the cement compartment.

- For SON68, CSH1.2 and K-phillipsite ($KAlSi_3O_8$:$3H_2O$) are oversaturated and may control the Ca and Al concentrations. The calculated Si concentration (about 1400 $mg \cdot L^{-1}$) is much lower the measured concentration, which increases continuously to < 4000 mg/L. Such high concentrations are possible because the glass compartment contains glass at high SA/V, while the transport between the glass and cement compartment is slow in the experimental setup. Hence the solution composition in the glass compartment is dominated by the dissolved glass components like in a system at high pH without solid cement phases (portlandite). In these conditions, very high Si concentrations are measured (Gin 2019), but they were not reproduced by the model.
- For SM539 strätlingite (a C-A-S-H phase) and K-phillipsite are oversaturated. The strätlingite would form because of the high Al content of SM539. This phase slightly overestimates the Al concentration: it predicts an Al concentration of about 5 mM (135 $mg \cdot L^{-1}$) whereas about 80 mg/L was measured.

3.3.2.3 Effect of the iron filter on diffusion

Effective diffusion coefficients in glass are generally in the order of $1x10^{-19}$ to $1x10^{-23}$ $m^2 \cdot s^{-1}$ and diffusion coefficients in cement are < $1x10^{-12}$ $m^2 \cdot s^{-1}$. Applying an aqueous diffusion coefficient of $2x10^{-9}$ $m^2 \cdot s^{-1}$ and a porosity of the iron filter of 0.34, the calculated effective diffusion coefficient in this iron filter based on Eq.3.3 is $2.3x10^{-10}$ $m^2 \cdot s^{-1}$ which is much higher than diffusion coefficients in the glass and cement. Therefore the iron filter is not expected to be a diffusion barrier. *Figure 37* shows that the iron filter has nearly no 'resistance' for boron (B) diffusion from the glass into the cement when the porosity of the iron filter is above 0.25.

The solid analyses in report and EURAD-ACED deliverables D2.10 (Gin 2019), D2.12 (Gin 2022) and in (Ferrand 2018) show that precipitates are formed inside the filter and at the interface with the cement paste, especially for SM539, but overall the initial porosity apparently does not decrease much. So the conclusion from the modelling that the filter does not constitute an important diffusion barrier seems to fit with the observations.

Comparison with similar mockup tests without filter (Ferrand 2018) gave indications that the total boron release was higher in these tests without filter than in the tests with filter, but the effect was significant only for SM539. This might be caused by the formation of a local precipitate at the interface with the cement, decreasing the porosity of the outermost part of the filter.

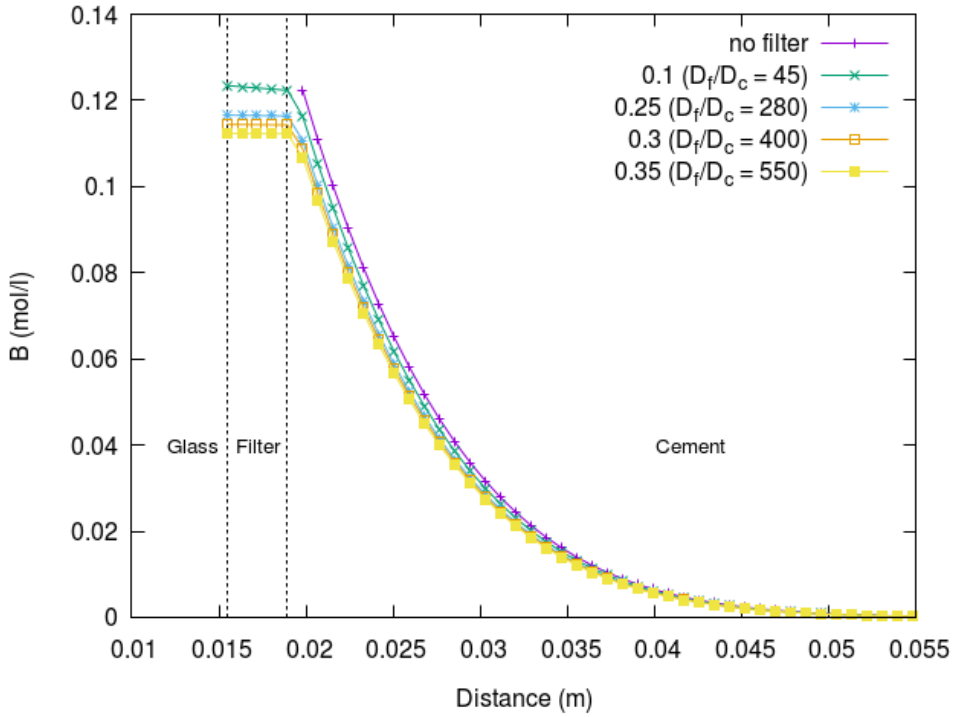

Figure 37. Effect of porosity in the iron filter on B diffusion from the glass into the cement for Experiment 4 (D_f is the calculated diffusion coefficient at different porosity in the iron filter based on Eq. 3.3 and a cement diffusion coefficient D_c of $4.5x10^{-13}$ $m^2 \cdot s^{-1}$) (SCK CEN model).

3.3.2.4 Modelling of the pH

At the end of the experiments, the measured pH in the glass compartment and the cement compartment was still higher than 13.3 for the experiments with both glasses. Such a high pH also limits the diffusion of Ca from the cement into the glass compartment since the Ca solubility is lower at higher pH. So, although glass powder was used in the experimental setup to increase the reactive surface area, the release of glass constituents that have the potential to decrease the pH was still too small to have a measurable effect within the geometry and duration of the experiment, and this is confirmed by the model (*Figure 38*). Also, the diffusion of the glass constituents in the HPC was too slow to have an effect on the pH in the cement. The nearly constant pH away from the glass compartment is also partially due to the no-flux boundary at the end of the cement plugs, so the Na and K controlling the pH of the cement cannot diffuse away. Otherwise, there would be a decrease in pH towards the end of the cement plug.

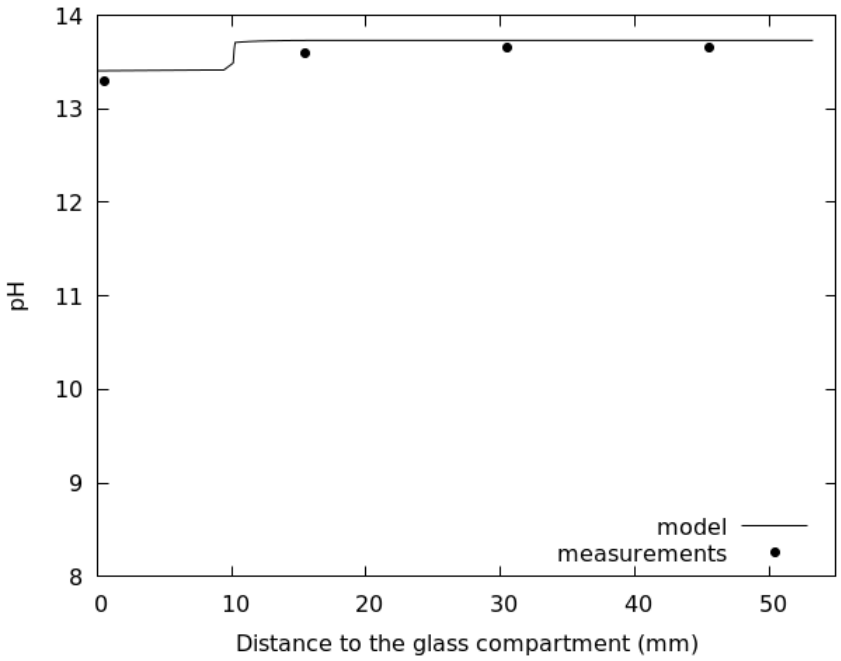

Figure 38. Modelled and measured pH profiles after 900 days for Experiment 4 with SON68 at room temperature (25°C); the results for SM539 are similar (SCK CEN model).

3.3.2.5 Modelling of the mineral volume fraction profile after 900 days

The main observations in the solid analyses were the following:

1. The SEM analyses shown in EURAD-ACED deliverable D2.12 (Gin 2022) show a morphologically altered layer at the HCP surface that is about 100 µm thick for SM539 and over 200 µm for SON68. This was observed also in previous analyses (Ferrand 2018). Nevertheless, it is not certain that we can generalize this, because the alteration layer thickness is not uniform. This layer shows an increased porosity. The increased porosity is the result of the dissolution of portlandite and reprecipitation as C-S-H phases, mainly CSH1.2. There is a Ca/(Si+Al) gradient from the glass towards the HCP: The Ca/(Si+Al) ratio is very low (<0.05) in the filter pores close to the glass, and higher in the filter pores and the phases in the gap on the HCP side. In the degraded cement, the Ca/(Si+Al) ratio is about 1.2. In the SM539 cell, this CSH1.2 phase almost completely cloggs the porosity. In the SON68 cell, there is more coarse porosity that was not clogged. The total volume fraction of CSH1.2 might thus be quite similar in the 2 cells but the distribution of this phase is different in the 2 cells. This looks unexpected, because SON68 releases much more Si to the HCP compartment, but the analyses also show presence of a layer of secondary alteration phases (S.A.P. layer) on top of the (altered) HCP. These would be ASR-gel like phases for SON68 and a mixture of calcium-alumina-silica hydrate phases (C-A-S-H) with amorphous SiO_2 for SM539. This layer is thicker for SON68 than for SM539. Part of the Si released by the SON68 is thus trapped in the ASR gel. The combined CSH1.2 and ASR gel formation is still higher for SON68 than for SM539. The soluble glass components like boron an the alkaline ions diffuse much deeper than the layer of 100 or 200 µm in which the Si reacts.
2. Next to SEM analyses, also LA-ICP-MS analyses are reported in D2.12. LA-ICP-MS profiles for Si and Ca are also shown in *Figure 42* in section 3.3.2.6. They show an alteration layer

containing less Ca and more Si than the bulk HCP, but only for SON68. This confirms qualitatively the SEM observation that the SON68 shows a more pronounced alteration layer. The LA-ICP-MS profiles suggest, however, a thinner alteration layer than the SEM analyses (for SM539 it even shows no alteration layer looking at the Si and Ca profile). Because we did not calculate chemical profiles from SEM-EDX mean measurements, the information obtained by these two techniques can, however, not be quantitatively compared. The different SEM and LA-ICP-MS profiles are not necessarily in contradiction with each other. If we see less increase of Si in LA-ICP-MS profiles, this does not necessarily mean that there is no Si coming from the glass compartment. The thin Si and Ca profile suggesting little in- or outflow of Si and Ca deeper than 100 µm could be the net result of a potentially important influx of Si coming from the glass and an equally important influx of Ca coming from the cement but precipitated as calcite. Because both Si and Ca increase, the concentration in ppm (and the profile) does not change. The precipitation of calcite could thus compensate the decreasing Ca/Si ratio and mask the influx of Si.

The solid analyses in D2.12 further give no indication for pore clogging in the altered HCP. There are some porosity changes due to dissolution and precipitation processes (pozzolanic reaction, carbonation), leading to a change in the capillary vs gel porosity ratio, but the overall porosity may not change that much.

3. The solid analyses further suggest depletion of ettringite, although small amounts of sulphur containing phases like ettringite and monosulfoaluminate remain at the surface.

We can compare these observations with the results of the modelling.

The modelled mineralogical profiles after 900 days are shown in *Figure 39*. At the interface, portlandite and CSH1.6 are replaced mainly by C-S-H with a lower Ca/Si ratio (CSH1.2), due to reactions with Si from the glasses. The model also predicts ettringite dissolution at the interface. For the Al-rich glass SM539, the model predicts strätlingite (C-A-S-H) precipitation due to the further reaction of CSH1.2 with Al from the glass. Strätlingite is a proxy for the observed C-A-S-H phases. Actual strätlingite precipitation was not observed in the experiments, probably due to the low temperature. Instead, Al substitution occurred in all the newly formed C-S-H at the interface, indicating further reaction of Al with C-S-H. These modelling results reproduce well the observations.

There are also observations the model cannot explain.
The model predicts a thickness of the altered cement layer less than 150 µm for both glasses. It could not reproduce the difference in alteration layer thickness. It also did not reproduce the formation of the ASR-gel like SAP layer on the SON68.

Prior modelling using tobermorite and jennite as precipitating phases could better reproduce the observed alteration layer thickness, including the thicker layer for SON68, but those phases are not representative of C-S-H in the Thermochimie version 11a database according to the authors of Thermochimie (Blanc 2012). CSH0.8, CSH1.2 and CSH1.6 are the three phases representing C-S-H in this database. Also, with tobermorite and jennite, the modelled volume fractions of hydration products are different from literature and from the measurement (D2.12). As mentioned higher, the alteration layer thickness is not uniform. Hence the relevance of the better fit with tobermorite and jennite must be relativized.

The formation of the ASR gel precipitation layer was not considered in the modelling exercise because these phases are not included in the database, but the high alkali content of the surface layer is considered in the modelling of Li, Na and K (section 3.3.2.8). In the model, CSH1.2 represents both newly formed C-S-H and ASR gel.

The evolution of the porosity is difficult to reproduce by the modelling. The observations suggest an increase of the porosity. However, in *Figure 39*, precipitation of CSH1.2 at the interface significantly reduces the capillary porosity for both glasses. This is indicated by a decrease in the volume fraction of white space. This porosity decrease in the HCP suggested by the model was thus not observed in the analyses. The precipitated SAP layer had a lower porosity according to the observations, but as mentioned this layer was not reproduced by the model. The apparent decrease of the porosity at the interface in *Figure 39* may be misleading though. C-S-H gels contain a significant amount of very small pores called gel pores (Jennings 2008), and the total porosity of cement includes capillary porosity and gel porosity (Jennings 2004). Therefore, precipitation of CSH1.2 at the interface does not completely occlude the cement and the actual porosity may be larger than suggested by *Figure 39*. Porosity clogging is difficult to describe as a homogeneous process in the heterogeneous HCP system.

Another aspect that was not fully considered in the model, was the carbonation that was higher than expected. Not considering this might have affected the (calculated) dissolution processes and may also be a cause for not reproducing the observed alteration thicknesses.

In the model, the higher Si release from the SON68 compartment leads to a higher CSH1.2 fraction in the first cement alteration layer. The Si could not diffuse deeper because it is retained in this phase.

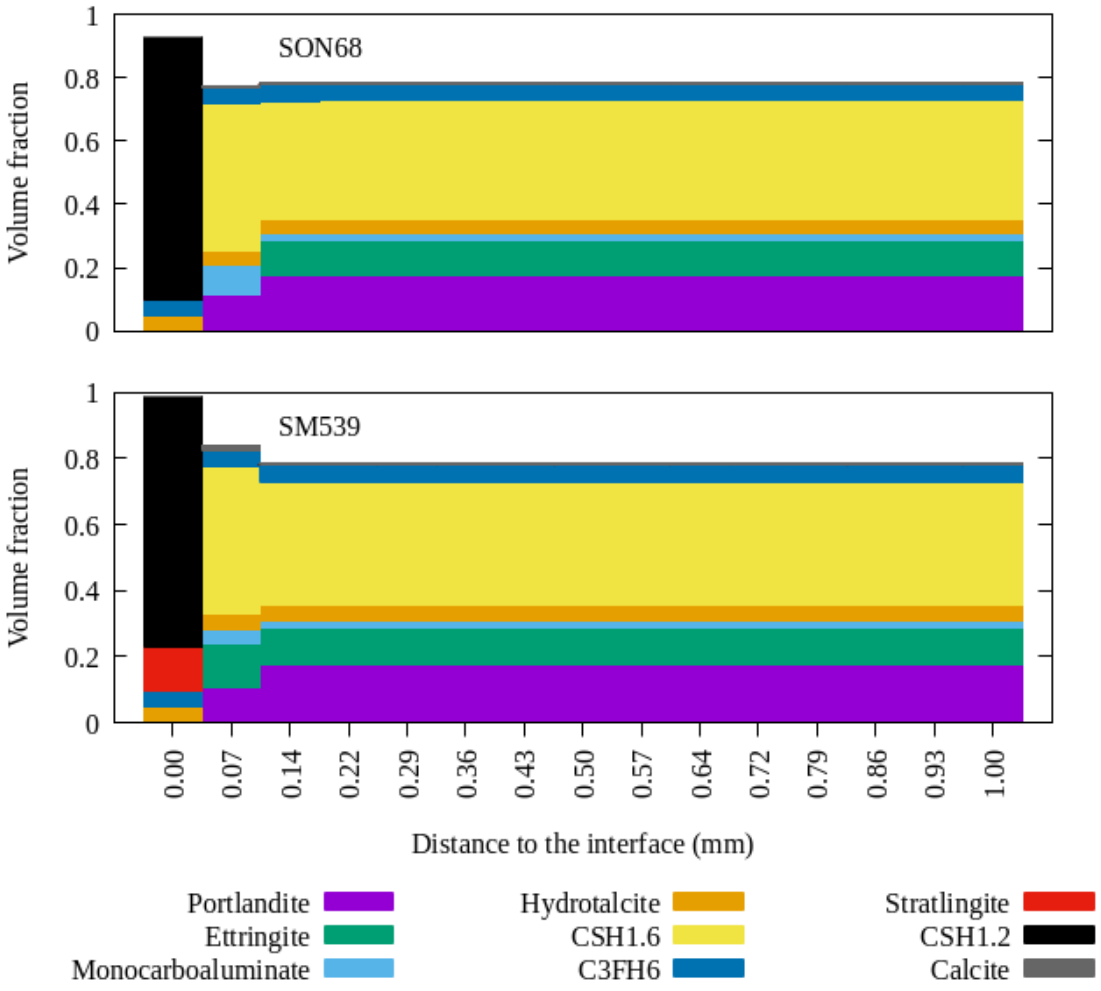

Figure 39. Modelled volume fraction of solid phases in the cement after 900 days in Experiment 4 at 25°C (SCK CEN model).

Conclusions for the modelling of the mineralogical profiles in the cement:

- The formation of a porous interface is reproduced, but there are uncertainties related to the representation of the secondary phases by the phases in the database; this also has an impact on the depth of the alteration profile.
- The partial filling of the porosity by C-S-H is reproduced.
- The predicted phases are similar to the phases observed and described in D2.12.
- The depth of the Si diffusion could be simulated reasonably well using a D_{cement} based on boron, but depends more on the assumed solubility controlling minerals than on the diffusion coefficient.
- The exact porosity is difficult to define, because of the difference between open porosity and gel porosity. Because of the gel porosity, a complete blocking of the further diffusion is unlikely
- The thin S.A.P. layer (≈ ASR gel or C-A-S-H + $SiO_{2(am)}$) that is observed and mentioned in D2.12 is not predicted by the model. Because the observed S.A.P were not included in the model, the model calculates more precipitation of CSH1.2 compared to the experimental results.
- Carbonation of the interface was not considered, but might have affected the dissolution processes.

Remark

Table 7 shows that the diffusion coefficient in cement was very low and similar for the two glasses**.** This is the case in spite of the important differences in the alteration layers. In both cells, the SAP edging phase can be considered as a dense crust that could act as a diffusion barrier. The thickness of this layer is much smaller in the SM539 cell but its nature is different. With all these porous network differences it is difficult to conclude that the similarly low diffusion coefficient of boron for both cells is linked to the change of the porous network in the altered area. There is no straightforward relation of the diffusivity with the evolution of the this porous network. Even if the porosity would increase, the replacement of the capillary porosity by gel porosity might still lower the diffusivity, if the pores are not connected. On the other hand, the low diffusion coefficient may also be caused by the nature of the diffusing boron species (see section 3.3.2.9). With the current information, it is not possible to exclude one of the two possible explanations.

3.3.2.6 Modelling of boron in the glass compartment and cement

The elemental profiles in the cement compartment were measured by LA-ICP-MS. A detailed description of the results can be found in EURAD-ACED deliverable 2.12 (Gin 2022). *Table 6* shows the calculated (theoretical) concentrations of elements in the cement close to the interface in the hypothesis that these elements would be present only as dissolved species in the cement pores (line 'Calculated'). The calculation of these concentrations is based on the measured concentrations in the glass compartment at the end of the experiments, i.e., after 900 days. Those concentrations are also the maximum concentrations expected in the pore solution of the cement at the interface according to Fick's first law of diffusion. Since the porosity and density of the cement are known, the concentrations can be calculated in µg/g cement. These calculated concentrations are compared with the concentrations measured by LA-ICP-MS for the SON68 cell (line 'Measured'). The measured concentrations include both the amounts in the pores (dissolved) and the amounts that are present in the cement paste in not-dissolved form. For all listed elements the calculated concentrations are much lower than the measured concentrations. These results indicate that all those elements are present predominantly in not-dissolved form, by precipitation or sorption on the cement phases. Calculation based on their pore solution concentration only would underestimate the amount of those elements in the cement.

Amount (µg/g cement)	B	Li	Cs	K	Mo	Na
Calculated (only dissolved species)	314.8	49.66	32.6	2430	95	1165
Measured (dissolved + not dissolved)	3428	1536	1959	94826	438	23305

Table 6. Comparison of calculated elemental concentrations in the cement close to the interface considering only dissolved species and concentrations measured by LA-ICP-MS including dissolved and not-dissolved species for Experiment 4 with SON68 at room temperature (≈ 25°C)

Boron has been reported to precipitate as calcium borate in a high-pH and calcium-rich solution (Utton 2013). Since thermodynamic data for calcium borate is not included in the current Thermochimie database, B sorption onto cement was assumed in the modelling with the sorption coefficient K_f as an additional fitting parameter. A linear sorption isotherm was assumed

$$B\_sor = K_f [B] \qquad \text{(Equation 3.9)}$$

Where B_sor is the amount of B sorbed onto cement and [B] is the boron concentration in the cement pore solution.

The criterion for the fitting was to ensure that the modelled boron concentration in the glass compartment and boron profile in the cement are in good agreement with the measurements. Since there are three fitting parameters, i.e., diffusion coefficients in the glass and cement and also the distribution coefficient of boron, such a modelling has to be done by trial and error.

With the parameters in *Table 7* the evolution of boron concentration in the glass compartment and boron profile in the cement can be modelled as shown in *Figure 40* and *Figure 41*.

Fitting parameter B	SON68	SM539
D_{B_cem} ($m^2 \cdot s^{-1}$)	7.1×10^{-15} ~ 2.1×10^{-14}	7.1×10^{-15} ~ 1.4×10^{-14}
D_glass ($m^2 \cdot s^{-1}$)	8.3×10^{-22}	1.2×10^{-21}
Kd ($mL \cdot g^{-1}$)	90~150	40~90

Table 7. Fitted parameters for B in the modelling of Experiment 4 at room temperature (SCK CEN model).

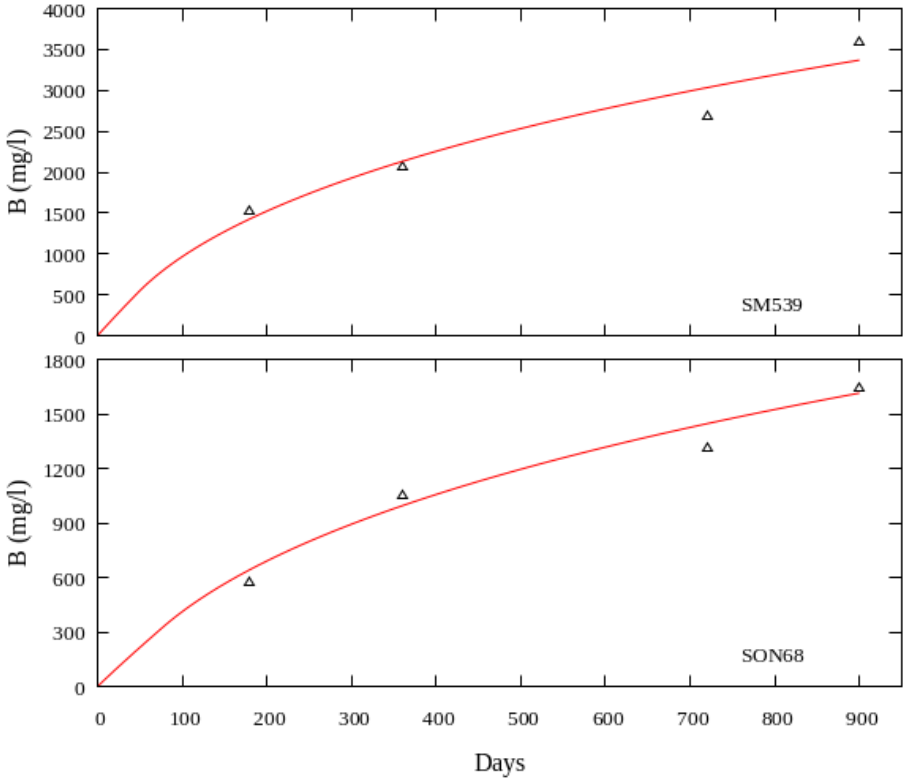

Figure 40. Measured and modelled evolution of B solution concentrations in the glass compartments for Experiment 4 at room temperature with glasses SM539 and SON68 (SCK CEN model).

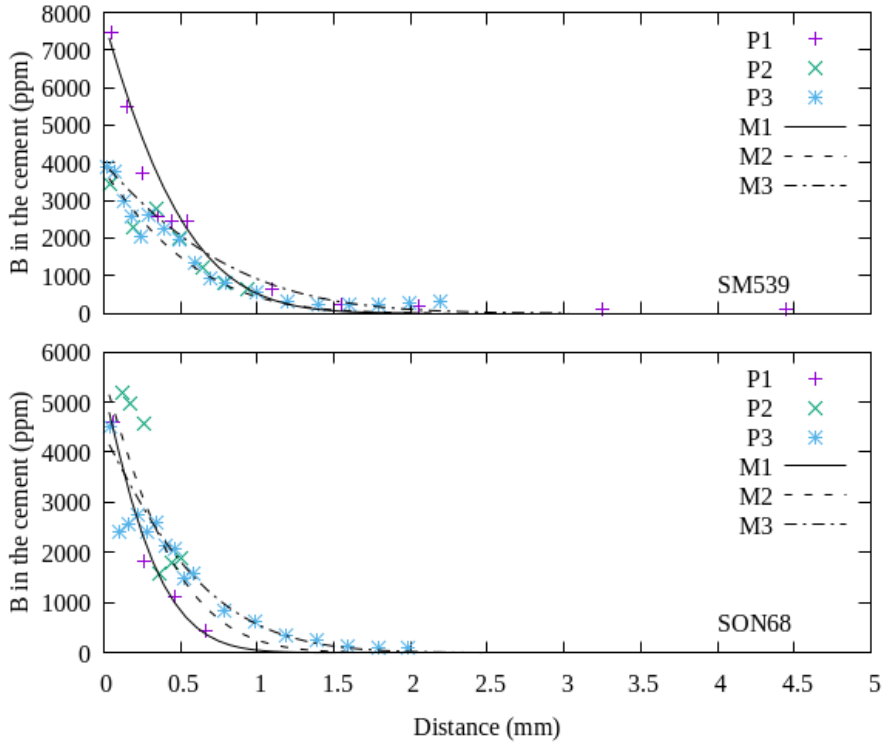

Figure 41. Modelled and measured LA-ICP-MS B profiles in the cement compartment after 900 days for Experiment 4 at room temperature for glasses SM539 and SON68; 3 profiles were taken and modelled separately (SCK CEN model).

3.3.2.7 Modelling results for Si, Ca and Al in the cement paste

Figure 42 shows the Si and Ca profiles in the cement as measured by LA-ICP-MS and the modelled Si and Ca profiles. The altered depths for Si and Ca from LA-ICP-MS are much smaller than for boron in *Figure 41*. The modelling results for Si are in good agreement with the LA-ICP-MS results, i.e., there is an increase of Si close to the interface. The enrichment of Si is due to Si diffusion from the glass into the cement. The silica concentrations in the glass compartment are indeed high (>4000 mg/L for SON68, around 300 mg/L for SM539). The model predicts a slight decrease of Ca at the interface, which is also in agreement with the Ca decrease at the interface measured by LA-ICP-MS. The Ca is assumed to diffuse towards the filter and the glass compartment, where it might precipitate (section 3.3.2.3). In the model, the Ca pore solution concentration in the cement is very low because it is controlled by equilibrium with portlandite :

$$Ca(OH)_2 \rightarrow Ca^{2+} + 2OH^- \qquad \text{(Equation 3.10)}$$

The high pH as in this experiment will thus suppress the dissolution of portlandite. Ca dissolution and local reprecipitation will not significantly change the total amount of Ca.

The measured profiles can be reproduced relatively well, although the Ca concentrations that were measured in the unaltered HCP were around 60 mg/L and thus much higher than the theoretical concentrations predicted by the model.

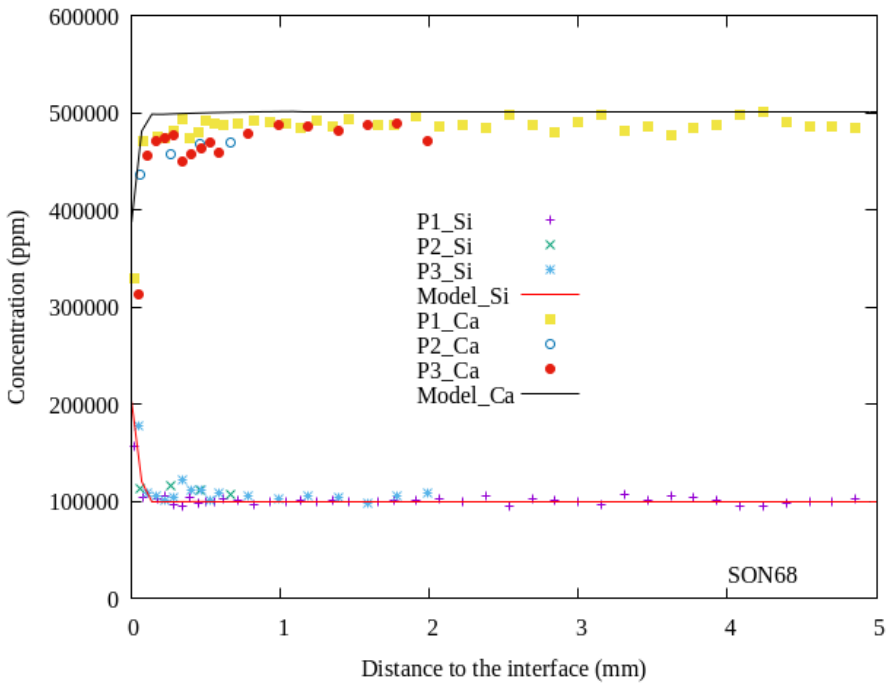

Figure 42. Comparison of the modelled and measured Ca and Si profiles in the cement compartment after 900 days for SON68 glass in Experiment 4 at room temperature (SCK CEN model).

For glass SM539, the modelling shows little Si enrichment in the cement and thus also very little Ca decrease at the interface due to the low Si concentrations in the glass compartment (data are not

shown). These modelling results agree with the LA-ICP-MS profiles that show no change of the Si or Ca concentration close to the filter (see D2.12).

The obtained modelling results agree well with the measurements for the Al profiles in the cement for the SM539 cell shown in *Figure 43*. The increase of Al near the interface is due to the fact that the Al concentration is higher in the glass compartment than in the cement, leading to diffusion of this Al into the cement. For the SON68 cell both the model and LA-ICP-MS results show little variation of the Al concentrations across the cement compartment (measured data shown in D2.12) because the Al concentrations are equally low in the glass layer and the HPC pore water, so there is nearly no Al diffusive flux. Note that even though the weight percentage of Al_2O_3 in SM539 glass (20%) is much higher than in the cement (3%), there is only a small amount of Al from the glass compartment reaching the surface of the cement due to the low Al solution concentration gradient between the glass layer and the cement. Thus the interaction of cement and glass in those experiments is controlled by diffusion in the pore water.

As mentioned in section 5.3.2.5, precipitation of calcite could mask the Ca dissolution. This case was not modelled.

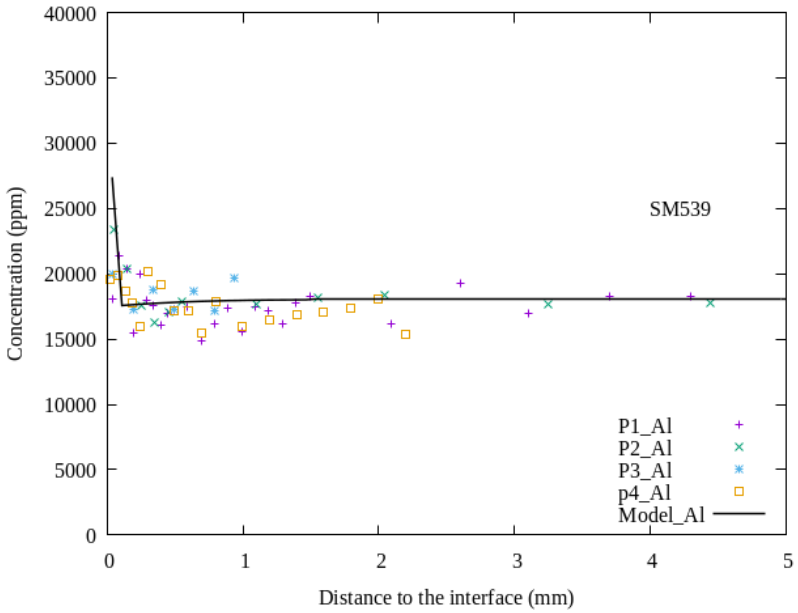

Figure 43. Comparison of the modelled and measured Al profile in the cement compartment after 900 days for glass SM539 of Experiment 4 at room temperature (SCK CEN model).

3.3.2.8 Modelling results for Li, Na and K in the hardened cement paste

Figure 44 shows the measured and modelled Li, Na and K profiles in the cement for the cell with SON68 after 900 days. The results for SM539 are similar and are not shown here. The measured Li, Na and K profiles deviate from typically diffusional profiles since it is more L-shaped. Without including alkali sorption the model underestimates the alkali concentrations at the interface, even though the model describes well the deeper profile of the alkali concentrations. Since Li has a larger penetration depth than B, the fitted effective diffusion coefficient for Li is also larger, as shown in *Table 8*. Such differences

between Li and B might be due to the relatively small size of Li (see section 3.3.2.9). To better describe Li at the interface sorption of Li onto the newly formed CSH1.2 at the interface was included:

$$Csh\_sOH + Li^{+} = Csh\_tOHLi^{+} \quad \text{(Equation 3.11)}$$

In this reaction the Csh_sOH is the surface master species associated with CSH1.2. Similar sorption reactions were also applied for Na and K in the model with the same reaction constant. Therefore the sorption sites are not only occupied by Li, but also Na and K. For simplicity, a very large reaction constant was applied so that all the available surface sites of CSH1.2 were covered by alkalis (Hong 1999). It was found that with a site density of 0.05 mol sites per mol of C-S-H such as used for CSH1.6 in the hydration model, the modelled Li, Na and K concentrations at the interface are much lower than the measured concentrations shown in *Figure 44*. The site densities required to better describe the Li concentrations at the interface for SON68 and SM539 are much higher, i.e., 0.37 instead of 0.14 mol sites per mol of newly-formed CSH1.2 shown in *Table 8*, respectively. The model requires a higher site density for the newly-formed CSH1.2 in the experiment with SON68 because the Li solution concentrations for SON68 are much lower than for SM539, but the Li concentrations measured by LA-ICP-MS at the interface for SON68 glass are as high as for SM539. Such difference is linked to the nature of the newly-formed phases, i.e., more ASR like gel in the SON68 cell and more C-A-S-H plus silica gel in the SM539 cell.

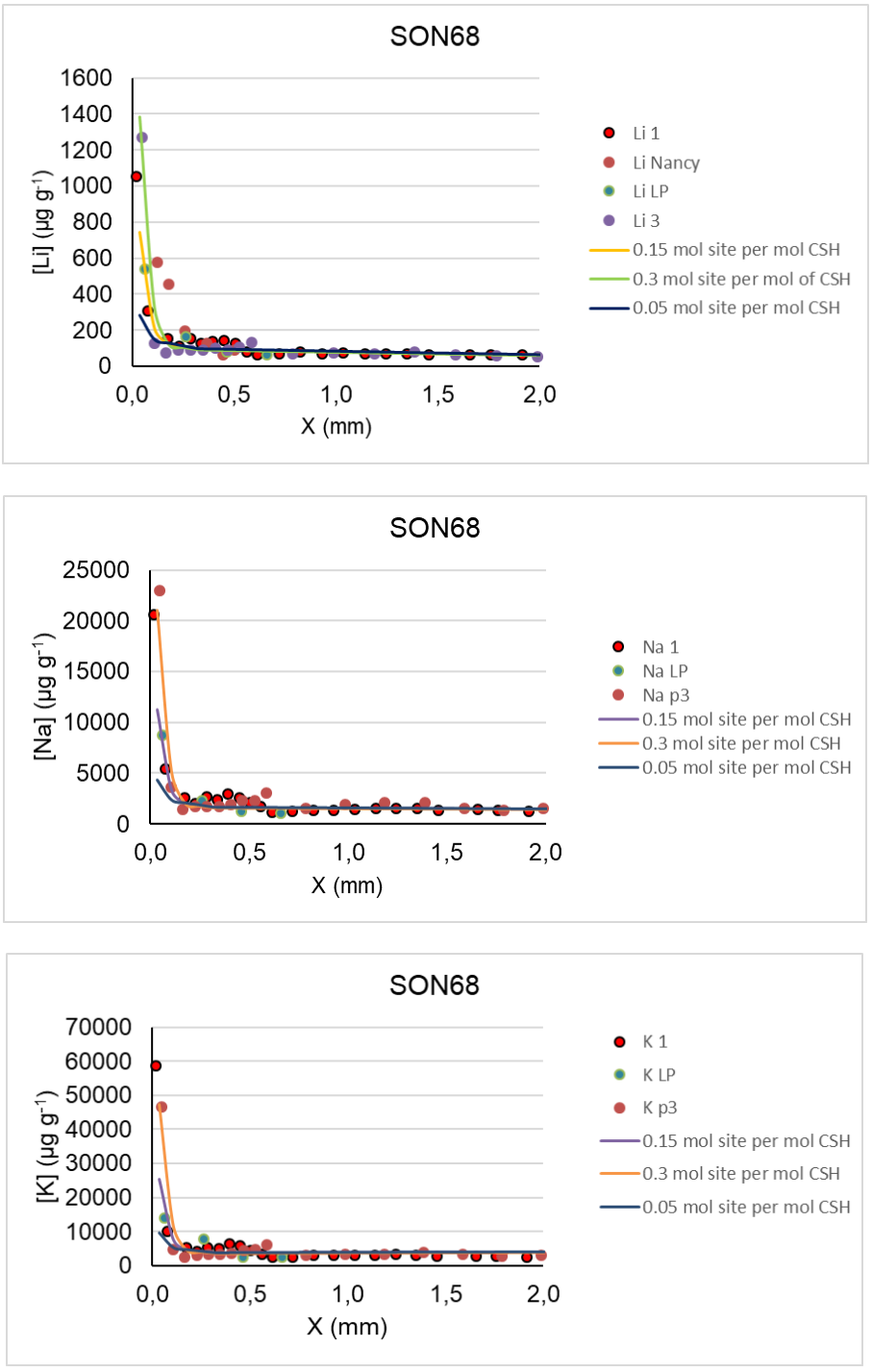

Figure 44. Comparison of the modelled and measured Li, Na and K profiles in the cement compartment after 900 days for the cell with SON68 glass in Experiment 4 at room temperature (SCK CEN model)

Fitting parameter Li	SON68	SM539
D_{Li_cem} ($m^2 \cdot s^{-1}$)	1.1~1.4 x10^{-13}	(0.7~1.1) x 10^{-13}
Site density (mol per mol CSH1.2)	0.37	0.14

Table 8. Fitting parameters for Li diffusion and sorption in the cement for Experiment 4 at room temperature (SCK CEN model).

3.3.2.9 Interpretation of the boron and lithium diffusion coefficient in the cement paste

Boron does not stabilize the GAL. Hence the concentration of leached boron has no direct effect on the glass dissolution. Still, it is important to understand its behaviour for several reasons. Boron is a glass dissolution indicator and high concentrations of boron species can decrease the local pH, and hence have an effect on the glass dissolution. But in the context of this experiment the main relevance is that D_{glass} and D_{cement} for boron are used also for the other glass constituents, like silicon and alumina. Hence the calculated depth of the diffusion profile of silica in the cement, is the depth assuming that the cement diffusion coefficient for borate and silicate species is the same.

The diffusion coefficients D_{cement} for boron (Table 7) are smaller than usually assumed. The diffusion coefficients of order of magnitude 10^{-14} $m^2 \cdot s^{-1}$ are 100 or 1000 times smaller than D_e for tritium in CEM I ($5.9x10^{-12}$ $m^2 \cdot s^{-1}$) given in (Večerník 2019). In section 3.4.3 of EURAD-ACED deliverable D2.17 (De Windt 2022) an effective diffusion coefficient of $1x10^{-11}$ $m^2 \cdot s^{-1}$ is used for a CEM I concrete with total porosity of 11.5%.

Using the much lower diffusion coefficients may have an important effect on the predicted long-term evolution. Hence it is important to understand why we find such low diffusion coefficients for boron (and lithium).

The diffusion of glass tracer elements (Li, B) was limited to the first millimeters of the HCP, and the diffusion coefficients of these elements are very low compared to HTO, Cl^- and Na^+, which are commonly used as 'non-reactive' diffusion tracers in cement (Bajja 2015, Večerník 2019). This behaviour is linked to (i) the aqueous chemistry of these elements in alkaline environments, (ii) the sorption and precipitation of these elements in HCP, (iii) the electrostatic interaction of these ions with cementitious hydrates, and (iv) the evolution of the porous network of HCP at the interface with the stainless steel filter. The sorption/precipitation phenomena are discussed in section 3.3.2.8 and can partly explain the sharp diffusion profiles. The other points are discussed in this section.

The aqueous boron chemistry is dominated by the constant dissociation of boric acid following the equation:

$$B(OH)_3 + H_2O \leftrightarrow B(OH)_4^- + H^+ \qquad LogK = -9.24 \ \ (T = 25°C, I = 0) \qquad \textit{Equation 3.12}$$

In highly alkaline media, the tetrahedral ion $B(OH)_4^-$ will be the dominant species, and in the absence of complexing counter ions, this anion will diffuse in the cement paste. This anionic species presents a high steric hindrance, which can at least partly explain the slow diffusion of boron in cementitious medium. Li can also diffuse in the form of an anionic species in alkaline environments, as it can complex with SO_4^{2-} to form $LiSO_4^-$ (Dhoury 2015):

$$Li^+ + SO_4^{2-} \leftrightarrow LiSO_4^- \ (aq) \qquad \textit{LogK = 0.77 (T = 25°C)} \qquad \textit{Equation 3.13}$$

The important release of SO_4^{2-} from ettringite dissolution at the interface with the stainless steel filter might have led to such complexation. Compared to Na and K, Li presents a smaller ionic radius but a higher hydration shell, which can also explain its slow diffusion through HCP. Note that a difference in diffusivity between these alkalis is linked to the size and charge density of these cations. Indeed, higher charge density induces stronger electrostatic interactions with the surface, and higher solvation shell radii induce lower retention. For instance, it was recently shown by atomistic simulation that Cs diffuses much more rapidly in C-S-H than Na, with a difference of two orders of magnitude in the effective diffusion coefficients (Duque-Redondo 2021). The same authors also showed that the aliovalent substitution of Si^{4+} by Al^{3+} in C-S-H strongly decreases the diffusion of alkalis. However, it is difficult to see any impact of this substitution on the Li diffusion profile obtained for the different cells, probably because substitution of Si by Al in C-A-S-H is limited to the direct interface.

Similar phenomena may cause the slow diffusion of silicate species, which are also present as relatively large anions.

Another or a complementary explanation for the low diffusion coefficient can be that the altered HCP, containing secondary phases such as CSH1.2 and calcite from the carbonation reaction has a lower accessible porosity than the unaltered HCP or that there is more sorption on the altered HCP, which may lead to a smaller effective diffusion coefficient even with an increased accessible porosity. In this regard, the formation of subsequent layers with a decreasing Ca/Si ratio towards the glass may have an effect on the diffusivity. Alkali silicate solutions, also known as water glass, are used as concrete densifiers in the building industry due to their pore-filling effects. They work by combining with free limes to form C-S-H, or ASR-like gel (Thompson 1997). The formation of such reaction products was also proved in the experiments. Hence the low effective diffusion coefficients may result from the high concentrations of Na, K and silicates in the glass compartments.

With the limited information available, it is not clear if the low diffusivity is due to the speciation of the boron (and silica) or to a change in the properties of the altered cement versus the unaltered cement.

3.3.3 Conclusions for the modelling of Experiment 4

- After 900 days only a very thin layer of cement has been chemically altered. Transport of all the elements from the glass investigated here seems to be retarded in the cement due to either sorption and/or precipitation as secondary phases. The diffusion length for B in the cement is about 2 mm, and the diffusion length for Si is less than 0.5 mm.
- 1 D reactive transport model plus diffusion-controlled glass dissolution model can well reproduce the B solution concentration in the glass compartment, and the LA-ICP-MS and mineralogical profiles in the cement, including sorption of alkali cations on newly formed C-S-H with low Ca/Si ratio
- The fitted B diffusion coefficient in the cement is in the order of 10^{-14} $m^2 \cdot s^{-1}$, this is 100 to 1000 times smaller than the values usually assumed for cement (effective diffusion coefficient for HTO). The model assumes the same D_e for diffusion of silicon species, but because this element is solubility controlled, the diffusion profiles are more shallow than for boron. The concentration profiles of Si do, however, not reliably indicate the diffusion profile because the concentration of Si in the HCP is already very high (contrary to boron). The only indication concerning the penetration depth of Si is the reaction of the anhydrous phase. In the altered area, the amount of silicic acid was sufficiently high to dissolve portlandite and favor hydration.
- It is not clear if the low diffusivity is due to the speciation of the diffusing species or to a change in the properties of the altered cement versus the unaltered cement.
- The model is applicable at high pH (≈13.5) and does not consider affinity effect; the only fitting parameters are the diffusion coefficients in glass and cement; effects of glass composition and cement properties are expressed via the diffusion coefficients.
- The penetration depths in the cement for different elements from the glass are different, indicative of complex interaction between elements from the glass and cement.
- The formation of a porous layer depleted in portlandite is well reproduced, but the exact porosity is not clear (gel porosity vs. open porosity; porosity is intrinsic parameter in D_{cement})
- The faster dissolution of the glass particles at interface with cement was not modelled separately
- The effect of the interaction with steel and a possible dense corrosion product layer was not studied, as there is no measurable corrosion of the stainless steel filters at pH 13.5.

- Even though the pozzolanic reaction is expected to speed up the release of calcium from the cement, the results show that only calcium in the cement close to the glass has reacted after 900 days; this can be explained by the low calcium solubility in the cement at high pH.

4 Model application on waste package scale

4.1 Generic system for modelling at waste package scale

The calculations have been done for the reference disposal cell systems described in section 2.1.1 (HLW glass/steel/bentonite/granite) and section 2.1.2 (HLW glass/steel cement/clay). These systems are also the base case for the modelling in task 4.1 described in EURAD-ACED deliverable 2.17 (De Windt 2022). Some characteristics, such as the thickness of the buffer and the properties of the host rock may be not relevant for modelling at the mm or cm waste package scale. Within these reference systems, there are still differences between the various national concepts, more particularly different materials for the engineered barriers and host rock, and different dimensions. The definition of the materials in the system has important consequences, because the parameter estimations from experiments simulating another system may not be usable.

4.2 Description of models used for modelling at waste package scale

4.2.1 Model used by BRGM for the HLW glass/steel/bentonite/granite system at waste package scale

Initially the plan was to model the glass/steel/bentonite/granite system. Due to unforeseen circumstances this was not possible. Instead, a similar system, i.e. glass/steel/COx claystone has been modelled (section 4.3.1). Because at waste package scale and for the considered time frame, the influence of the host rock (granite) on the glass and steel alteration can be neglected, and because the effects of clays like bentonite and COx clay are qualitatively similar, this system is comparable to the glass/steel/bentonite/granite system. The model that was used was the one presented in section 3.1, with the geometry explained in section 4.2.2. The parameters and modelling results are given in section 4.3.1.

4.2.2 Model used by BRGM for the HLW glass/steel/cement/clay system at waste package scale

The selected modelling tools and modelling strategy were similar to those described in section 3.1. The interactions at the waste package scale were simulated using a 1D radial geometry (*Figure 45*) with a spatial discretization of 5 mm at the interfaces, whereas for the modelling of the experiment (section 3.1) a grid size of 1 µm was used.

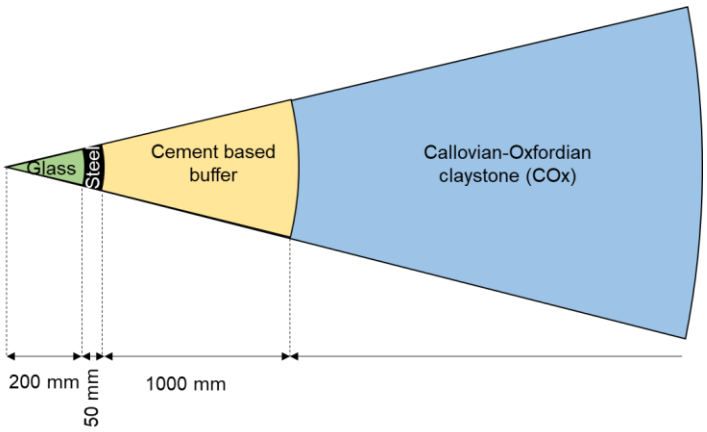

Figure 45. Considered radial geometries for the modelling at the waste package scale (BRGM model).

Several simulations were carried out in order to ensure the continuity between the approach considered for the simulation of the experiments and the generic case. The geometry was first used without cementitious material using the parameters previously considered for the modelling of experiments (i.e. temperature of 70°C, constant corrosion of 2 µm $year^{-1}$ etc.). The objective was to check the possible impact of upscaling on the numerical results. Thereafter, a young concrete (i.e. pH = 13.5) was implemented at 25°C to simulate the base case defined in Task 4 (Table 3.1 in D2.17). The modelled cases, the parameters and modelling results are shown in section 4.3.2.

4.2.3 Model used by SCK CEN for the HLW glass/steel/cement/clay system at waste package scale

The diffusion driven high pH model was not used at waste package scale, but a calculation was performed in which the model simulating experiment 4 was allowed to run for several days to see how much glass must dissolve for the glass compartment to decrease the pH at the glass surface from 13.6 to pH 10 - 10.5, where the conventional affinity driven dissolution models are applicable. The model used for the cement/clay system is the same as the model described in section 3.3

4.3 Modelling cases and results at waste package scale

The calculations at the waste package level in task 3.2 are complementary to those in task 4 and described in EURAD-ACED deliverable D2.17 (De Windt 2022), and allow conclusions for task 4. These are sensitivity studies to see the effect of parameter variations for a particular model. The models used in task 4 are explained in report deliverable D2.17.

The reference systems are the ones described in section 2.1. The parameters were varied for the modelling of task 3.2, to do more detailed calculations at the mm or cm scale around the glass/steel/concrete or glass/steel/bentonite interface (but the bentonite was replaced by COx clay). Different cases were modelled varying the glass composition (ISG and SON68), the thickness of the steel layer, temperature, evolution stage of the cement buffer, and the selection of iron corrosion products.

A major difference with the disposal cell scale calculations of Task 4.1 in D2.17 is that the latter calculations include explicitly the evolution of the near field and the overpack (phase II in *Figure 2*). The glass dissolution starts when most of the overpack has been corroded. In the calculations of Task 3.2, the glass dissolution and overpack corrosion start simultaneously, at least for the system HLW/steel/COx and the system HLW/steel/young concrete. For the system HLW/steel/aged concrete, the glass is assumed to start dissolving only when the concrete has aged already.

For the glass/steel/cement/COx system the calculation was done in Task 3.2 to simulate the evolution of the young cement (see section 4.3.2) simultaneously with the glass dissolution, but in this calculation only the concrete layer in direct contact with the COx clay was aged by conversion of portlandite into calcite. The concrete in contact with the glass was young concrete for the entire modelled period of time (up to 10,000 years). In the calculations for T4.1 in D2.17, all portlandite has disappeared at the time of the overpack perforation. So the conditions to which the glass is exposed in these modelling exercises are very different. It is also important to consider those results as a modelling test when the GRAAL model was applied beyond its range of pH applicability (6-10.5) as for example when the young concrete was modeled.

4.3.1 Modelling cases and results from for the HLW glass/steel/bentonite/granite system (BRGM)

As mentioned before, due to unforeseen circumstances the calculation for the HLW glass/steel/bentonite/granite system was replaced by a different, but comparable system. This was thus not identical to the reference HLW glass/steel/bentonite/granite disposal cell defined in D2.17.

The base case defined for the glass/steel/bentonite/granite system for the modelling in task 4.1 as defined in D2.17 is given in *Table 9*.

	Buffer thickness (cm)	**Temp (°C)**	**Water saturation (%)**	**Bentonite type**	**Steel overpack**	**Granite**	**Glass**
Base case in task 4.1 for Period III	75	32	100	Febex	5 cm thick Porous, with corrosion products	Spanish Reference Granitic host rock	ISG

Table 9. Base case defined for the glass/steel/bentonite/granite system in Table 2-1 of D2.17.

For Task 3.2, the modelling was done for the system described in *Table 10*. Apart from the clay type, also the glass and temperature were different. Because COx and Febex are both clays, having similar qualitative properties, the modelling of the glass/steel/COx clay is considered as an approximation for the reference case with Febex.

	Buffer thickness (cm)	**Temp (°C)**	**Water saturation (%)**	**Bentonite type**	**Steel overpack**	**Granite**	**Glass**
Base case task 3.2	75	70	100	COx clay 25 m	5 cm thick Porous	Not considered	SON68 (unfractured, homogeneous)

Table 10. Glass/steel/clay base case studied in Task 3.2 to replace the base case for Task 4.1 given in Table 2-1 of D2.17.

This 'glass/steel/COx clay' system at waste package scale was modelled as a first step for the glass/steel/young cement/COx clay system (section 4.3.2), using the model presented in section 3.1 and the geometry shown in section 4.2.2 (*Figure 45*).

In this modelled case, a waste package surrounded by the COx clay without cementitious material was simulated using conditions as close as possible to those of the EDF/ANDRA experiments (see section 3.1). Thus, SON68 glass, a constant temperature of 70°C, a constant steel corrosion rate of 2 µm year^{-1} and a layer-by-layer alteration of the glass were considered. The glass was considered impermeable (i.e. $D_e = 10^{-45}$ m^2·s^{-1} at 70 °C) until its alteration began, after which diffusion coefficients $D_e = 5.6\ 10^{-11}$ m^2·s^{-1} at 70 °C were used for diffusion in the pore water and $D_e = 1.8\ 10^{-22}$ m^2·s^{-1} at 70 °C for diffusion in the altered layer of the glass. Fractures were not considered. Similarly, a layer-by-layer corrosion of the steel was applied. Nevertheless, following the modelling scenario selected in the framework of Task 3.2, the steel was processed as a permeable medium ($D_e = 5.6\ 10^{-11}$ m^2·s^{-1} at 70°C). This strategy avoids H_2 accumulation at the glass – steel interface.

Overall, corrosion products predicted after 1,000 years of simulated time were consistent with the modelling of experiments (cf. section 3.1). For example, a reduction of pyrite in pyrrhotite was expected in the COx. As simulated for the experiments, a slight precipitation of saponite was also predicted. The main corrosion products were magnetite, iron carbonates (i.e. siderite and chukanovite) and berthierine at the steel – COx interface (*Figure 46*). As expected, the glass – steel interactions led to the formation of magnetite and iron silicate (i.e. cronstedtite-Th).

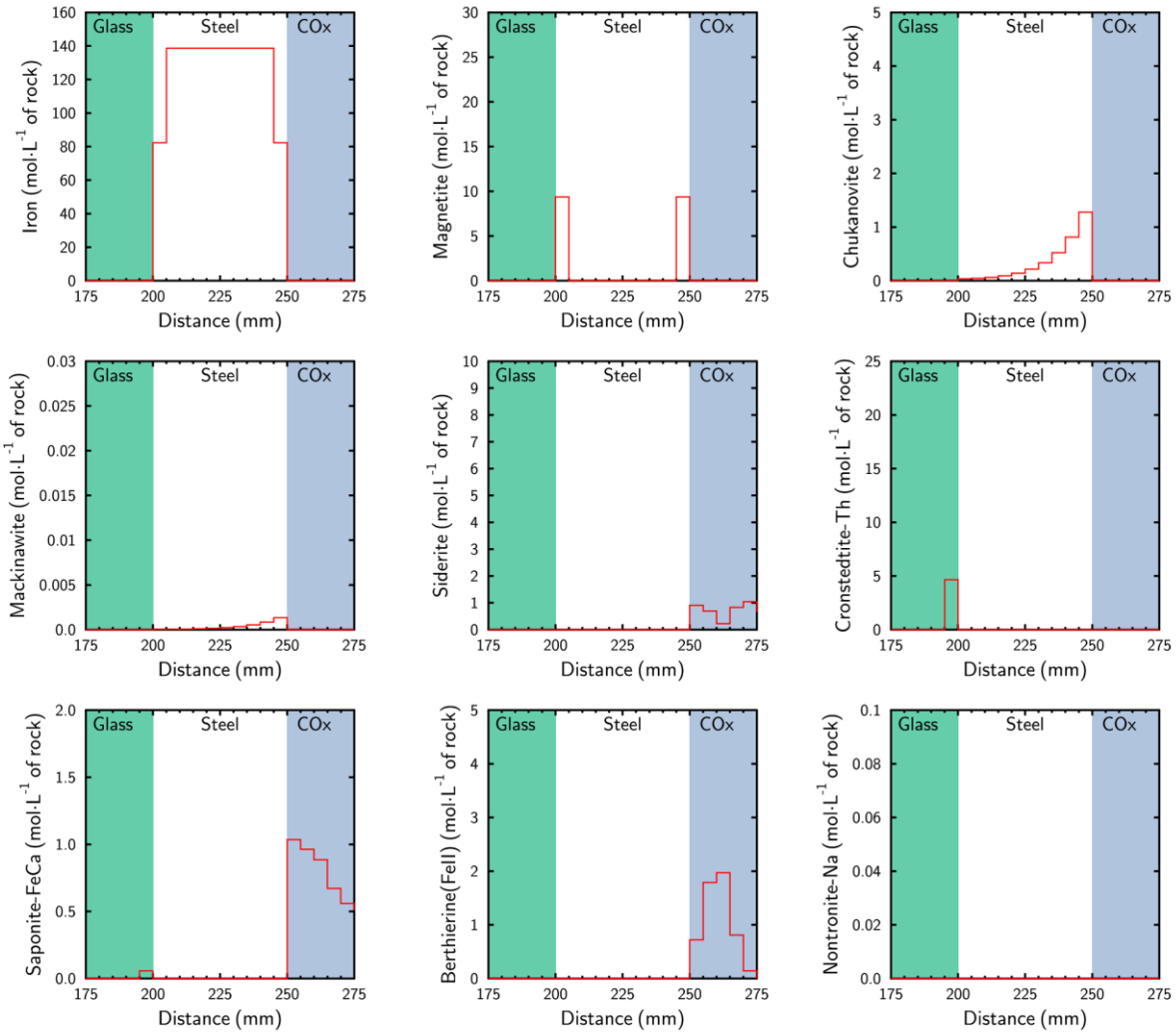

Figure 46. Corrosion products calculated with the BRGM model after 1,000 years. Modelling carried out at the waste package scale with SON68 glass but without cementitious material at 70°C.

Nevertheless, corrosion products were slightly different at 10,000 years with formation of cronstedtite-Th at the steel – COx interface (*Figure 47*). We would thus have a corrosion product layer composed of a mix of magnetite, chukanovite and Mackinawite. The iron-silicate precipitation may be related to the consideration of steel as a permeable medium (i.e. Si diffusion from the glass).

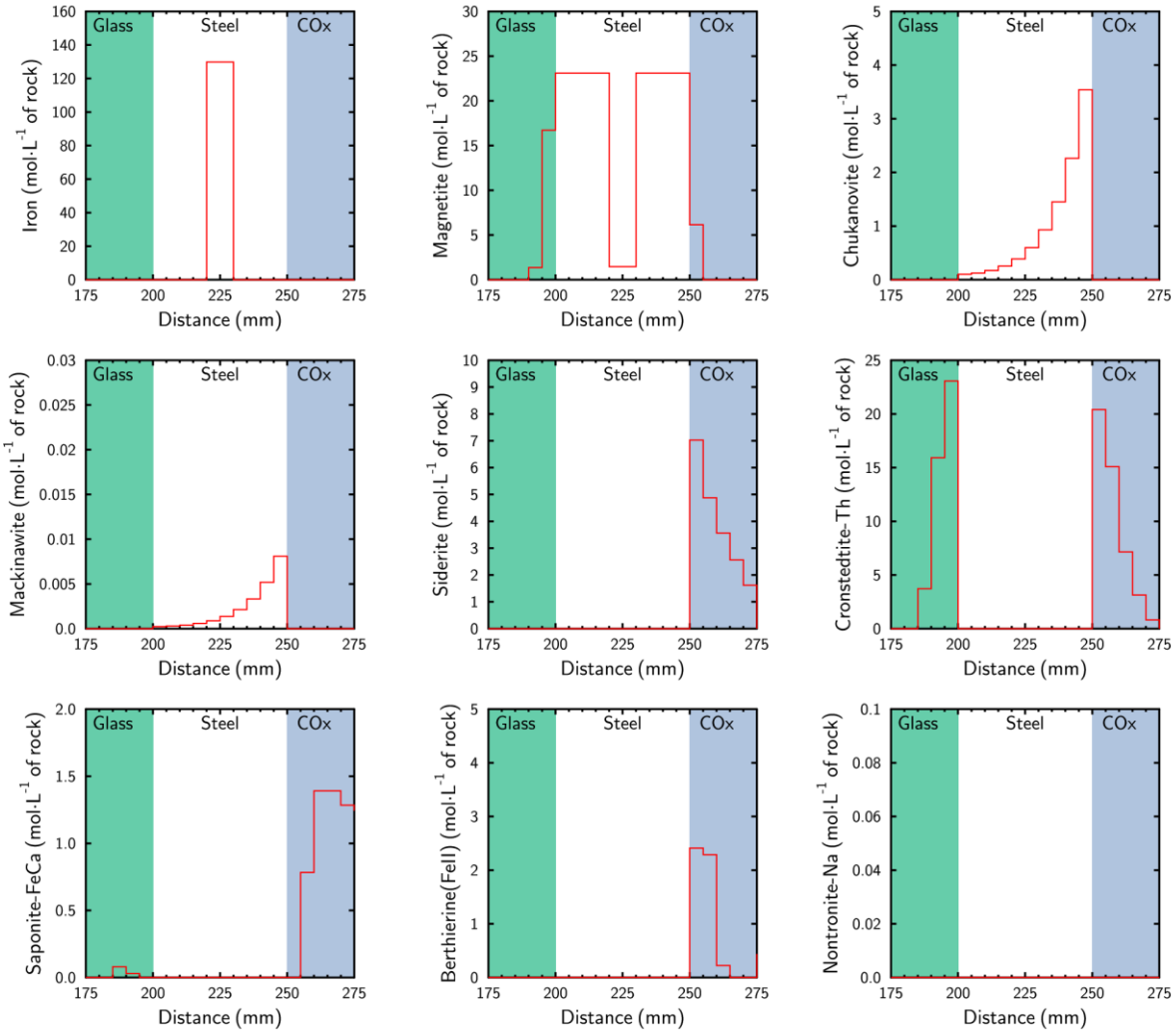

Figure 47. Corrosion products calculated with the BRGM model after 10,000 years. Modelling carried out at the waste scale with SON68 glass but without cementitious material at 70°C.

A thickness of 12.9 mm of glass was altered at 10,000 years (Figure 48). SON68 alteration products were consistent with the modelling of experiments; numerical results indicated the presence of non-passivating gels as well as the precipitation of zincsilite ($Zn_3Si_4O_{10}(OH)_2 \cdot 4H_2O$), pimelite ($Ni_3Si_4O_{10}(OH)_2 \bullet 4$), hydroxyapatite ($Ca_{10}(PO_4)_6(OH)_2$), $CaMoO_4$(s) and celestite ($SrSO_4$).

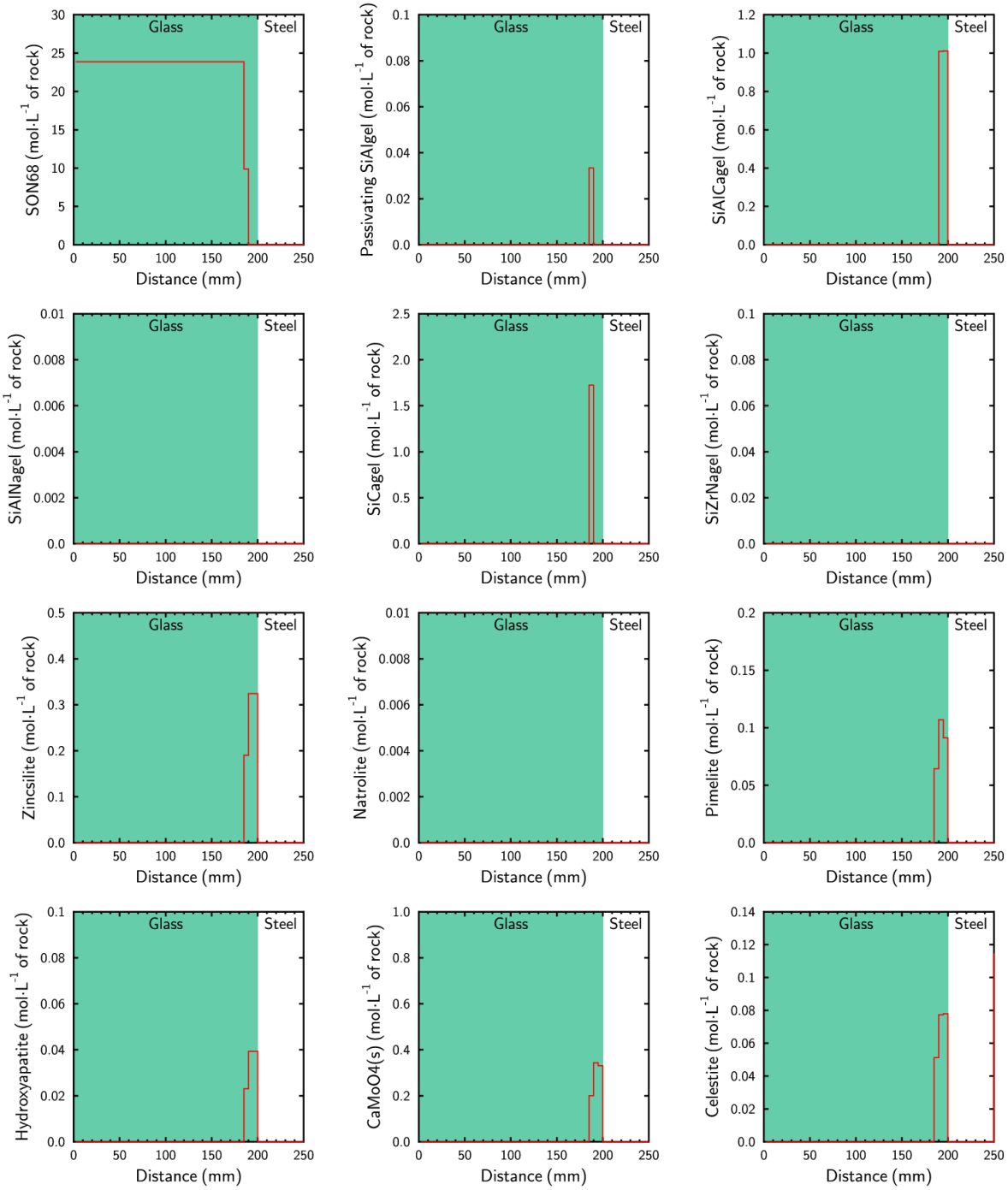

Figure 48. SON68 glass alteration products calculated with the BRGM model at the glass – steel interface after 10,000 years. Modelling carried out at the waste scale without cementitious material at 70°C.

The upscaling from the modelling of experiments to the generic case by increasing the grid size from 1 µm to 5 mm and the reaction progress had a negligible impact on the numerical results.

The types of steel corrosion products that are expected on the short term (in the experiment) and on the long term (waste package) are mostly similar. The long-term calculation predicts also the formation of cronstedtite in the COx contacting the steel, though, whereas this does not appear in the experiment modelling. Cronstedtite also does not appear in the disposal cell scale modelling in EURAD-ACED deliverable D2.17 (De Windt 2022).

4.3.2 Modelling cases and results for the HLW/steel/cement/clay system (BRGM)

A base case was defined for task 4.1, and complemented by a sensitivity analysis (see table 3.1 in D2.17). The base case was defined as shown in *Table 11*.

	Buffer thickness (cm)	**Temp (°C)**	**Water saturation (%)**	**concrete type**	**Steel overpack**	**Host rock clay**	**Glass**
task 4.1	30 (5 and 100 cm as variants)	25	100	young CEM I	5 cm thick Porous, with corrosion products	COx	ISG (fractured)

Table 11. Base case defined for the glass/steel/cement/clay system in Table 3-1 of D2.17.

The cases calculated in task 3.2 for the glass/steel/cement/clay system are given in *Table 12*. Case 3 in *Table 12* was a base case in D2.16 (Samper 2022), but not any more in D2.17 (De Windt 2022), in which there are no results for the modelling of this system.

	Buffer thickness (cm)	**Temp (°C)**	**Water saturation (%)**	**concrete type**	**Steel overpack**	**Host rock clay**	**Glass**
Young cement Case 1 (§ 4.3.2.1)	100	25	100	Young cement (pH 13.5)	5 cm thick Porous	COx	ISG (unfractured)
Young cement Case 2 (§ 4.3.2.1)	5	25	100	Young cement (pH 13.5)	5 cm thick Porous	COx	ISG (unfractured)
Old cement Case 3 (§ 4.3.2.2)	100	25	100	Old CEM I pH 10.5 Not fractured	5 cm thick Porous	COx	ISG (unfractured)

Table 12. Glass/steel/cement/clay cases studied in Task 3.2 to replace be base case for Task 4.1 given in Table 2-1 of D2.17.

The waste package scale calculations (by BRGM) in task 3.2 were thus performed for young and old cement. Waste package calculations specific for the bentonite-grout mixture were not performed.

4.3.2.1 Modelling of the system glass/steel/young cement/ COx

Using the model presented in section 4.2.2 (glass/steel/COx), a 100 cm thick young concrete layer (pH 13.5) was inserted between the steel and the COx clay (*Figure 45*) for modelling at the waste package scale at 25°C. Its composition was taken from D2.16 and is reported in *Table 13* (CSH1.2 was taken into account, but did not form). Moreover, the ISG glass (i.e. simplified composition) replaced the SON68. Additionally the temperature was decreased to 25 °C and a corrosion rate as function of pH was implemented (cf. D2.16). The applied effective diffusion coefficients were $3 \cdot 10^{-11}$ $m^2 \cdot s^{-1}$ at 25 °C for the COx and 10^{-12} $m^2 \cdot s^{-1}$ at 25 °C for the steel, the concrete and the glass.

Mineral name in THERMOCHIMIE	**Young concrete (mol $\cdot L^{-1}$ of rock)**	**Aged concrete (mol$\cdot L^{-1}$ of rock)**
Calcite	$1.92\ 10^{1}$	$2.18\ 10^{1}$
CSH1.6	$9.80\ 10^{-1}$	--
CSH0.8	--	$7.61\ 10^{-1}$
Ettringite	$4.22\ 10^{-2}$	$4.13\ 10^{-2}$
Hydrotalcite	$3.08\ 10^{-2}$	--
Monocarboaluminate	$7.63\ 10^{-2}$	--
Portlandite	1.51	--
Stratlingite		$9.03\ 10^{-2}$
Vermiculite-Ca		$4.11\ 10^{-2}$

Table 13. Mineralogical assemblages considered for the young (i.e. pH = 13.5 at 25 °C) and the aged (i.e. pH = 10.5 at 25 °C) concretes. Mineral concentration (mol L^{-1} of rock) calculated assuming a porosity of 10%, used in the BRGM model.

After the diffusion of alkalis (i.e. Na end K), the pH was controlled by the equilibrium between the porewater and the portlandite (i.e. pH = 12.5 at 25 °C). However, the phase was converted into calcite at the concrete – COx interface (*Figure 49*) leading to a pH decrease as well as the transformation of CSH1.6 into CSH1.2 and calcite. Such an evolution was fully consistent with expected processed (e.g. D2.16 and D2.17). Note that CSH0.8 precipitation has not yet occurred at 10,000 years because the space discretization at the concrete – COx interface (i.e. 5 mm) was too rough to decipher the process.

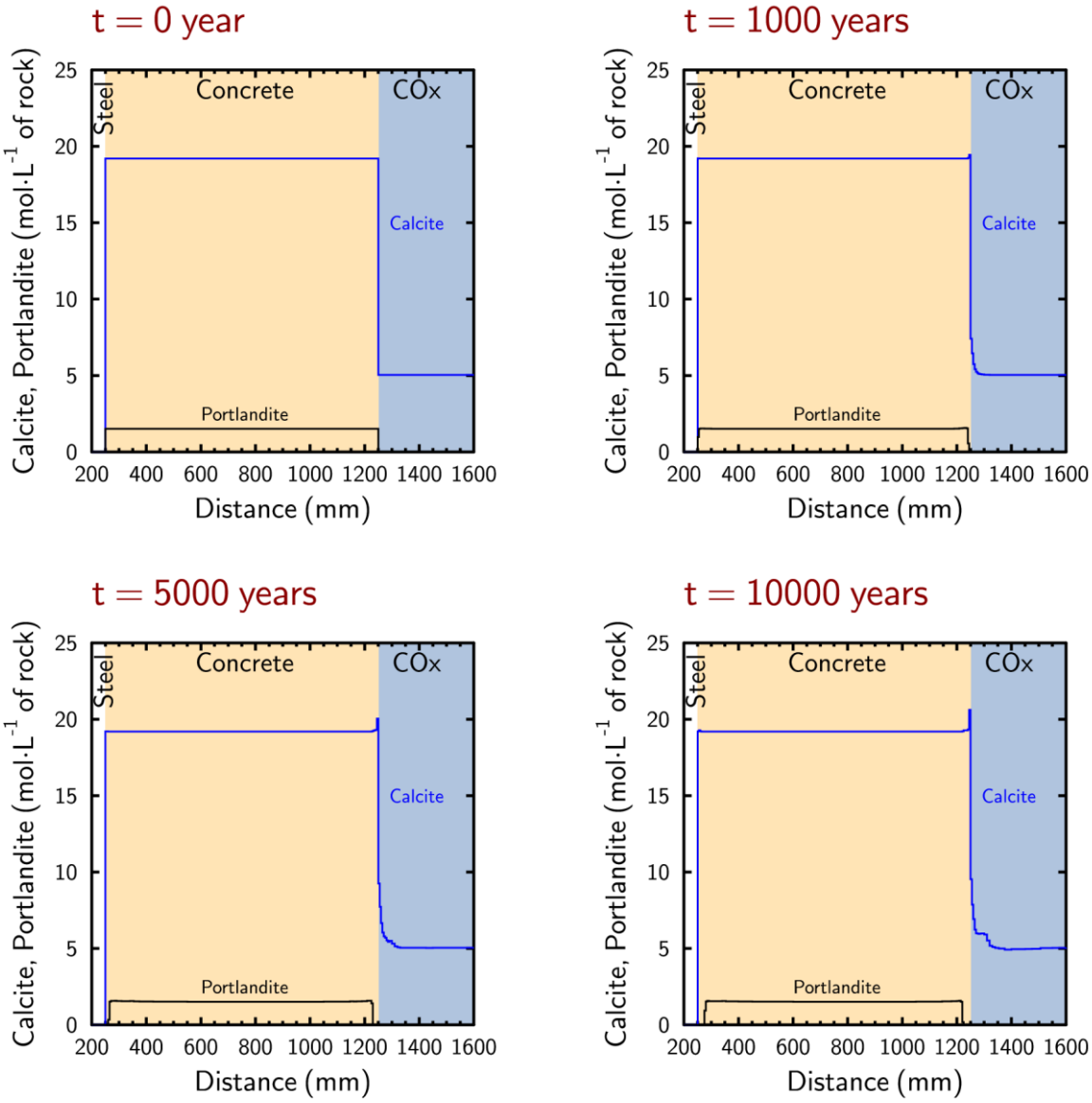

Figure 49. Young concrete carbonation at the waste package scale calculated with the BRGM model for a cement buffer of 100 cm thickness at 25°C.

Following the recommendation of D2.16 and D2.17, the steel corrosion rate was a function of pH. Over 10,000 years, average corrosion rates considering the pH evolution were 0.31 and 0.14 µm·year^{-1} at the glass – steel and the steel – concrete interfaces, respectively. In contrast to previous modelling, we note the precipitation of magnetite inside the cementitious material (*Figure 50*). Such precipitation was promoted by high pH conditions and should lead to the formation of a passive layer.

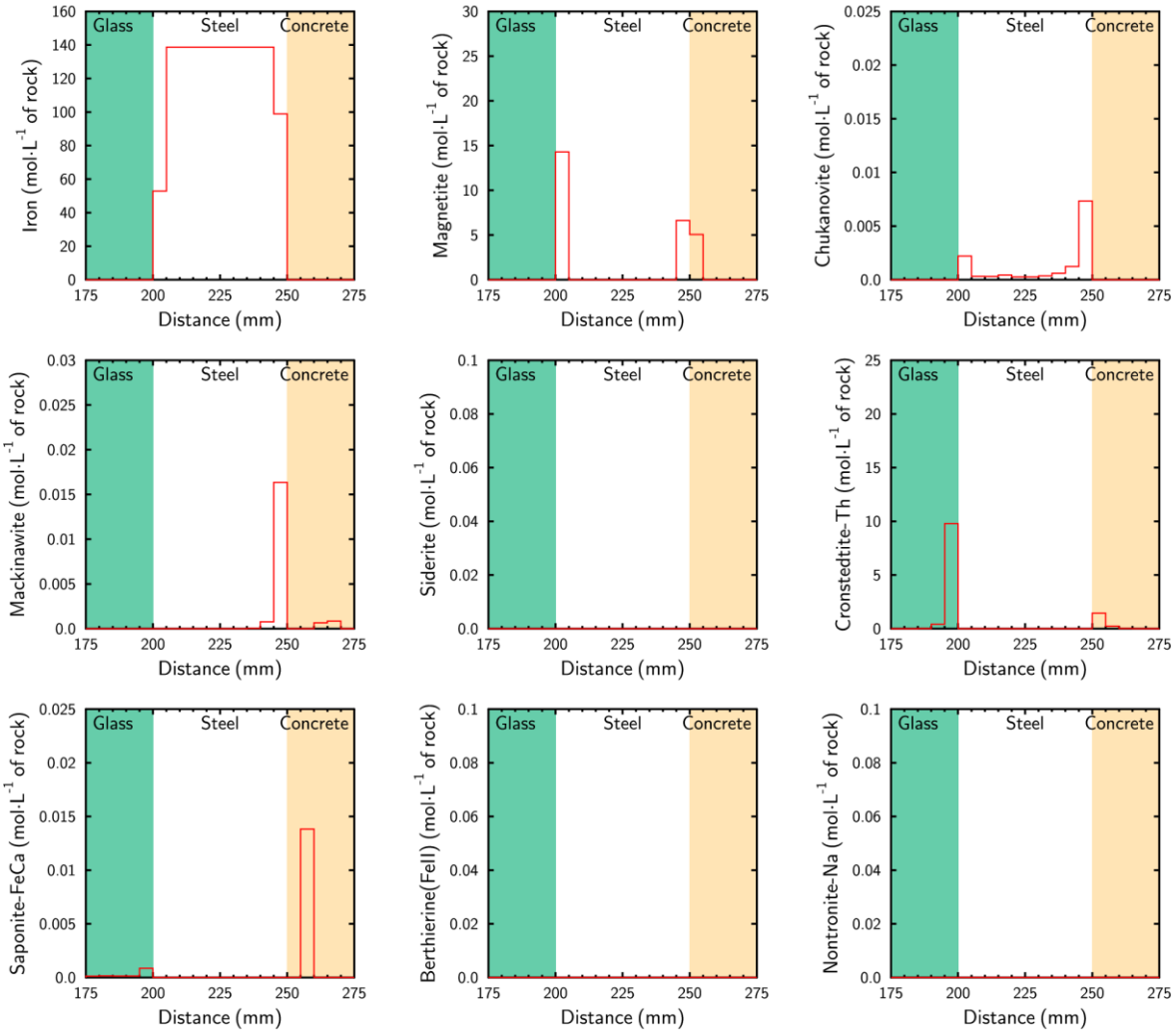

Figure 50. Corrosion products with a young concrete at the waste package scale calculated with the BRGM model after 10,000 years for ISG glass and a cement buffer of 100 cm thickness at 25°C.

Modelling indicated a glass alteration of 53.3 mm after 10,000 years (Figure 51). This would be more than 25% of the original glass block. Such fast dissolution may, however, be not relevant because the pH conditions were out of the validity domain of GRAAL (i.e. pH > 11, see Frugier 2018, Fournier 2018). Modelling only indicated the precipitation of gels as ISG-glass alteration products (passivating and non-passivating gels). Next to this, the assumption that the glass starts to dissolve already at t = 0 year, when the young concrete has not yet been altered and still has a high pH, is not the expected evolution scenario (see section 2.1.2)

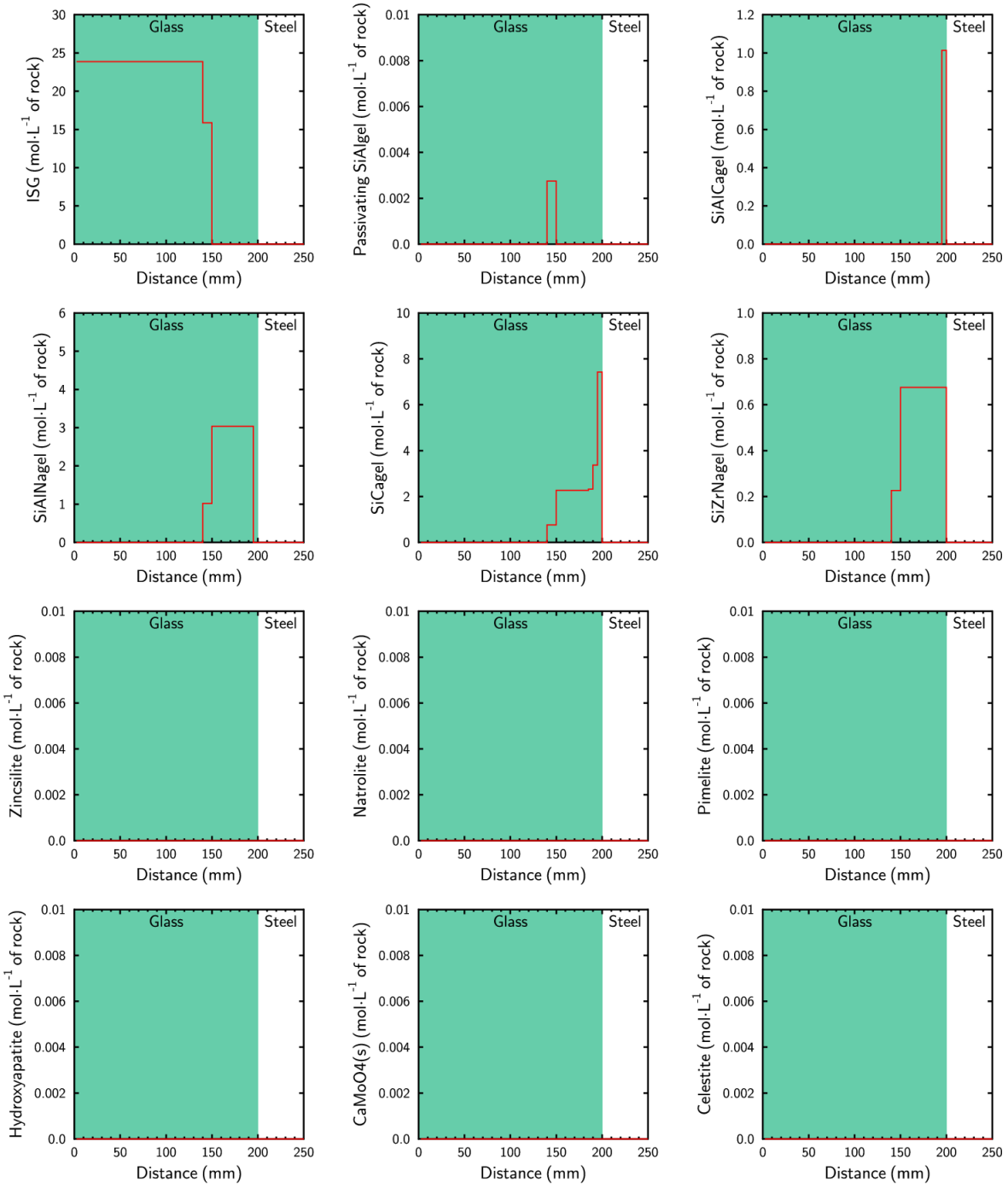

Figure 51. ISG glass alteration products calculated with the BRGM model at the glass – steel interface after 10,000 years with a young concrete at the waste package scale for a cement buffer of 100 cm thickness at 25°C.

The glass alteration rate evolved in the first years but remained nearly constant after 500 years at about 6 µm.year^{-1}, this is about 0.04 g·m^{-2}d^{-1} (*Figure 52*). In contrast, the steel corrosion rate was nearly constant over 10,000 years. Overall, the large amount of young concrete (i.e. 1 m, see *Figure 45*) led to slow steel corrosion rates but increased glass dissolution.

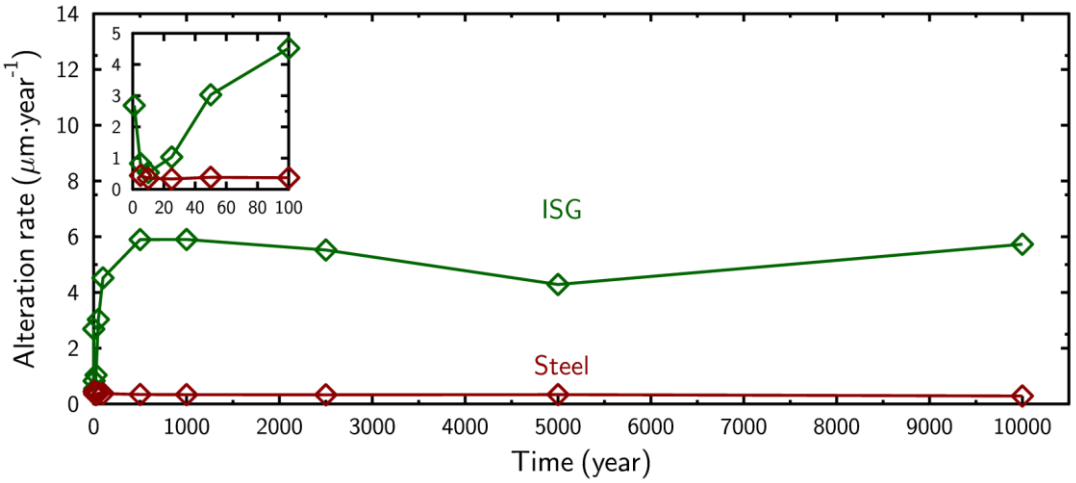

Figure 52. Alteration rates calculated at the waste package scale with the BRGM model at the ISG glass – steel interface with a young concrete for a cement buffer of 100 cm thickness at 25°C.

A sensitivity test was carried out with 5 cm of young concrete instead of 1 m (case 2 in *Table 12*). Numerical results indicated a significant decrease of the glass alteration: 9.2 mm after 10,000 years of simulated time. Alteration rates are reported in *Figure 53*. The reason for this fast rate decrease is the fact that with only 5 cm buffer, the young concrete evolves to aged concrete within 500 years. The old concrete does not have any portlandite anymore (explaining the lower glass dissolution rate) and has a lower pH (10.5) explaining the higher steel corrosion rate.

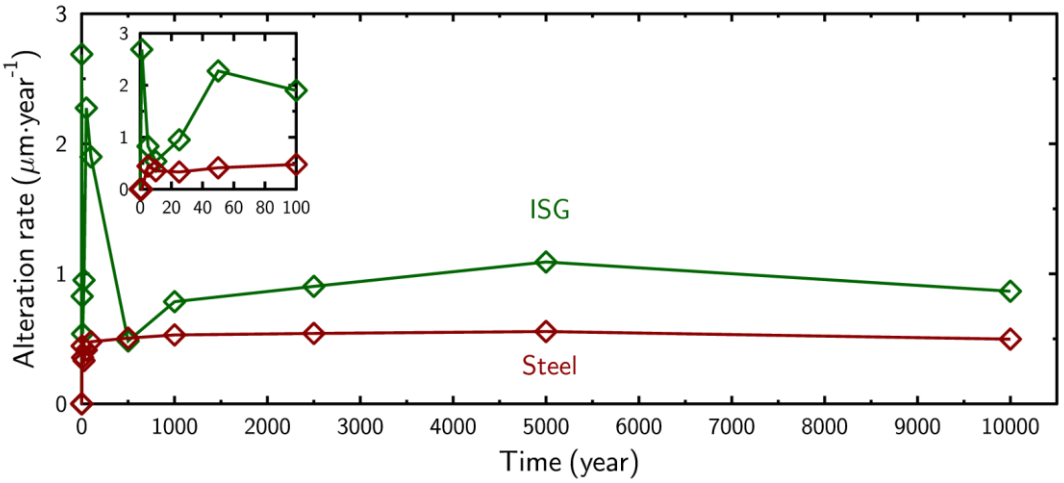

Figure 53. Alteration rates calculated at the waste package scale with the BRGM model at the ISG glass – steel interface with a young concrete for a cement buffer of 5 cm thickness at 25°C.

4.3.2.2 Modelling of the system glass/steel/old cement/COx

Finally, 1 m of an aged concrete was implemented (case 3 in *Table 12*). Its composition was determined with PHREEQC (batch calculation). First, the young concrete (i.e. pH = 13.5 at 25 °C) was depleted in alkalis (i.e. Na and K) leading to a pH of 12.5 at 25 °C. Hereafter, CO_2 was added until to reach a pH of 10.5 at 25 °C. For the sake of consistency with previous modelling, the same selection of secondary

phases has been considered during the concrete carbonation. The resulting mineralogy consisted in an assemblage of calcite, CSH0.8, ettringite, stratlingite and vermiculite-Ca (*Table 13*). Such a composition reflected a partial carbonation of the concrete (e.g. Glasser 2007).

After 10,000 years of simulated time, modelling showed CSH0.8 carbonation in the near field of the COx (*Figure 54*). Moreover, the alteration profile highlighted the formation of saponite and vermiculite at the interfaces.

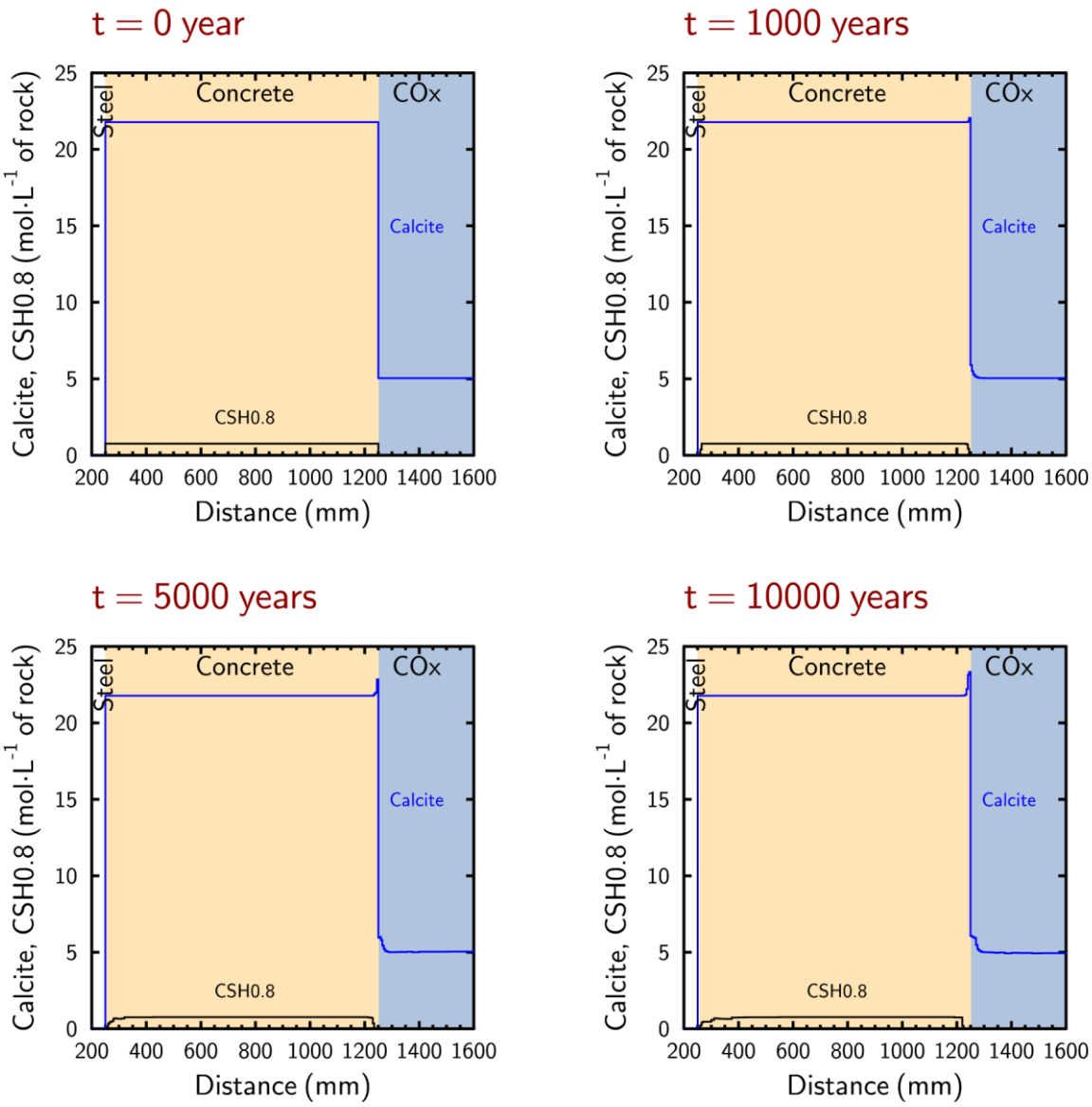

Figure 54. Aged concrete carbonation, calculated with the BRGM model at the waste package scale at 25°C.

Over 10,000 years, average steel corrosion rates were 0.46 and 0.32 µm·year^{-1} at the glass – steel and the steel – concrete interfaces, respectively. The lower pH related to the consideration of an aged concrete led to higher steel corrosion rates than expected with a young concrete. Thus, the nature of corrosion products at the steel – concrete interface was slightly modified with the formation of berthierine(FeII) (*Figure 55*).

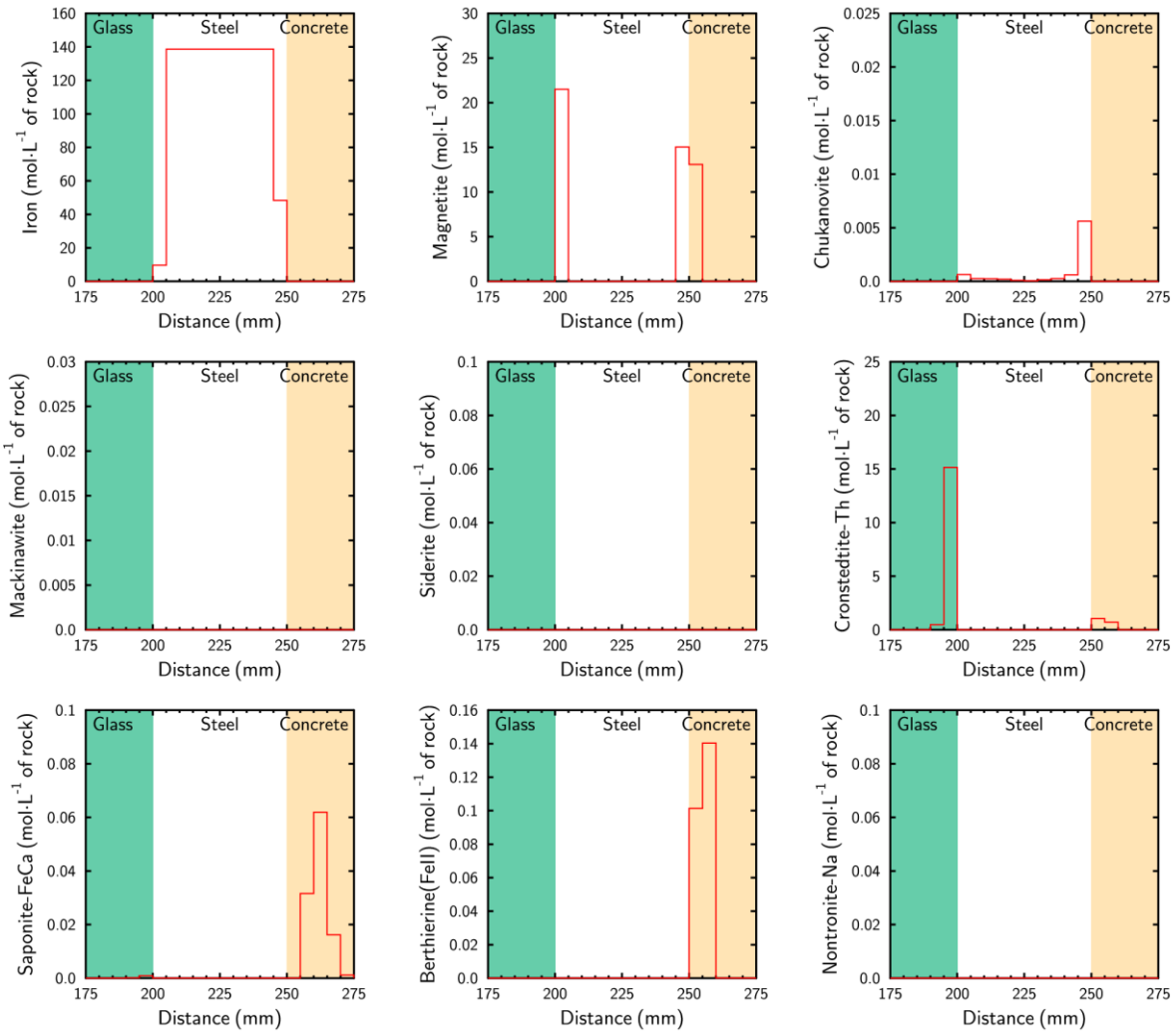

Figure 55. Corrosion products after 10,000 years, calculated with the BRGM model for ISG glass and an aged concrete at the waste package scale at 25°C.

The numerical results indicated a glass alteration of 8.8 mm after 10,000 years (*Figure 56*). The consideration of an aged concrete decreased the glass dissolution but alteration products were similar to those simulated with a young concrete.

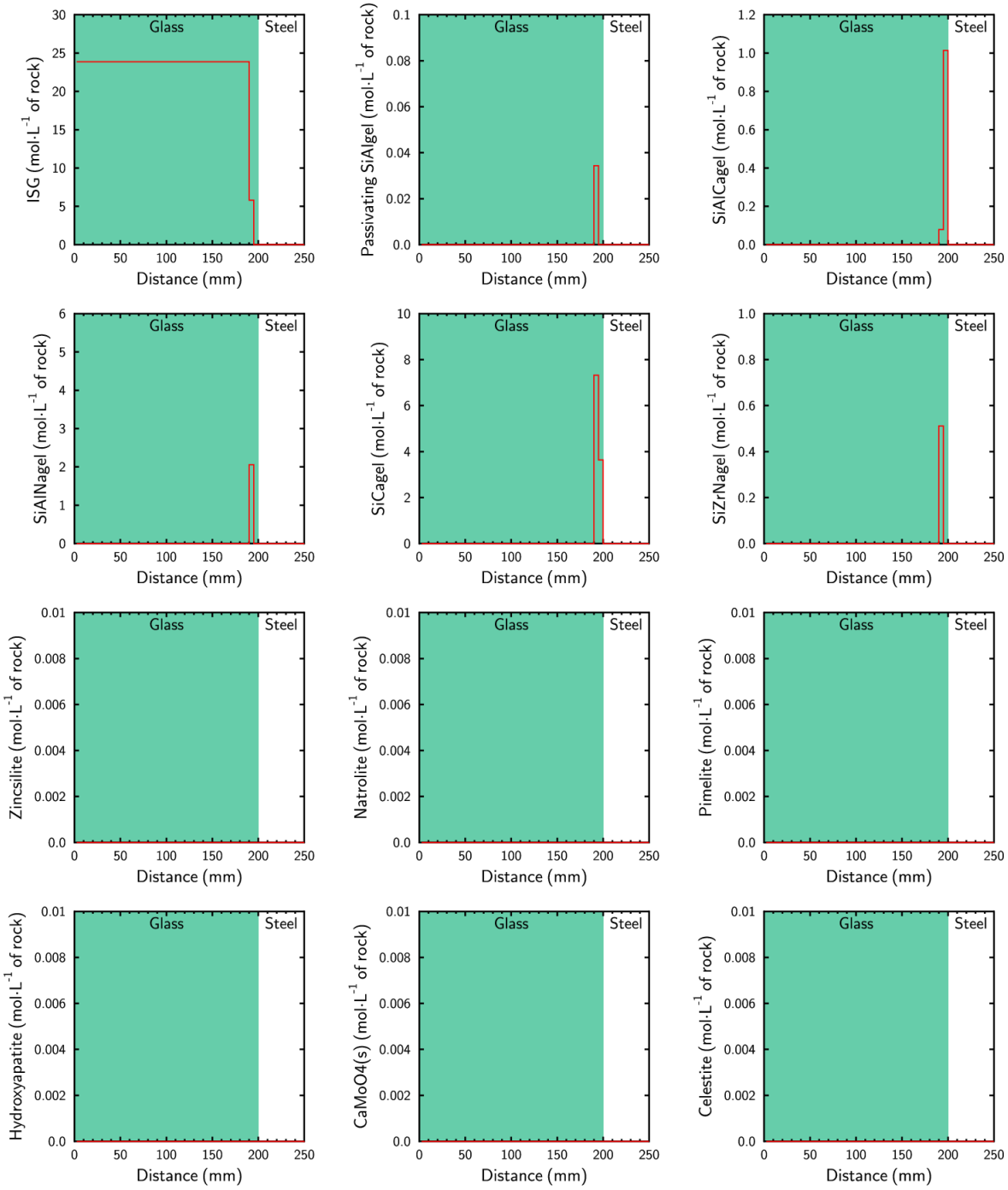

Figure 56. ISG glass alteration products at the glass – steel interface after 10,000 years, calculated with the BRGM model for an aged concrete at the waste package scale at 25°C.

The evolution of the glass alteration rate and the steel corrosion rates at the glass – steel interface are shown in *Figure 57*.

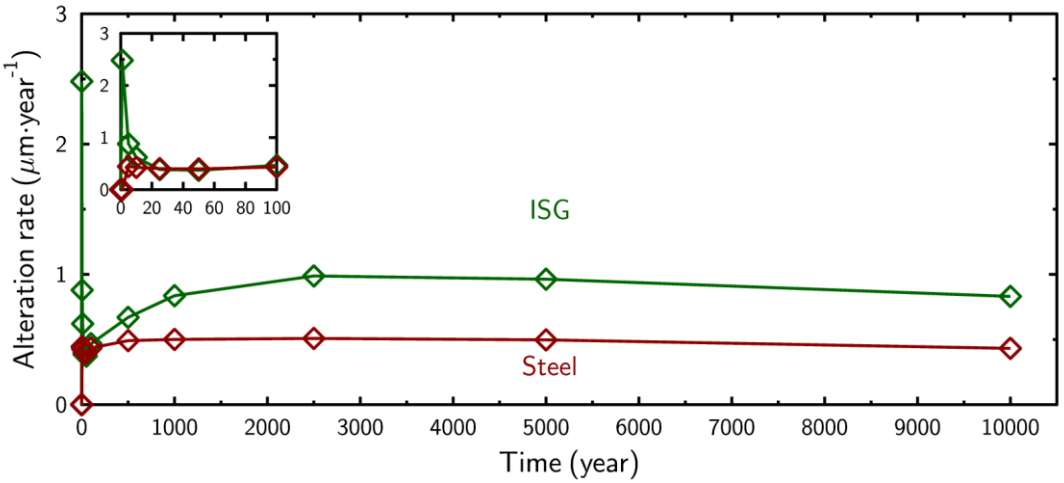

Figure 57. Alteration rates at the ISG glass – steel interface, calculated with the BRGM model for an aged concrete at the waste package scale at 25°C.

4.3.3 Conclusions for the modelling at waste package scale

- The modelling strategy has attempted to link the modelling of Experiment 3 with the modelling at the waste package scale. Therefore, parameters used in the modelling of the experiments were gradually modified to get a generic case (i.e. temperature, glass composition etc.). At the same time, several modelling assumptions, such as the selection of secondary phases or the implementation of the GRAAL model, remained identical for the modelling both at the waste package scale and the experiment scale. Overall, the upscaling (i.e. space discretization of 5 mm rather than 1 µm at the interfaces and the consideration of the steel as a permeable medium) did not indicate significant modifications of numerical results and was supposed as valuable.
- The modelling of generic cases indicated that the steel corrosion products were quantitatively and qualitatively dependent on the corrosion rate and the chemistry of the surrounding environment.
- The consideration of old concrete resulted in faster corrosion rates than those involved with a young concrete.
- Overall, magnetite and iron silicate were predicted at the glass – steel interface.
- COx – steel interactions led to the precipitation of magnetite and iron carbonates with the possible formation of cronstedtite (depending on the modelled time) due to the Si diffusion from the glass (as steel is treated as a porous material).
- Magnetite was the main corrosion product expected at the concrete – steel interface.
- The glass dissolution rate appeared to be function of both the steel corrosion rate and the chemistry of the surrounding environment.

4.3.4 Modelling cases and results for the HLW/steel/cement/clay system (SCK CEN)

The diffusion model that was used by SCK CEN has been validated only at the high pH of young cement water. It has not been validated at the lower pH that is expected to occur as a result of the evolution of the concrete (see section 2.1.2). Hence, the applicability of the model for long-term simulations of the base case defined in *Table 11* is very limited. Still a calculation was performed in which the model simulating the experiment (section 3.3) was allowed to run for several days to see how much glass must dissolve for the glass compartment to reach a pH 10 - 10.5, where the conventional affinity driven dissolution models are applicable. This is the hypothetical pH decrease caused by the dissolution of the glass only, without consideration of the pH decrease of the concrete by the interaction with the host rock. The result is shown in *Figure 58*. The calculation was done with the following parameters:

- D_{glass} = 8.25 x 10^{-22} $m^2 \cdot s^{-1}$ (cfr. Mockup tests)
- D_{cement} = 1.70 x 10^{-14} $m^2 \cdot s^{-1}$ (cfr. Mockup tests)
- Large glass surface area (SA/V = 75000 m^{-1})
- Temperature = 25°C

Figure 58 shows that to decrease the pH from 13.6 to 10.5 in the experiment, nearly 400 grams of SON68 glass needs to be dissolved per liter of young cement water (YCWCa).

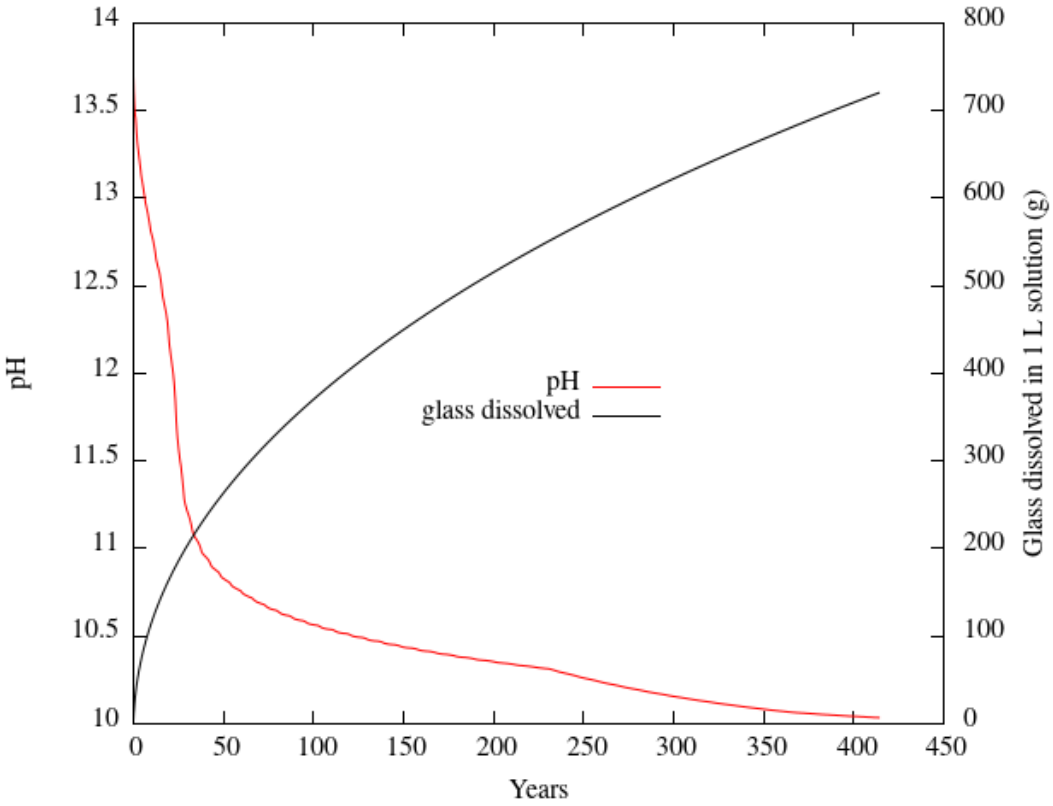

Figure 58. Evolution of the pH and the cumulated amount of glass dissolved in 1L YCWCa for a long-term extrapolation of experiment 3, calculated with the SCK CEN model at 25°C.

This would be reached in less than 150 years. This suggests that, in the unlikely event that the glass would come in contact with the young cement water, only a relatively small amount of glass has to dissolve to decrease the pH at the glass surface to the pH range where the classical dissolution models can be used, based on affinity (degree of undersaturation). Because in reality perforation of the overpack

is expected only when the pH of the cement buffer is close to 10.5, the actual amount of glass needed to reach pH 10.5 would even be smaller. A more precise calculation should consider the actual disposal geometry and the impact of the steel corrosion products. Because of the low steel corrosion rate at high pH, the steel corrosion products may have an effect only when the pH is already close to 10.5. These conclusions are based on the assumption that the diffusion model is applicable in the pH range 10 – 13.6. With the limited experimental dataset available today for glass dissolution in this pH range (in contact with aged, neutralized cement), this assumption is not sufficiently supported, though. It is likely that the dissolution rate of the glass will decrease with the decreasing pH, implying that the glass would dissolve slower than in *Figure 58* and that the pH will decrease slower, but the amount of glass that has to dissolve to reach pH 10.5 may be similar. Experimental validation of these conclusions and the model (or another model) in this pH range is necessary to increase the confidence in the results.

5 Synthesis for upscaled modelling

In this section, we present the main considerations regarding the upscaling.

- The model used for the simulation of Experiment 3 could be used to model the steel/CO_X and the glass/steel interaction for periods up to 10 000 years. The upscaling required a space discretization of 5 mm rather than 1 µm at the interfaces and the consideration of the steel as a porous media, but this did not lead to significant modifications of the numerical results.

- The selection of iron corrosion products and secondary phases used in the model in task 3.2 was different from the selection for the disposal cell modelling in task 4.1 described in EURAD-ACED deliverable D2.17 (De Windt 2022). The latter model only considers magnetite, greenalite, and siderite. Other corrosion products (chukanovite, mackinawite, saponite-FeCa, berthierine(FeII), cronstedtite-Th, considered in task 3.2 are not considered in task 4.1. Greenalite was discarded from the model in task 3.2, because it would lead to a glass dissolution rate higher than observed in the experiment with COx at 70°C (Experiment 3, section 3.1.2). Still, it was observed with SON68 in contact with COx at 50°C in another experimental setup (Dillmann 2016), as mentioned in EURAD-ACED deliverable D2.5 (Deissmann 2020). The models in task 3.2 and task 4.1 both consider triggering of the glass dissolution by formation of iron silicates. The fact that greenalite leads to faster dissolution than berthierine (FeII) or cronstedtite-Th with the GRAAL model in task 3.2 suggests that the nature of the iron silicate affects the glass dissolution kinetics in the modelling as long as the iron is corroding. The modelled cases do not allow to evaluate how important the selection of iron corrosion products (magnetite, siderite, chukanovite…) and iron silicates greenalite, berthierine, cronstedite…) is for the long-term glass dissolution kinetics. We can only conclude that the selection made in task 4.1 does not consider some phases that are suggested by the model in task 3.2. This may be partly due to the differences in the system (clay, temperature).

- Because task 3.1 did not include any tests with bentonite (e.g. Febex), there was no modelling of such experiment. Instead, Experiment 3 with interaction with COx clay was modelled. Still, the modelling in D2.17 was done with FEBEX bentonite (for ISG at 32°C). The physicochemical characteristics of Febex bentonite and COx clay are different, as illustrated in *Table 14* for some parameters that should have an effect on the glass dissolution and the secondary phase formation, but a systematic study of this effect goes beyond the scope of task 3.

	Febex (D2.17)	**COx (D2.12)**
pH	6.46	≈6.8
$HCO3^-$	$7.59x10^{-3}$ mol·L^{-1}	$3.80x10^{-3}$ mol·L^{-1}
Ca	$3.32X10^{-2}$ mol·L^{-1}	$9.93x10^{-3}$ mol·L^{-1}
Mg	$3.67x10^{-2}$ mol·L^{-1}	$4.10x10^{-3}$ mol·L^{-1}
D_e	$4.07x10^{-11}$ m^2·s^{-1}	$5.6x10^{-11}$ m^2·s^{-1}
Porosity	40.7 %	18 %

Table 14. Comparison of some physicochemical characteristics of Febex bentonite and COx clay.

- An important upscaling problem is associated to the consideration (or not) of the fractures in a glass block. In contrast to the models used in task 4.1, the models used in task 3.2 do not consider these fractures. Whereas in task 3.1 a layer-by-layer glass dissolution is assumed, thus neglecting the effect of fractures in the glass block, the model used in task 4.1 considers this effect in a simplified way. The fractures were not explicitly modelled, but a high diffusion coefficient was used for the species that dissolve from the glass and diffuse through a growing glass alteration layer (10^{-13} m^2·s^{-1} <25,000 years, 10^{-10} m^2·s^{-1} >25,000 years). In this way, a "fractured" block in a representative elementary volume is simulated at a scale of several cm, within which the dissolved species can diffuse and reach the inner zone of the block quite readily. This diffusion coefficient is much larger than the one used for transport of species in the unfractured glass alteration layer in the mechanistic models task 3.2. The diffusion coefficient used in the performance assessment driven model of task 4.1 thus has a meaning that is different from the diffusion coefficient used in the mechanistic modelling of task 3.

- The modelling of Experiment 4 suggests diffusion coefficients for boron in the altered young cement paste that are 100 to 1000 times smaller than the values usually assumed for cement and that were used also for the disposal cell calculations in D2.17. There are indications that these low D_e values are applicable also for silica released by the glass. It is not clear if the low D_e values are due to the boron and silicon speciation, or to a lower diffusivity of the altered cement paste. Such low diffusivity would slow down the interaction between the glass and the cement.

- For the very high pH conditions in young cement, three very different glass dissolution models have been used.
    - To model Experiment 4 with young cement and pH about 13.5 (section 3.3.2), a diffusion driven glass dissolution model was used, assuming isovolumetric dissolution/reprecipitation. In this model, all kinetics is represented in one lumped parameter, i.e. the diffusion coefficient. Because of the very high pH, an affinity effect where increasing Si concentrations cause a decrease of the glass dissolution rate is not considered. The selection of secondary phases allowed to precipitate on the glass surface still affects the concentrations of the solubility limited glass constituents (Si, Al, ….) that diffuse further in the compartment with the hardened cement paste.
    - To model the young cement system at waste package scale (section 4.3.2.1), the GRAAL model was used, in which the concentrations of glass constituents in solution determine the glass dissolution rate via the formation of a passivating SiAl gel. In this model, the glass dissolution kinetics depend directly on the selection of secondary phases. The results of this modelling exercise may be not relevant because pH conditions were out of the validity domain of GRAAL (i.e. pH > 11, see Frugier 2018, Fournier 2018).
    - In D2.17 also an affinity driven glass dissolution model is used for the disposal cell calculations with young CEM I (see *Table 11*). However, in this more complete system

simulation, the pH of the concrete decreases to <10 by the time of the perforation of the overpack, as a result of the processes mentioned in section 2.1.2. Hence the affinity driven glass dissolution model can be applied.

- The diffusion driven high pH model was not used at waste package scale, but a calculation was performed in which the model simulating experiment 4 was allowed to run for several days to see how much glass must dissolve for the glass compartment to decrease the pH at the glass surface from 13.6 to pH 10 - 10.5, where the conventional affinity driven dissolution models are applicable. The conclusion was that a relatively small amount of glass is required for this. Experimental validation of the model (or another model) in this pH range is necessary to increase the confidence in this conclusion.

- The modelling of experiment 3 with glass/steel/COx suggests that the pH increase due to steel corrosion is significant at the clay side and at the glass side. At the glass coupon side, it is 10.8 at 70°C (so about 12.3 at 25°C) for a steel corrosion rate of 2 µm/y. At the clay side, the pH would be 10.2 at 70°C. This is to be compared with the pH of about 7.0 at 25°C for the COx host rock. The negative feedback effect of the higher pH on the steel corrosion rate (lower corrosion rate at higher pH) was not considered, although it would be two orders of magnitude lower at pH 12 than at pH 8 (Figure 3-6 in D2.17). This is related to the way in which the steel corrosion equation is defined. In cementitious media with high initial pH, the steel corrosion rate is much lower than in clay media. Hence the resulting pH increase due to the steel corrosion is also less important.

- Experiment 1 with SON68 in contact with a corroding piece of iron and COx clay at 50°C, showed higher steel corrosion rates than those observed in experiment 3 (SON68 in contact with corroding iron on COx at 70°C), where a steel corrosion rate of 2 µm·year^{-1} was assumed. In experiment 1, an iron corrosion product layer up to 100 µm was found after 2.5 years, this is 40 µm·year^{-1}, but the layer thickness increased slower between 2.5 and 6.1 years, and the layer thickness was very variable (5 to 100 µm after 2.5 years, 15 to 120 µm after 6.1 years, see D2.12). Hence there is a relatively large uncertainty on the steel corrosion rate, both on the extent and on the evolution with time (constant or decreasing). Although the steel corrosion rate apparently decreased with time, the glass dissolution rate was similar for the tests at 2.5 and 6.1 years. Because the steel corrosion provides iron for the formation of iron phyllosilicates that prevent the formation of a passivating amorphous silica gel, the assumptions made for the steel corrosion rate have a direct impact on the glass dissolution rate. Assumptions like a constant corrosion rate triggering the glass dissolution at a constant dissolution rate may be overconservative. For the disposal cell calculations in D2.17, a constant corrosion rate of 1.41 µm·year^{-1} was used.

- Experiment 2 (simplified glass composition in contact with compact Boda clay with iron particles at 80°C) showed lower dissolution rates than experiment 1, but in this setup there was no direct contact between glass and iron. Experiment 3 and 4 confirmed the importance of distance between the glass surface and the reacting EBS material (iron or cement paste). The glass alteration increasing effect is restricted to the outer layer.

- Pore clogging close to the interface is a process with potentially large impact on the glass alteration rate and the evolution of the contacting engineered barriers. In report D2.17, the so called 'porosity feedback effect' would lead to a much slower glass dissolution with the bentonite buffer and with the cement buffer. In the bentonite buffer, the porosity in the steel corrosion layer would decrease very much as a result of magnetite precipitation. In the cement buffer, corrosion products (magnetite, greenalite) could also decrease the porosity, but apart from this also the precipitation of saponite, C-A-S-H and calcite could lead to a porosity decrease in the cement layer and slow down any chemical degradation. On the other hand, decalcification of the cement might increase the porosity and transfer properties, thus enhancing the progression of the diffusion fronts and the chemical

evolutions in relation to neutralisation of the cement buffer. The experiments and their modelling in task 3 did not provide direct evidence for a pore clogging effect in the clay medium, but the boron profiles in the hardened OPC paste of Experiment 4 suggest a low diffusivity in the cement layer next to the glass (D_e lower than found in literature for various cement media). This can be an indication for a decrease of the effective porosity and might be related to the formation of CSH1.2, but this is not yet a complete pore blocking.

- The experiments and modelling show that perforation of the overpack is delayed by using a high pH buffer (using cementitious materials) that decreases the overpack corrosion rate and by increasing the thickness of the overpack. Using a thicker cement buffer provides al longer protection, but once the overpack is perforated, the formation of iron-silicate phases is expected to trigger the glass dissolution. There is thus a trade-off between the short term advantage and long-term disadvantage of using a thicker overpack.

- The high pH of young cement will also trigger the glass dissolution. The waste package calculations of section 4.3.2 (*Figure 52*) suggest a rather constant high long-term dissolution rate, of about 5 µm/year for the ISG glass. Experiment 4 shows that – with a stainless steel filter separating glass from young cement paste – the dissolution rate of SON68 was < 1 µm/year for the glass particles close to the filter and the HCP. This would be considerably lower, although the ISG would have a similar dissolution rate as SON68 at high pH in dynamic tests, i.e. in diluted conditions with a continuous flow of the high pH leachant (Elia 2017, Caes 2020). Tests in young cement water show that at very high SA/V (without cement paste) even in this medium very low long-term dissolution rates are reached (100 times lower than in experiment 4), probably as a result of the pH decrease imposed by the glass dissolution and precipitation of secondary phases (Ferrand 2021). If we see still a higher dissolution rate in experiment 4, it must be because of the interaction with the cement, which is diffusion controlled. Hence a further long-term decrease of the glass dissolution rate in the presence of cement paste can also be expected. In the most likely evolution scenario, the concrete will be transformed into aged concrete by the time the overpack is perforated. The modelling in section 4.3.2. (*Figure 53*) shows a lower long-term glass alteration rate of about 1 µm/year, but for this medium (aged cement, C-S-H phases with pH 10.5) no experimental data are available to validate the model. Also the bentonite-grout mixture from Exp 2 did not give information about this, because the bentonite-grout layer was too thin.

6 Recommendations for future experimental and numerical work

As shown in section 5, the work performed for task 3 in EURAD-ACED has contributed to a better understanding of the coupled dissolution, corrosion and transport processes expected in a HLW disposal system, but important questions remain to be solved. This section presents a number of recommendations for future experimental and numerical work, based on the experience of task 3.

- The secondary phases formed during the alteration of the glass, steel, clay or cement experiments are often difficult to identify and thermodynamic and kinetic data are sometimes not available. This is the case for the systems with clay buffer and with cement buffer. A good characterization in a range of disposal relevant conditions is important to better assess the phases that can be expected in situ. With the clay buffer, the experimental data on the formation of greenalite are not consistent, although this mineral was used as iron silicate mineral in the upscaled modelling of task 4.1. To verify to which extent the selection of a particular set of secondary phases (like iron silicates) has an effect on the predicted glass dissolution rate, a set of calculations should be done, using different minerals. This was not done in EURAD-ACED.

- To simulate the glass dissolution kinetics at very high pH (13.5), only a high-level diffusion driven dissolution model is available. The GRAAL model is not applicable in this pH domain. In the most likely evolution scenario, the pH of the cement buffer will be lower when the glass comes in contact with the pore water, but it may still be higher than 10 or 11, so higher than the pH range where the glass dissolution is assumed to be affinity driven, and where the GRAAL model has been validated. Even with bentonite, a local high pH can be reached. In the calculation in D2.17 for bentonite and pore clogging, the glass dissolution rate is low although the pH would be 12.5 due to the residual dissolution (Fig 2-49 in D2.17). A pH >12 can be reached at the glass surface with bentonite buffer also due to the steel corrosion. The glass dissolution behaviour in the range pH range 10 – 12.5 is not well known. More studies to support and validate the models for this pH range would be corroborate the credibility of the long-term modelling.

- To validate the reactive transport models that include the subsequent interfaces expected in real disposal conditions, integrated experiments are necessary that focus explicitly on these coupled mechanisms. The experiments that were available for validation of the models in EURAD-ACED have been valuable in this regard, but were far from sufficient. Parametric experimental studies are necessary rather than isolated experiments with a minimum parameter set. These tests should be done in the pH range 10-12.5.

- The materials that will be used in the future deep disposal structures may be different from the reference near field materials that are studies today. Hence a better insight is necessary in the material characteristics that have most impact. This can be part of a parametric approach.

- The tests that were used in task 3.2 to support the modelling were performed in conditions that tend to accelerate the glass alteration, i.e. either high temperature (70°C, Experiment 3) or high pH (13.5, Experiment 4). To validate the models for the expected conditions, tests should be done also on these less aggressive conditions, causing slower glass alteration. This can be part of a parametric approach.

- The low diffusion coefficient for boron and silicon species in altered young cement found in Experiment 4 suggest that diffusion coefficients usually assumed in cement may overestimate the diffusion coefficients of the relevant glass species in the cement layer that is altered by the interaction with the glass. This interpretation assumes that silicon species have a similar diffusion

behaviour as boron species (but is involved in secondary phase formation, while boron is not). Targeted experiments could confirm this hypothesis, e.g. an experiment using glass (or solutions) with specific Si isotopes that can be distinguished from the original Si in the HCP. Such experiments should also make clear if the low diffusivity is due to the speciation of the silica or to a change in the properties of the altered cement versus the unaltered cement.

- The conditions inside the glass fractures are different from the conditions on the outside of the glass block, and this can lead to a different dissolution behaviour. This has been illustrated by Experiments 2 and 3 in task 3.1 of EURAD-ACED. In both experiments compartments filled with glass powder were used, and in both cases the glass particles close to the steel interface were altered more than the particles deeper in the glass compartment. This aspect was modelled for Experiment 3 (section 3.1.5.2.3) but not for Experiment 4. In task 4.1 the effect of the cracking has been modelled in a very abstract way, using a large diffusion coefficient for diffusion in the glass, but this model could not be validated or calibrated with the experiments. Specific experiments would be necessary for this.

- Because the alteration processes are slow, and because alteration products may evolve further with time, it is very important to perform tests of very long duration, i.e. several decades. Such data are crucial to validate the models based on short term experiments.

- Anaerobic steel corrosion can lead to the accumulation of H_2 gas inside the overpack (and glass canister). This phenomenon was not studied experimentally. By attributing a porosity to the overpack, the accumulation of H_2 was avoided for the modelling in task 3. Still it would be interesting to explicitly consider the effects of the H_2 accumulation, to see under which conditions a separate gas phase would be formed, which would probably delay the further corrosion of the steel and alteration of the glass.

- The anaerobic steel corrosion leads to a local pH decrease. This should lead to a decrease of the steel corrosion rate. This evolution is not explicitly considered in the modelling of Experiment 3 in task 3.2. Experiments that study simultaneously the glass dissolution and steel corrosion, providing good quantitative data are missing. Future experiments might consider to include this objective.

- A lot of systems have been modelled in task 3.2 and in task 4.1 (D2.17) generating a lot of graphs, but because there is no common standard, a quantitative comparison of the results is difficult and only general qualitative conclusions are possible. A suitable common standard could be the remaining fraction of glass after a certain period of time, because this is directly linked to the source term. With such a standard, one could quantify the effect of parameter variations, such as the effect of specific corrosion products or iron silicates (greenalite, siderite…) on the life time of the glass. If the lifetime is almost the same, regardless the exact secondary phase, one can simplify the calculations for upscaling by considering only one product. In a similar way, one could quantify the effect of the overpack steel thickness, the buffer thickness, the consideration of fractures in the glass or in the concrete, the use of a different glass dissolution model etc… Because the calculations are time consuming, only a very limited set of calculations could be performed for task 3 in EURAD-ACED, but it would be useful to continue this kind of calculations in a future program.

References

Avrami, M. (1939). Kinetics of Phase Change. I General Theory, J. Chem. Phys. 7, 1103-1112

Azoulay, I., Rémazeilles, C., and Refait, Ph. (2012). Determination of standard Gibbs free energy of formation of chukanovite and Pourbaix diagrams of iron in carbonated media, Corrosion Science 58, 229-236.

Bajja, Z., Dridi, W., Larbi, B., and Le Bescop, P. (2015). The validity of the formation factor concept from through-out diffusion tests on Portland cement mortars, Cement and Concrete Composites 63, 76-83

Beaudoin, J., Odler, I. (2019). 5 - Hydration, Setting and Hardening of Portland Cement, in: Hewlett, P.C., Liska, M. (Eds.), Lea's Chemistry of Cement and Concrete (Fifth Edition). Butterworth-Heinemann, pp. 157-250.

Bernard, O., Ulm, F.-J., Lemarchand, E. (2003). A multiscale micromechanics-hydration model for the early-age elastic properties of cement-based materials. Cement and Concrete Research 33, 1293-1309.

Bildstein, O., Lartigue, J.-E., Schlegel, M.L. *et al.* (2017). Gaining insight into corrosion processes from numerical simulations of an integrated iron-claystone experiment. Radioactive Waste Confinement: Clays in Natural and Engineered Barriers, S. Norris, J. Bruno, M. van Geet, E. Verhoef

Blanc, Ph., Lassin, A., Piantone, P., *et al.* (2012). M. Thermoddem: A geochemical database focused on low temperature water/rock interactions and waste materials, Applied Geochemistry 27(10), 2107-2116.

Blanc, P., Vieillard, P., Gailhanou, H., Gaboreau, S., Marty, N., Claret, F., Madé, B., Giffaut, E. (2015). ThermoChimie database developments in the framework of cement/clay interactions. Applied Geochemistry 55, 95-107.

Blanc P, Debure M., Govaerts J., Gu Y., Jacques D., Kosakowski G., Leivo M., Marty N., Neeft E., Shao H., Vehling F. (2024). Description of ILW modelling results and recommendations for future experiments and numerical work: Deliverable 2.15 of the HORIZON 2020 project EURAD. EC Grant agreement no: 847593.

Bourdelle, F, Mosser-Ruck, R., Truche, L., *et al.* (2017). A new view on iron-claystone interactions under hydrothermal conditions (90°C) by monitoring in situ pH evolution and H_2 generation, Chemical Geology 466, 600-607.

Caes, S., Ferrand, K., and Lemmens, K. (2020), Topical report on dynamic dissolution tests on SON68, SM513 and ISG glasses, SCK CEN report ER-0729

Carriere, C., Neff, D., Martin, C., *et al.* (2020). AVM nuclear glass/steel/claystone system altered by Callovo–Oxfordian poral water with and without cement–bentonite grout at 70°C. Materials and Corrosion, 1-9

Chivot, J. (2004). Thermodynamique des produits de corrosion, Andra, collection sciences et techniques, 341 pages

Deissmann, G., Ait Mouheb, N., Martin, C., Turrero, M.J., Torres, E., Jacques, D., Weetjens E., Kursten B., Cuevas, J., Samper, J., Montenegro, L., Leivo M., Somervuori, M., Carpen, L. (2020): Experiments and numerical model studies on interfaces. Final version as of 12.05.2021 of deliverable D2.5 of the HORIZON 2020 project EURAD. EC Grant agreement no: 847593.)

De Windt L., Samper J., Cochepin B., Garcia E., Mon A., Montenegro L., Samper A., Raimbault L., Veilly E. (2022): Integrated reactive transport models for assessing the chemical evolution at the disposal cell scale, D2.17 of the HORIZON 2020 project

Debure, M., Linard, Y., Martin, C. *et al.* (2019). In situ nuclear-glass corrosion under geological repository conditions. npj Materials Degradation 3, 38.

Dhoury, M. (2015), Influence des ions lithium et borate sure l'hydratation de ciments sulfo-alumineux: application au conditionnement de résines échangeuses d'ions boratées, Thèse de doctorat Université de Montpellier

Dillmann, P., Gin, S., Neff, D., Gentaz, L., Rébiscoul, D. (2016). Effect of natural and synthetic iron corrosion products on silicate glass alteration processes. Geochimica et Cosmochimica Acta 172, 287-305.

Duque-Redondo, E., Yamada, K., Manzano, H. (2021). Cs retention and diffusion in C-S-H at different Ca/Si ratio. Cement and Concrete Research 140, 106294.

Dzombak, D.A. and Morel, F.M.M. (1990), Surface complexation Modeling: Hydrous Ferric Oxide. John Wiley & Sons, new York

Elia, A., Ferrand, K., and Lemmens, K. (2017). Determination of the Forward Dissolution Rate for International Simple Glass in Alkaline Solutions , MRS Advances Vol.2, pp.661-667

ENRESA (2001). ENRESA 2000. Evaluación del comportamiento y de la seguridad de un almacén geológico profundo de residuos radiactivos en arcilla. ENRESA (in Spanish).

Ferrand, K., Liu, S. and Lemmens, K. (2018). Integrated leach tests with simulated HLW glass in contact with ordinary Portland cement paste, SCK CEN report ER-0431

Ferrand, K., Klinkenberg, M., Barthel, J., Caes, S., Poonoosamy, J. , Lemmens, K., Bosbach, D. and Brandt, F. (2021), Dissolution Kinetics of International Simple Glass and Formation of Secondary Phases at Very High Surface Area to Solution Ratio in Young Cement Water, Materials 14, 1254

Fleury, B., Godon, N., Ayral, A. *et al.* (2013). SON68 glass dissolution driven by magnesium silicate precipitation, Journal of Nuclear Materials 442(1–3), 17-28.

Fournier, M., Frugier, P., Gin, S. (2018). Application of GRAAL model to the resumption of International Simple Glass alteration. Materials Degradation 2, 21.

Frugier, P., Minet, Y., Rajmohan, N. *et al.* (2018). Modelling glass corrosion with GRAAL. npj Materials Degradation 2, 35.

Gailhanou, H., Lerouge, C., Debure, M., *et al.* (2017). Effects of a thermal perturbation on mineralogy and pore water composition in a clay-rock: An experimental and modelling study, Geochimica et Cosmochimica Acta 197, 193-214.

Gaucher, E.C., Tournassat, C., Pearson, at al. (2009). A robust model for pore-water chemistry of clayrock, Geochimica et Cosmochimica Acta 73(21), 6470-6487.

Giffaut, E., Grivé, M., Blanc, Ph. *et al.* (2014). Andra thermodynamic database for performance assessment: ThermoChimie, Applied Geochemistry 49, 225-236.

Gin, S., Jollivet, P., Fournier, M., Angéli, F., Frugier, P., Charpentier, T. (2015). Origin and consequences of silicate glass passivation by surface layers. Nature Communication 6

Gin, S., Tocino, F., Ferrand, K., Martin, C., Fabian, M. (2019). HLW: Report describing the selected experiments and the existing/expected experimental results. Final version as of 17/12/2019 of deliverable D2.10 of the HORIZON 2020 project EURAD. EC Grant agreement no: 847593.

Gin, S., Delanoe, A., Tocino, F., Ferrand, K., Goethals, J., Sterpenich, J., and Fabian, M. (2022): High level radioactive waste package – Characterization of glass/steel/buffer interaction experiments. Final version as of 04.05.2023 of deliverable D2.12 of the HORIZON 2020 project EURAD. EC Grant agreement no: 847593.

Glasser, F.P., Matschei, T. (2007). Interactions between Portland cement and carbon dioxide. Proceedings of the ICCC Conference.

Grangeon, S., Debure, M., Montouillout, V., Elkaïm, E., Lerouge, C., Gaboreau, S., Maubec, N., Bourbon, X., Martin, C., Michau, N., and Marty, N. (to be published), Evolution of a cementitious grout upon alteration in aqueous solution: insights from laboratory and in-situ mineralogical characterizations and geochemical modelling.

Hellmann, R., Cotte, S., Cadel, E., Malladi, S., Karlsson, L.S., Lozano-Perez, R., Cabié, M., Seyeux, A. (2015). Nanometre-scale evidence for interfacial dissolution-precipitation control of silicate glass dissolution, Nature Materials 14, 307-311

Hong, S.Y., Glasser, F.P. (1999). Alkali binding in cement pastes : Part I. The C-S-H phase. Cement and Concrete Research 29, 1893-1903.

Jander, W. (1927), Reaktionen im festen Zustande bei höheren Temperaturen. Reaktionsgeschwindigkeiten endotherm verlaufender Umsetzungen, Zeitung für anorganische and allgemeine Chemie, 163 (1): 1-30, http://dx.doi.org/10.1002/zaac.19271630102

Jennings, H.M. (2004). Colloid model of C−S−H and implications to the problem of creep and shrinkage. Materials and Structures 37, 59-70.

Jennings, H.M., Bullard, J.W., Thomas, J.J., Andrade, J.E., Chen, J.J., Scherer, G.W. (2008). Characterization and modeling of pores and surfaces in cement paste: correlations to processing and properties. Journal of Advanced Concrete Technology 6, 5-29.

Johnson, J., Anderson, F., and Parkhurst, DL. (2000). Database thermo.com.V8.R6.230, Rev 1.11. Lawrence Livermore National Laboratory, Livermore, California.

Kaufhold, S., Dohrmann, R., Weber, C. (2021). Evolution of the pH value at the vicinity of the iron-bentonite interface, Applied Clay Science 201, 105929.

Krattiger, N., Lothenbach, B., Churakov, S.V., (2021). Sorption and electrokinetic properties of ASR product and C-S-H: A comparative modelling study. Cement and Concrete Research 146, 106491.

Labbez, C., Pochard, I., Jönsson, B., Nonat, A. (2011). C-S-H/solution interface: Experimental and Monte Carlo studies. Cement and Concrete Research 41, 161-168.

Lemmens, K., and Ferrand, K. (2019). Dissolution behaviour of vitrified high-level waste in highly alkaline conditions, SCK CEN report ER-0559

Liu, S., Jacques, D., Govaerts, J., Wang, L. (2014). Conceptual model analysis of interaction at a concrete–Boom Clay interface. Physics and Chemistry of the Earth, Parts A/B/C 70-71, 150-159.

Liu, S. Ferrand, K., Lemmens, K. (2015). Transport- and surface reaction-controlled SON68 glass dissolution at 30 °C and 70 °C and pH = 3.7, Applied Geochemistry 61, 302-311

Liu, S. Ferrand, K., Aertsens, M., Jacques, D., and Lemmens, K. (2019). Diffusion models for the early-stage SON68 glass dissolution in a hyper-alkaline solution, Applied Geochemistry 111, 104439

Lothenbach, B., and Winnefeld, F. (2006). Thermodynamic modelling of the hydration of Portland cement, Cement and Concrete Research 36, 209-226

Mann, C., Ferrand, K., Liu, Sanheng., Eskelsen, J.R., Pierce, E., Lemmens, K., and Corkhill, C. (2019). Influence of young cement water on the corrosion of the International Simple Glass, NPJ Materials degradation 3:5

Marty, N.C.M., Fritz, B., Clement, A., *et al.* (2010). Modelling the long term alteration of the engineered bentonite barrier in an underground radioactive waste repository. Applied Clay Science, Volume 47 (1–2), 82-90.

Marty, N.C.M., Bildstein, O., Blanc, P., Claret, F., Cochepin, B., Gaucher, E.C., Jacques, D., Lartigue, J.-E., Liu, S., Mayer, K.U., Meeussen, J.C.L., Munier, I., Pointeau, I., Su, D., Steefel, C.I. (2015). Benchmarks for multicomponent reactive transport across a cement/clay interface. Computational Geosciences 19, 635-653.

Marty N.C.M., Claret F., Lassin A. *et al.* (2015b). A database of dissolution and precipitation rates for clay-rocks minerals. Applied Geochemistry 55, 108-118.

Marty N.C.M., Lach A., Lerouge C., *et al.* (2018). Weathering of an argillaceous rock in the presence of atmospheric conditions: A flow-through experiment and modelling study. Applied Geochemistry 96, 252-263.

Miron, D.M., Kulik, D.A., Yan, Y., Tits, J., and Lothenbach, B. (2022). Extensions of CASH-thermodynamic solid solution model for the uptake of alkali metals and alkaline earth metals in C-S-H. Cement and Concrete Research 152, https://doi.org/10.1016/j.cemconres.2021.106667

Mosser-Ruck, R., Sterpenich, J., Michau, N., *et al.* (2020). Serpentinization and H_2 production during an iron-clay interaction experiment at 90°C under low CO_2 pressure. Applied Clay Science 191, 105609.

Mosser-Ruck, R., Cathelineau, M., Guillaume, D., *et al.* (2010). Effects of temperature, pH, and iron/clay and liquid/clay ratios on experimental conversion of dioctahedral smectite to berthierine, chlorite, vermiculite, or saponite. Clays and Clay Minerals 58(2), 280-291.

Necib, S., Linard, Y., Crusset, D., *et al.* (2016). Corrosion at the carbon steel-clay borehole water and gas interfaces at 85°C under anoxic and transient acidic conditions. Corrosion Science 111, 242-258.

Neeft, E., Weetjens E., Vokal A., Leivo M., Cochepin B., Martin C., Munier I., Deissmann G., Montoya V., Poskas P., Grigaliuniene D., Narkuniene A., García E., Samper J., Montenegro L., Mon A. (2019): Treatment of chemical evolution in National Programmes, D 2.4 of the HORIZON 2020 project EURAD. EC Grant agreement no: 847593.

Neeft E., Jacques D., Deissmann G. (2022): Initial State of the Art on the assessment of the chemical evolution of ILW and HLW disposal cells. D 2.1 of the HORIZON 2020 project EURAD. EC Grant agreement no: 847593.

Parkhurst, D.L., Appelo, C.A.J. (2013). Description of input and examples for PHREEQC version 3 - A computer program for speciation, batch-reaction, one-dimensional transport, and inverse geochemical calculations. U.S. Geological Survey Techniques and Methods, book 6, chap. A43, 497 p., available only at http://pubs.usgs.gov/tm/06/a43

Parrot, L.J. and Killoh, D.C. (1984). Prediction of cement hydration. Br Ceram trans 35 : 41-53

Rivard, C., Pelletier, M., Michau, N., *et al.* (2013). Berthierine-like mineral formation and stability during the interaction of kaolinite with metallic iron at 90 °C under anoxic and oxic conditions. American Mineralogist 98. 163-180.

Samper, J., Montenegro, L., De Windt, L., Montoya, V., Garibay-Rodríguez, J., Grigaliuniene, D., Narkuniene, A., Poska,s P., Cochepin, B. (2022): Conceptual model formulation for a mechanistic based model implementing the initial SOTA knowledge (models and parameters) in existing numerical tools. Final version as of 15.07.2022 of deliverable D2.16 of the HORIZON 2020 project EURAD. EC Grant agreement no: 847593.

Schlegel, M.L., Bataillon, B., Blanc *et al.* 2010. Anodic Activation of Iron Corrosion in Clay Media under Water-Saturated Conditions at 90 °C: Characterization of the Corrosion Interface. Environ. Sci. Technol 44(4), 1503–1508

Taylor, H.F.W. (1997). Cement Chemistry. Thomas Telford.

Thiéry, D. (2015). Modélisation 3D du Transport Réactif avec le code de calcul MARTHE v7.5 couplé aux modules géochimiques de PHREEQC, in: BRGM/RP-65010-FR, R. (Ed.), Orléans, France, pp. 164, available at http://infoterre.brgm.fr/rapports/RP-65010-FR.pdf

Thompson, J.L., Silsbee, M.R., Gill, P.M., Scheetz, B.E. (1997). Characterization of silicate sealers on concrete. Cem. Concr. Res. 27, 1561-1567.

Truche, L., Berger, G., Destrigneville, C., *et al.* (2009). Experimental reduction of aqueous sulphate by hydrogen under hydrothermal conditions: Implication for the nuclear waste storage, Geochimica et Cosmochimica Acta 73(16), 4824-4835.

Utton, C.A., Hand, R.J., Bingham, P.A., Hyatt, N.C., Swanton, S.W., and Williams, S.J. (2013), Dissolution of vitrified wastes in a high-pH calcium-rich solution, Journal of Nuclear Materials 435, 112-122

Večerník, P. , Drtinová, B. et al. (2019) Transport properties of cement-based materials, ÚJV Řež Technical report 430/2019/ENG

Vienna, J.D., Ryan, J.V. (2013). Current understanding and remaining challenges in modelling long-term degradation of borosilicate nuclear waste glasses. International Journal of Applied Glass Science 4, 283-294.

Non-exhaustive overview of processes modelled in task 3

Glass/steel/cement/clay	**Exp. 3 SCK CEN**	**Waste package SCK CEN**	**Exp. 2 BRGM**	**Waste package BRGM**
Evolution prior to contact glass/water				
Consumption of O2 in phase I	no	no	no	no
Generation of H2 gas by anaerobic corrosion	no	no	No (only H_2(aq))	No (only H_2(aq))
Concrete evolution by interaction with host rock	no	no	yes	yes
Concrete evolution by interaction with steel	no	no	yes	yes
Evolution of temperature = f(time, distance)	no	no	no	no
Corrosion kinetics of steel overpack in contact with concrete	no	no	yes	yes
Effects of beta,gamma radiation on near field and steel corrosion	no	no	no	no
Evolution after contact glass/water				
Glass alteration in humid atmosphere	no	no	no	no
Glass dissolution driven by affinity of model phase (SiO2, end members…)	no	no	Yes (GRAAL)	Yes (GRAAL)
Diffusion of glass constituents through growing GAL	yes	yes	Yes (GRAAL)	Yes (GRAAL)
Precipitation of secondary phases	no	no	yes	yes
Corrosion kinetics of steel in contact with glass	no	no	no	yes
Interaction of glass constituents with corroding steel	no	no	yes	yes
Interaction of glass constituents with steel corrosion products	no	no	yes	yes
Dissolution from internal surfaces (initial cracks)	no	no	no	no
Evolution of surface area by further cracking under mechanical stress (a.o. growing corrosion product layers)	no	no	no	no

Evolution of surface area by gradual glass dissolution	no	no	layer-by-layer	layer-by-layer
Effect of alpha radiolysis on glass dissolution	no	no	no	no
Ion exchange between glass surface and solution	no	no	no	no
Residual glass dissolution rate	yes	yes	Yes (GRAAL)	Yes (GRAAL)
Reactive transport of dissolved glass components (Si) in cement buffer (diffusive transport)	yes	yes	yes	yes
Reactive transport of dissolved glass components (Si) in cement buffer (advective transport)	no	no	no	no
Far field processes				
Reactive transport of glass constituents in host rock	no	no	yes	yes
Other model characteristics				
1 dimensional	yes	yes	yes	yes
2 dimensional	no	no	yes	yes
3 dimensional	no	no	no	no
Retardation/precipitation of RN in clay or cement buffer	no	no	no	no

Table with chemical formulae of minerals

Mineral name	**Formula**
Berthierine (FeII)	$(Fe_2Al)(SiAl)O_5(OH)_4$
Calcite	$CaCO_3$
Celestite	$SrSO_4$
Chukanovite	$Fe^{+2}{}_2(CO_3)(OH)_2$
Cronstedtite-Th	$Fe_3SiAlO_5(OH)_4$
CSH1.2	$Ca_{1.2}SiO_{3.2}{:}2.06H_2O$
CSH1.6	$Ca_{1.6}SiO_{3.6}{:}2.58H_2O$
C3FH6	$Ca_3Fe_2(OH)_{12}$
Ettringite	$Ca_6Al_2(SO_4)_3(OH)_{12}{:}26H_2O$
Gibbsite	$Al(OH)_3$
Goethite	FeOOH
Greenalite	$((Fe^{2+},Fe^{3+})_{2\text{-}3}Si_2O_5(OH)_4)$
Hydrotalcite	$Mg_4Al_2O_7{:}10H_2O$
Hydroxyapatite	$Ca_5(PO_4)_3(OH)$
K-phillipsite	$KAlSi_3O_8{:}3H_2O$
Magnetite	Fe_3O_4
Mackinawite	$(Fe,Ni)_{1+x}S$
Monocarboaluminate	$Ca_4Al_2CO_9{:}10.{}_{68}H_2O$
Natrolite	$Na_2(Al_2Si_3)O_{10}{:}2H_2O$
Nontronite-Na	$Na_{0.34}Fe_{1.67}Al_{0.67}Si_{3.66}O_{10}(OH)_2$
Pimelite	$Ni_3Si_4O_{10}(OH)_2{\bullet}4(H_2O)$
Portlandite	$Ca(OH)_2$
pyrite	FeS_2
Pyrrhotite	FeS
Saponite-FeCa	$Ca_{0.17}Mg_2FeAl_{0.34}Si_{3.66}O_{10}(OH)_2$
Siderite	$FeCO_3$
Stratlingite	$Ca_2Al_2SiO_7 \cdot 8H_2O$
Tobermorite	$Ca_5Si_6O_{16.5}(OH){:}10H_2O$
Zincsilite	$Zn_3Si_4O_{10}(OH)_2 \cdot 4H_2O$